Longitudinal intensity effects in the CERN Large Hadron Collider

THÈSE N^{O} 7077 (2016)

PRÉSENTÉE LE 28 JUIN 2016
À LA FACULTÉ DES SCIENCES DE BASE
LABORATOIRE DE PHYSIQUE DES ACCÉLÉRATEURS DE PARTICULES

ÉCOLE POLYTECHNIQUE FÉDÉRALE DE LAUSANNE

POUR L'OBTENTION DU GRADE DE DOCTEUR ÈS SCIENCES

PAR

Juan Federico ESTEBAN MÜLLER

acceptée sur proposition du jury:

Prof. R. Houdré, président du jury
Prof. L. Rivkin, Dr E. Shaposhnikova, directeurs de thèse
Prof. M. Migliorati, rapporteur
Dr G. Rumolo, rapporteur
Dr L. Stingelin, rapporteur

ÉCOLE POLYTECHNIQUE
FÉDÉRALE DE LAUSANNE

Suisse
2016

A María

Acknowledgements

First and foremost I want to thank my supervisor, Elena Shaposhnikova, for introducing me to the fascinating field of accelerator physics as a Fellow at CERN and for giving me the opportunity to do my PhD under her guidance. This work would not have been possible without her continuous support and advice. Her office door was always open and she was available for discussion and explanations at all times. I am very thankful to her for helping in preparing for measurements, talks, papers, and for proofreading this manuscript with patience. I am more than indebted to her.

I am also very grateful to Lenny Rivkin, for being my thesis advisor at the EPFL, for encouraging me to pursue this PhD research, and for his valuable advice and help. I want to thank him as well for supporting my participation in the CERN Accelerator School and the International Particle Accelerator Conference (IPAC'14), where I could improve my knowledge on accelerator physics and present my work.

Special thanks to Thomas Bohl, for sharing with me his immense knowledge about beam dynamics, accelerators operation, rf measurements and electronics, and much more. I enjoyed every time I spent with him in the Faraday cage. I really appreciate his constant availability for discussion and willingness to help. I am also very grateful to him for helping me writing the abstract of this thesis in German.

I am thankful to Philippe Baudrenghien, for everything he taught me about rf measurements and beam dynamics, and especially for all the detailed explanations about the LHC rf system. It was a pleasure to work together with him during MDs and operation of the LHC, either sitting in the CCC or in SR4, or in the LHC tunnel.

I have been amazingly fortunate to have had two wonderful office mates: Theodoros Argyropoulos and Alexandre Lasheen. At the very beginning, when Theo was my only office mate, he was very helpful and friendly. The experience was further enriched with the arrival of Alex. I truly enjoyed their company and from both of them I have learned a lot. At this point, I would also like to extend my gratitude to Helga Timko, who was not in the same office but with whom I worked closely. Her advice has always been very valuable.

It was also a pleasure to be part of the RF-BR section, with so many colleagues always willing to help. Thanks to all current and past colleagues of the section.

I appreciate the help of all the colleagues of the RF-FB and RF-CS sections, but more especially Daniel Valuch, Themis Mastoridis, John Molendijk, Urs Wehrle, and of course Philippe. Understanding the LHC low-level rf system and preparing for measurements is much less complicated with the explanations of so helpful people.

I would like to show my gratitude to the LHC RF MD team and everyone who contributed to the accomplishment of the MDs. Working nights and weekends was more pleasant with all of you. Special thanks in this case to Elena, Thomas, Philippe, Helga, Theodoros, Alex, and Themis. Thanks also to Tom Levens for his help with the beam instrumentation.

I want to acknowledge the BLonD developers, Alex, Danilo, Helga, and Theodoros, for making such a great and reliable work, which has been intensively used in this thesis.

Thanks also to the impedance team, in particular to Nicolas Mounet, Benoît Salvant, and Nicolò Biancacci, for their support with impedance calculations and measurements. Their help was essential for this thesis.

The contribution of the e-cloud team were also extremely important for this work. I really appreciate the help of Giovanni Rumolo, Gianni Iadarola, and Hannes Bartosik.

I am grateful to all the participants to the meetings on LHC machine studies and beam operation (LSWG and LBOC), for their help in organizing and carrying out measurements in the LHC. Of course, none of these measurements could have been done without the kind assistance of the LHC and all injectors' operators. Thanks to all of them.

I would like to thank Rama Calaga for leading the HiLumi Work Package 4 and Elias Métral for leading the HiLumi Task 2.4, as well as to all other members, for the very useful discussions about collective effects in the HL-LHC.

Although related to a machine not studied in this thesis, the SPS, I have also found very useful the participation in the LIU-SPS BD working group. I would like to thank Elena for chairing the meetings and all the participants for their great contributions, which have been very valuable for me.

Besides all the people who have directly contributed and helped me to carry out this PhD work, I want to thank all my friends that I met during my stay at CERN. In particular, I am very grateful to my closest Spanish friends: Álvaro, Manu, Roberto, Alberto, José, Alicia, and Jesús.

I would like to thank my family, especially to my sister and my parents, for being so supportive throughout my life.

Finally, I want to express my eternal gratitude to my wife, María, for her inestimable support during all these years.

Lausanne, April 2016 J. F. E. M.

Abstract

This PhD thesis provides an improved knowledge of the LHC longitudinal impedance model and a better understanding of the longitudinal intensity effects. These effects can limit the LHC performance and lead to a reduction of the integrated luminosity.

The LHC longitudinal impedance was measured with beams. Results obtained using traditional techniques are consistent with the expectations based on the impedance model, although the measurement precision was proven insufficient for the low impedance of the LHC. Innovative methods to probe the LHC reactive impedance were successfully used. One of the methods is based on exciting the beam with a sinusoidal rf phase modulation to estimate the synchrotron frequency shift from potential-well distortion. In the second method, the impedance is estimated from the loss of Landau damping threshold, which is also found to be in good agreement with analytical estimations.

Beam-based impedance measurements agree well with estimations using the LHC impedance model. Macroparticle simulations of loss of Landau damping reproduce the measurements precisely and are used to determine the current stability limits.

The single-bunch stability is analyzed for the HL-LHC, for a bunch intensity almost twice higher than the nominal LHC intensity. The effect of an additional rf system installed for double rf operation provides an increased stability margin in the absence of a wideband longitudinal damper system. The differences between the bunch-shortening and bunch-lengthening operation modes are presented, as well as the effect of an error in the phase synchronization between both rf systems. Several options for the rf parameters are considered, and their advantages and drawbacks under different circumstances are analyzed.

A novel diagnostic tool for e-cloud monitoring based on bunch phase measurements has been fully developed. An advanced post-processing was implemented to improve the measurement accuracy up to the required level by reducing systematic and random errors. The tool is available at the CERN Control Room and shows the e-cloud build-up structure along the bunch trains and the total beam power loss due to e-cloud. Phase shift measurements are in good agreement with simulations of the e-cloud buildup and can be used to estimate the heat load in the cryogenic system. The use of this method in operation has been proven to ease the scrubbing run optimization and can eventually be used as an additional input for the cryogenic system.

Keywords: Accelerator, beam dynamics, beam-based measurements, collective effects, electron cloud, high-intensity beams, HL-LHC, impedance, LHC, longitudinal, macroparticle simulations, radiofrequency (rf), single-bunch stability, wakefield.

Zusammenfassung

Diese Dissertation verbessert den Wissensstand über das longitudinale LHC Impedanzmodell und dient einem besseren Verständnis der longitudinalen Intensitätseffekte im LHC. Diese Effekte können die LHC Leistungsfähigkeit begrenzen und zu einer Reduzierung der integrierten Luminosität führen.

Die longitudinale LHC Impedanz wurde mit Strahl gemessen. Ergebnisse unter Verwendung von herkömmlichen Techniken wurden erhalten. Sie sind in Übereinstimmung mit den auf dem Impedanzmodell basierten Erwartungen, obwohl die Genauigkeit der Messungen nicht ausreichend war, um die sehr niedrige Impedanz des LHC zu messen. Die reaktive LHC Impedanz wurde erfolgreich mit innovativen Methoden ermittelt. Eine der Methoden basiert auf der Anregung des Strahls mit einer sinusförmigen Modulation der Phase des Hochfrequenzsystems (HF-Systems), um die Synchrotron-Frequenzverschiebung aufgrund der Verzerrung des Potentialtopfes abzuschätzen. Eine weitere Methode besteht darin, die Impedanz aus dem Zeitpunkt des Eintretens des Verlustes der Landau-Dämpfung zu ermitteln. Sie steht in guter Übereinstimmung mit analytischen Berechnungen.

Strahlbasierte Impedanzmessungen stimmen gut mit den Schätzungen des LHC Impedanzmodells überein. Numerische Simulationen des Verlusts von Landau-Dämpfung reproduzieren die Messungen und werden verwendet, um die aktuellen Stabilitätsgrenzen zu bestimmen.

Die Stabilität eines einzelnen Teilchenpaketes, mit einer fast zweimal höheren Intensität als ein nominales LHC Teilchenpaket, wurde für den Fall des HL-LHC analysiert. In Abwesenheit eines breitbandigen longitudinalen Dämpfungssystems, kann der Stabilitätsbereich durch ein zusätzliches HF System mit der halben oder auch der doppelten Frequenz erweitert werden. Die Unterschiede zwischen den beiden Betriebsarten Paketverkürzung und Paketverlängerung werden beschrieben, sowie der Einfluss eines Fehlers in der Phasensynchronisation zwischen den beiden HF-Systemen. Mehrere Optionen für die HF-Parameter werden betrachtet und ihre Vor- und Nachteile unter verschiedenen Umständen analysiert.

Ein neues Diagnose-Instrument wurde für die Überwachung der Elektronenwolke entwickelt. Es basiert auf Messungen der Phase des Teilchenpakets in Bezug auf die HF Spannung. Eine erweiterte Nachbearbeitung der Messdaten wurde implementiert um die systematischen und zufälligen Fehler bis auf den erforderliche Grad der Messgenauigkeit zu reduzieren. Das Instrument steht im CERN Control Center den Operateuren und Maschinenexperten zur Verfügung. Es zeigt den Aufbau der Elektronenwolke entlang der Teilchenpakete und die Gesamtverlustleistung des Strahls durch die Elektronenwolke. Die Phasenverschiebungsmessungen sind in guter Übereinstimmung mit Simulationen des Aufbaus der Elektronenwolke und können zur

Bestimmung der Wärmebelastung im Kryogeniksystem verwendet werden. Die Verwendung dieser Methode im Betrieb des LHC hat sich bei der Optimierung des “Scrubbing Runs” als nützlich erwiesen. Diese Methode könnte auch zur besseren Steuerung das Kryogeniksystems eingesetzt werden.

Stichwörter: Elektronenwolke, HL-LHC, Hochfrequenz (HF), hohe Intensität, Impedanz, Kielfeld, kollektive Effekte, LHC, longitudinal, Numerische Simulationen, Stabilität, Strahlbasierte Messungen, Strahldynamik, Teilchenbeschleuniger.

Résumé

Ce travail de thèse fournit une meilleure connaissance du modèle d'impédance longitudinale du LHC et une meilleure compréhension des effets d'intensité longitudinaux. Ces effets peuvent limiter les performances du LHC et conduire à une réduction de la luminosité intégrée.

L'impédance longitudinale du LHC a été mesurée avec des faisceaux. Les résultats obtenus grâce à l'utilisation des techniques traditionnelles sont conformes aux attentes fondées sur le modèle d'impédance, même s'il est prouvé que la précision des mesures est insuffisante pour mesurer la faible impédance du LHC. Des méthodes innovantes pour sonder l'impédance réactive du LHC ont été utilisées avec succès. La première méthode est basée sur l'excitation du faisceau avec une modulation de phase RF sinusoïdale pour estimer le décalage de fréquence synchrotronique provenant de la distorsion du puit de potentiel. Dans la deuxième méthode, l'impédance est estimée à partir du seuil de la perte de l'amortissement Landau, donnant un très bon accord avec les estimations analytiques.

Les mesures d'impédance avec le faisceau concordent bien avec les estimations faites à l'aide du modèle d'impédance du LHC. Les simulations de la perte de l'amortissement Landau reproduisent les mesures avec précision et sont utilisées pour déterminer les limites de stabilité actuelles.

La stabilité d'un paquet unique est analysée dans le cas du HL-LHC, pour une intensité presque deux fois plus élevée que l'intensité nominale du LHC. L'effet d'un système RF supplémentaire, installé pour un fonctionnement en double RF, fournit une marge de stabilité accrue en l'absence d'un système d'amortissement des oscillations longitudinales à large bande. Les différences entre les modes de fonctionnement de raccourcissement de paquets et d'allongement de paquets sont présentés, ainsi que les conséquences d'une erreur dans la synchronisation de phase entre les deux systèmes RF. Plusieurs options pour les paramètres RF sont considérées, et leurs avantages et inconvénients dans des circonstances diverses sont analysés.

Un nouvel outil de diagnostic pour la surveillance des nuages d'électrons basé sur des mesures de phase des paquets a été entièrement développé. Un post-traitement avancé a été mis en œuvre pour améliorer la précision de la mesure au niveau requis en réduisant les erreurs systématiques et aléatoires. Cet outil est disponible à la salle de contrôle du CERN et montre la structure de l'accumulation du nuage d'électrons le long des trains de paquets et la perte de puissance totale du faisceau dû au nuage d'électrons. Les mesures de décalage de phase sont en conformité avec les simulations de l'accumulation du nuage d'électrons et peuvent être utilisées pour estimer la charge de chaleur dans le système cryogénique. L'utilisation de cette méthode dans le fonctionnement a été prouvée pour faciliter l'optimisation des "Scrubbing Runs" et peut éventuellement être utilisée comme une entrée supplémentaire pour le système cryogénique.

Mots clefs : Accélérateur, champs de sillage, dynamique du faisceau, effets collectifs, faisceaux a haute intensité, impédance, mesures avec le faisceau, HL-LHC, LHC, nuage d'électrons, plan longitudinal, radiofréquence (RF), stabilité d'un paquet unique, simulations de particules.

Contents

Introduction

Particle accelerators are very powerful instruments that are used nowadays in many different fields. Being initially developed for nuclear and particle physics, currently they have additional applications that include, for instance, particle therapy for cancer treatment, radioisotopes production, and the use of synchrotron light sources in biology, chemistry, materials science, etc. Each of those applications can have different requirements in terms of beam intensity, size, and energy, as well as the particle type; and that has important implications for the design of the accelerator.

The most important parameter for high-energy physics accelerators is the energy available in the center of mass, which has to be sufficiently high to produce the particles of interest. In general, colliders are preferred as the beam energy required for a given energy available in the center of mass is lower than the one required in a fixed-target experiment, even though colliders have additional complications related to the acceleration of two beams.

Another important parameter that needs to be maximized is the number of collisions, as it defines the number of events that can be observed for a process with a given cross section. The number of events is proportional to the luminosity $\mathscr{L}$, defined for Gaussian bunches as

$$\mathscr{L} = \frac{N_b^2 M_b f_{\text{rev}}}{4\pi \sigma_x \sigma_y} S, \tag{1}$$

where N_b is the number of particles per bunch, M_b is the number of colliding bunches, f_{rev} is the revolution frequency of the particles, σ_x and σ_y are the transverse beam sizes, and S is the geometric luminosity-reduction factor, which takes into account the crossing angle and the bunch length.

In colliders, the goal is to maximize the luminosity and that requires a large number of bunches with high intensities and small size, i.e., high brightness. These requirements present a challenge, as high-brightness beams suffer from limitations caused by their electromagnetic interaction with the surroundings. Known as intensity effects, these interactions can degrade the performance of the accelerators, determining the minimum beam size and the maximum number of bunches achievable for a given intensity.

The CERN Large Hadron Collider (LHC)

The European Organization for Nuclear Research (CERN) is an international laboratory that operates a series of accelerators for nuclear and particle physics research, including the Large Hadron Collider (LHC), as well as a range of lower energy particle accelerators.

The LHC is a 27 km long particle accelerator designed to increase the energy of high-brightness proton beams from 450 GeV up to 7 TeV, and also of heavy ions from 177 GeV/u to 2.76 TeV/u. This thesis focuses on the LHC operation with proton beams and the limitations arising due to intensity effects. The LHC was designed to collide beams in the physics experiments installed in 4 different interaction points of the ring with an energy available in the center of mass of up to 14 TeV [1].

In the beginning of the LHC run 1 (2010–2013), the proton beam energy at collisions was 3.5 TeV, a half of the designed value. Starting from 2012, the top energy was increased to 4 TeV until the Long Shutdown 1 (2013–2015). A highlight of the experiment's results using data acquired during the LHC run 1 is the discovery of a new boson compatible with the Higgs boson [2, 3]. On the restart in 2015, the top energy was set to 6.5 TeV.

During the acceleration, the current in the magnets has to be gradually increased. As the LHC uses superconducting magnets to achieve a magnetic field of up to 8.3 T, the current cannot be increased too fast. For that reason, the length of the acceleration ramp is about ten minutes for the energies reached in the run 1 and approximately twenty minutes to arrive at 6.5 TeV, to be compared with acceleration ramps lasting seconds or even milliseconds in smaller, normal-conducting machines.

Injection into the LHC requires that the beams are accelerated in early stages to 450 GeV. For this purpose, the beams are accelerated in steps in different machines, using the accelerator complex shown in Fig. 1. The protons are extracted from the source to the Linear Accelerator 2 (LINAC 2), a 50 MeV linear accelerator. Then the Proton Synchrotron Booster (PS Booster) increases the kinetic energy of the beams up to 1.4 GeV, which is the injection energy of the Proton Synchrotron (PS). The PS also performs some rf manipulations in order to generate the time structure of the beam required by the LHC. The beams are then extracted from the PS with an energy of 25 GeV and are accelerated to 450 GeV in the Super Proton Synchrotron (SPS). The heavy ions are produced from a different source and the beam is first accelerated in the Linear Accelerator 3 (LINAC 3) to an energy of 4.2 MeV/u. Then the ions are transferred to the Low-Energy Ion Ring (LEIR), which increases the ion energies to 72 MeV/u before transferring them to the PS, from where they follow the same path as the protons.

The purpose of the injectors is not only to accelerate the LHC beam, but also to provide beams with different energies for different experiments. For example, beams extracted from the PS Booster are sent to ISOLDE to produce radioactive ion beams. PS beams are used to produce neutrons for the n-ToF experiment, antiprotons for the Antiproton Decelerator (AD), and are extracted for other fixed-target experiments. SPS beams are also sent to fixed-target

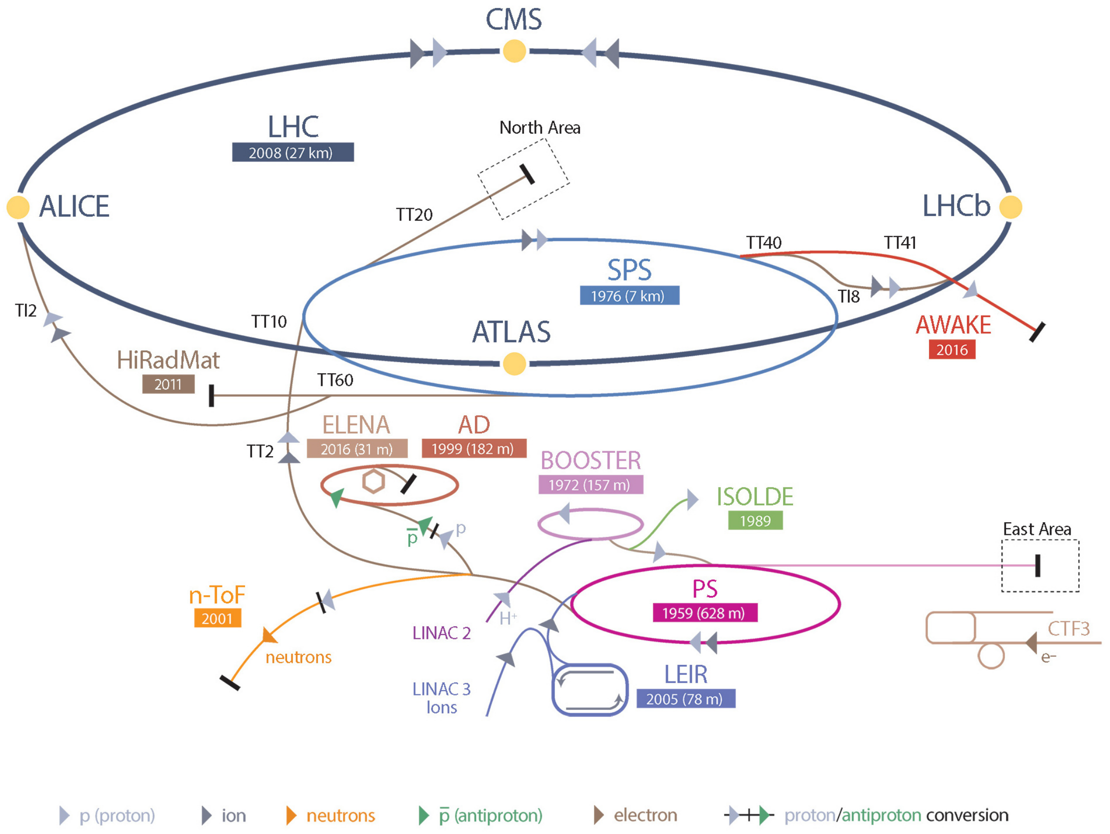

Figure 1 – The CERN accelerator complex. The year of construction and length of the circular accelerators is shown under their names, and the type of accelerated particles is marked in the transfer lines.

experiments, to an experimental area devoted to testing the effect of high-energy beams on materials and devices (HiRadMat), and will be used in the near future to test plasma wakefield acceleration in the AWAKE experiment.

In view of increasing the research capabilities of CERN, several upgrade options are currently being studied and planned. The High-Luminosity LHC (HL-LHC) [4] is one of the upgrade projects, aiming at increasing the luminosity produced in the LHC by approximately a factor 10 compared to the nominal LHC design value. That is achieved by increasing the bunch intensity by about a factor 2 and reducing the transverse beam size at the collision points. Intensity effects will become even more important for these beam and machine parameters, and different design options are being considered to mitigate them.

In order to reach the beam parameters necessary for the HL-LHC, another project is dealing with an upgrade of the LHC injectors: the LHC Injectors Upgrade (LIU) [5]. The magnitude of this project is also quite large, as the limitations of each injector need to be addressed and mitigation measures or upgrades have to be found and implemented.

Thesis outline

This PhD thesis presents a study of the longitudinal intensity effects in the LHC for proton beams. Based on a realistic impedance model, carefully verified by beam measurements using advanced diagnostic tools, predictions of the current performance limits in terms of beam stability are found. Implications of the HL-LHC project related to the longitudinal intensity effects will be also considered. The structure of the thesis is described below.

The beam dynamics of the synchrotron motion is reviewed in Chapter 1. First, the equations of motion for a single particle are derived and some important rf and beam parameters are defined. Then, the interaction of the charged-particle beam with the surroundings is analyzed using the concepts of wakefield and impedance. The outcomes of this interaction when the number of particles is increased are also examined there, as well as a natural mechanism that prevents instabilities from developing called Landau damping. Another effect that appears for high-intensity beams of positively charged particles, the electron cloud (e-cloud), is overviewed. Finally, some basic concepts of macroparticle tracking simulation codes are discussed and the code used for the results presented in this thesis is described.

In Chapter 2, an overview of the main parameters of the LHC and its rf system is presented, including a description of the low-level rf loops and the available beam diagnostics.

Measurements of the LHC impedance with beams are presented in Chapter 3 and compared with the LHC impedance model. Then, the LHC impedance model is used in macroparticle tracking simulations to find the LHC single-bunch longitudinal stability threshold, which is also compared to the threshold observed in the machine. The multi-bunch stability is briefly discussed.

The same method as used in Chapter 3 to determine the single-bunch longitudinal stability threshold in the LHC is used in Chapter 4 to establish the stability limits for the HL-LHC upgrade and to define a valid parameter set for the beam. Considerations related to the HL-LHC operation with an additional rf system are evaluated, and results from simulations of beam stability in a double rf system are presented.

Chapter 5 describes a novel method to monitor the e-cloud based on rf measurements. The method makes use of precise measurements of the energy lost by the beam due to the interaction with the e-cloud, which is connected to the e-cloud density in the ring. The main advantages with respect to other indirect measurements of the e-cloud are also discussed, as well as the use of the method in LHC operation.

Finally, Chapter 6 summarizes the main conclusions of this PhD thesis.

1 Synchrotron motion and intensity effects

In this chapter, the synchrotron motion of the particles in an accelerator is reviewed, as well as the interaction of a charged particle beam with its surroundings. Special attention is given to the effects caused by the beam-coupling impedance, like the potential-well distortion and beam instabilities. The electron-cloud effect is also described. Some important equations used in the following chapters of the thesis are introduced here. Finally, basic concepts of macroparticle simulation codes are also covered.

1.1 Longitudinal single-particle motion

In a synchrotron, a charged particle beam is confined and accelerated by electromagnetic fields. The force **F** exerted on a particle with charge q traveling at a velocity **v** in the presence of an electric **E** and a magnetic field **B** is described by the Lorentz force:

$$\mathbf{F} = q\left(\mathbf{E} + \mathbf{v} \wedge \mathbf{B}\right). \tag{1.1}$$

As the term corresponding to the magnetic field in Eq. (1.1) is perpendicular to the particle velocity **v**, the acceleration of the particles has necessarily to be done through an electric field. Although an electrostatic field can be used for acceleration, it is practical only for low-energy accelerators as they are limited by the field breakdown and the length of the accelerator. High-energy accelerators rely on radio-frequency (rf) cavities to provide the accelerating voltage. There are several types of rf cavities, which can be classified according to the electromagnetic wave characteristics in standing-wave cavities or traveling-wave structures. Depending on the cavity material, we can also distinguish between normal-conducting cavities and superconducting cavities. The choice of the cavity type depends on many factors, as the required voltage, frequency, and power; fabrication and operation costs; space constraints, etc. (for more details see e.g., [6]).

The particle trajectory can be modified either by an electric or a magnetic field, but for particles with high velocities, it is usually more convenient to make use of magnets, as the corresponding force linearly increases with the particle speed. Dipole magnets are generally used to bend the particles and to keep them in a closed trajectory, and quadrupole magnets are used to focus the beam in the plane that is perpendicular to the longitudinal displacement (transverse plane).

The magnetic field in the dipole magnets should be such that the particles experience a Lorentz force (1.1) which is equal in magnitude and opposite in direction to the centrifugal force F_c:

$$F_c = m\frac{v^2}{\rho} = q\,v\,B, \tag{1.2}$$

where m is the particle mass and ρ is the bending radius. From Eq. (1.2), the following expression can be obtained:

$$\frac{p}{q} = B\,\rho, \tag{1.3}$$

where p is the particle momentum. Equation (1.3) is known as the magnetic rigidity and it indicates that if the particle momentum changes (acceleration or deceleration), the magnetic field of the dipole magnets should be adjusted accordingly to keep the orbit radius constant.

The position of a particle can be described in a Cartesian coordinate system that moves with a reference particle, as shown in Fig. 1.1. This particle has the design energy E_o and passes through the center of all the magnets describing a closed trajectory of length $C_o = v\,T_o$, with an angular revolution frequency $\omega_o = 2\pi/T_o$. Using this coordinate system, the motion in the longitudinal direction z can be decoupled from the motion in the transverse plane $\{x,y\}$. In the following, we will focus on the longitudinal motion of the particles.

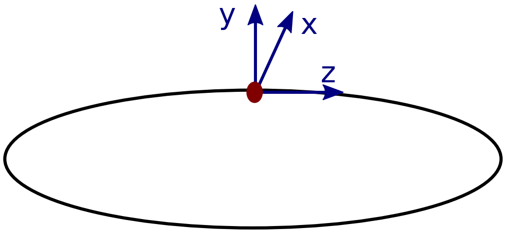

Figure 1.1 – Cartesian coordinate system used to describe the particle motion in a synchrotron.

The focusing in the longitudinal plane, as well as the acceleration, is obtained by the longitudinal component of the electric field in the rf cavities. The reference particle should be synchronized with the rf voltage, i.e., the rf phase angle $\phi = \omega_{\mathrm{rf}}\,t$ is the same every time the reference particle crosses an rf cavity, with ω_{rf} being the rf frequency. For this reason, the reference particle is often called the synchronous particle. This synchronization implies that the rf frequency must be an integer multiple of the revolution frequency:

$$\omega_{\mathrm{rf}} = h\,\omega_o, \tag{1.4}$$

where h is called the harmonic number.

During acceleration, the particle momentum increases and so does the revolution frequency. This implies that the rf frequency has to be adapted according to the synchronism condition (1.4), in addition to the adjustment of the magnetic field imposed by Eq. (1.3).

The phase of the rf voltage when a particle is passing the rf gap determines the relative longitudinal position of the particle. In this case, the phase ϕ of an arbitrary particle is the deviation from the phase of the synchronous particle, ϕ_s:

$$\phi = \phi_s + \Delta\phi. \tag{1.5}$$

In a similar way as for the phase coordinate, the energy E of a particle can be expressed relative to that of the synchronous particle, E_o, as

$$E = E_o + \Delta E. \tag{1.6}$$

The longitudinal phase-space coordinates $\{\phi,\Delta E\}$ fully describe the longitudinal motion of the particles, and are used below in the equations of motion for convenience.

1.1.1 Energy gain per turn

The electric field $\mathcal{E}$ in the rf cavity gap can be written:

$$\mathcal{E}(t) = \mathcal{E}_o \sin(\omega_{\mathrm{rf}}\, t), \tag{1.7}$$

where $\mathcal{E}_o$ is the longitudinal component of the rf field in the cavity gap (assuming that it is uniform over the gap). The argument of the sine function changes during the passage of the reference particle and can be written as a function of the synchronous phase and the velocity of the particle, $v = \beta c$, where c is the speed of light. Neglecting the change of the particle velocity during the passage we obtain:

$$\omega_{\mathrm{rf}}\, t = \phi_s + \frac{\omega_{\mathrm{rf}}}{\beta c} z. \tag{1.8}$$

The reference particle gains an energy δE_o during the passage through the rf cavity gap of length g that is [7]

$$\delta E_o = q \int_{-g/2}^{g/2} \mathcal{E}_o \sin(\phi_s + \frac{\omega_{\mathrm{rf}}}{\beta c} z)\, dz = q \mathcal{E}_o\, g\, T \sin\phi_s, \tag{1.9}$$

where T is the transit-time factor, defined as

$$T = \frac{\sin\left(\dfrac{\omega_{\mathrm{rf}}\, g}{2\,\beta\, c}\right)}{\dfrac{\omega_{\mathrm{rf}}\, g}{2\,\beta\, c}}, \tag{1.10}$$

and depending on the time it takes for a particle to cross the cavity gap. It takes into account the fact that the particle sees an averaged electric field during the passage.

The effective rf voltage amplitude seen by the synchronous particle is therefore

$$V_{\mathrm{rf}} = \mathscr{E}_o\, g\, T, \tag{1.11}$$

and it depends on the particle velocity through the transit-time factor. In a synchrotron where particles have a small spread in momentum, and especially for ultrarelativistic beams, the transit-time factor is approximately the same for all particles and we can assume that they see the same amplitude of the rf voltage V_{rf}.

In most of the synchrotrons, the energy gain per turn of the synchronous particle is small enough so that the acceleration rate can be approximated by a smooth function of time:

$$\frac{dE_o}{dt} = \frac{\omega_o}{2\pi}\, q\, V_{\mathrm{rf}} \sin\phi_s. \tag{1.12}$$

If we now consider an arbitrary particle with a phase ϕ, it gains an energy per turn that is $\delta E = q\, V_{\mathrm{rf}} \sin\phi$, and the acceleration rate for this particle can be written as

$$\frac{dE}{dt} = \frac{\omega_o}{2\pi}\, q\, V_{\mathrm{rf}} \sin\phi. \tag{1.13}$$

Using Eqs. (1.12) and (1.13) we obtain the equation of motion for the energy difference:

$$\frac{d\Delta E}{dt} = \frac{\omega_o}{2\pi}\, q\, V_{\mathrm{rf}} \left(\sin\phi - \sin\phi_s\right). \tag{1.14}$$

1.1.2 Phase slippage

In addition to the equation of motion for the energy difference (1.14), and in order to fully describe the single-particle motion, it is required another equation of motion that accounts for the time evolution of the phase angle variable ϕ.

For an arbitrary particle with a revolution frequency ω, compared to the revolution frequency of the synchronous particle ω_o, the difference in arrival time Δt between the arbitrary particle and the synchronous particle is

$$\Delta t = 2\pi\left(\frac{1}{\omega} - \frac{1}{\omega_o}\right) = -\frac{2\pi}{\omega_o}\frac{\Delta\omega}{\omega}, \tag{1.15}$$

and the phase variable can be calculated from the difference in arrival time as

$$\Delta\phi = \omega_{\text{rf}}\Delta t. \tag{1.16}$$

Assuming that the phase change over one turn is slow enough compared to the revolution frequency, we can approximate Eq. (1.16) by

$$\frac{d\phi}{dt} \simeq -h\omega_o\frac{\Delta\omega}{\omega}, \tag{1.17}$$

where it was considered that ϕ_s changes much slower than ϕ ($d\phi_s/dt \ll d\phi/dt$).

Then, by logarithmic differentiation of the expression $\omega = 2\pi\beta/C$ we get

$$\frac{\Delta\omega}{\omega} = \frac{\Delta\beta}{\beta} - \frac{\Delta C}{C}. \tag{1.18}$$

The first term on the right-hand side of the Eq. (1.18) can be calculated using the relations for the momentum $p = \gamma m_o \beta c$ and $\beta = \sqrt{1 - 1/\gamma^2}$, with γ being the Lorentz factor:

$$\frac{\Delta\beta}{\beta} = \frac{1}{\gamma^2}\frac{\Delta p}{p}. \tag{1.19}$$

The second term of the Eq. (1.18) comes from considerations of the particle motion in the transverse plane (see for example Ref. [8]), and is related to the fact that particles with different momentum have orbits of different lengths. The momentum compaction factor α depends on the optics of the accelerator lattice and determines the relation between the orbit length and the momentum of a particle in the first-order approximation as

$$\alpha = \frac{\Delta C/C}{\Delta p/p}, \tag{1.20}$$

In the majority of accelerators, α is a positive quantity, meaning that a particle with a higher momentum travels a longer distance in one turn than a particle with lower momentum; but the accelerator lattice can also be designed to obtain a negative α.

Combining Eqs. (1.17), (1.18), (1.19), and (1.20) we obtain:

$$\frac{d\phi}{dt} = -h\omega_o\left(\frac{1}{\gamma^2} - \alpha\right)\frac{\Delta p}{p}. \tag{1.21}$$

Finally, using the relation $\Delta p/p = 1/\beta^2 \Delta E/E_o$ and defining the phase slippage factor as $\eta = \alpha - 1/\gamma^2$, we obtain the second equation of motion:

$$\frac{d\phi}{dt} = \frac{h\omega_o \eta}{\beta^2 E_o} \Delta E. \tag{1.22}$$

The sign of the slippage factor defined above changes for a certain value of the particle energy, called transition energy and corresponding to a Lorentz factor $\gamma_{\mathrm{tr}} = 1/\sqrt{\alpha}$. This energy separates two different regimes. Below the transition energy ($\eta < 0$), a particle with higher momentum than the synchronous particle makes one turn faster, and vice-versa. Above the transition energy ($\eta > 0$), the opposite is true.

1.1.3 Phase stability

Combining Eqs. (1.14) and (1.22), the time evolution of the phase coordinate can be written as a second order differential equation:

$$\frac{d^2\phi}{dt^2} - \frac{h\omega_o^2 q V_{\mathrm{rf}} \eta}{2\pi \beta^2 E_o} \left(\sin\phi - \sin\phi_s\right) = 0. \tag{1.23}$$

If we analyze the motion of a particle with a phase $\phi = \phi_s + \Delta\phi$, which has a small deviation $\Delta\phi$ from the synchronous phase, Eq. (1.23) can be linearized around ϕ_s and we get

$$\frac{d^2\Delta\phi}{dt^2} + \omega_{s0}^2 \Delta\phi = 0. \tag{1.24}$$

This is the equation of a harmonic oscillator, with the angular frequency of the system

$$\omega_{s0} = \sqrt{-\frac{h\omega_o^2 q V_{\mathrm{rf}} \eta \cos\phi_s}{2\pi \beta^2 E_o}}, \tag{1.25}$$

which is known as the synchrotron frequency.

In order for the oscillating system to be stable, the expression under the square root in Eq. (1.25) must be a positive quantity. As all the parameters are positive except η and $\cos\phi_s$, we get that the stability condition is

$$\eta \cos\phi_s < 0. \tag{1.26}$$

In the stationary case without acceleration or energy losses, the voltage seen by the synchronous particle is zero and therefore $\sin\phi_s = 0$. As a consequence, the stability condition is different depending on the sign of η. Below the transition energy $\eta < 0$, then the synchronous phase should be $\phi_s = 0$. Above the transition energy, the sign of the slippage factor changes ($\eta > 0$) and the synchronous phase should be shifted to $\phi_s = \pi$.

During the acceleration, the synchronous particle should see a positive voltage, which implies that $\sin\phi_s > 0$. Again, the stability condition is different below and above the transition energy. Below transition, the synchronous phase should be in the range $0 < \phi_s < \pi/2$, and above transition $\pi/2 < \phi_s < \pi$. A similar reasoning leads to the stability condition for deceleration.

1.1.4 The synchrotron Hamiltonian

The synchrotron motion can also be described using the Hamiltonian formalism. For that purpose, canonical coordinates must be used. There are different possible choices, and here we are going to use the phase-space coordinates $(\phi, \Delta E/\omega_o)$. The Hamiltonian of a particle, in this case, can be constructed from the equations of motion taking into account the following relations [9, 10]:

$$\frac{d}{dt}\left(\frac{\Delta E}{\omega_o}\right) = -\frac{\partial H}{\partial \phi} \tag{1.27}$$

$$\frac{d\phi}{dt} = \frac{\partial H}{\partial(\Delta E/\omega_o)}. \tag{1.28}$$

Then we can obtain the Hamiltonian by integration:

$$H = \int \frac{d\phi}{dt}\, d(\Delta E/\omega_o) - \int \frac{d}{dt}\left(\frac{\Delta E}{\omega_o}\right) d\phi, \tag{1.29}$$

where the second term of the right-hand side is known as the potential well U. The potential well can be defined for an arbitrary voltage $V(\phi)$ as

$$U(\phi) = -\frac{q}{2\pi}\int \left[V(\phi) - V(\phi_s)\right] d\phi. \tag{1.30}$$

Finally, the Hamiltonian can be written as

$$H = \frac{h\omega_o^2\eta}{2\beta^2 E_o}\left(\frac{\Delta E}{\omega_o}\right)^2 + U(\phi) + \mathscr{C}, \tag{1.31}$$

where $\mathscr{C}$ is an integration constant. The integration constant can be calculated by imposing, for example, that $H(\phi = \phi_s, \Delta E/\omega_o = 0) = 0$. For the case of a single rf system with a sinusoidal rf wave, the Hamiltonian can be expressed as

$$H = \frac{h\omega_o^2\eta}{2\beta^2 E_o}\left(\frac{\Delta E}{\omega_o}\right)^2 + \frac{qV_{\mathrm{rf}}}{2\pi}\left[\cos\phi - \cos\phi_s + (\phi - \phi_s)\sin\phi_s\right]. \tag{1.32}$$

1.1.5 The rf bucket

The particle trajectory described by the Hamiltonian (1.32) has two different types of fixed points, when the derivative of the coordinates with respect to time is zero ($d\phi/dt = 0$ and

$dE/dt = 0$). From Eq. (1.22), we see that $\Delta E/\omega_o = 0$ for the fixed points. From Eq. (1.14), there are two possibilities: $\phi = \phi_s + 2k\pi$ and $\phi = (2k+1)\pi - \phi_s$, for $k = 0, 1, 2\ldots$ The first ones are called stable fixed points and the trajectory of a particle close to one of those points is an ellipse. The second ones are called unstable fixed points and if a particle in one of those points is slightly perturbed, it moves away describing a hyperbola near the unstable fix point and then it can oscillate [8]. Figure 1.2 shows the two types of fixed points and different trajectories both for a stationary and an accelerating rf bucket.

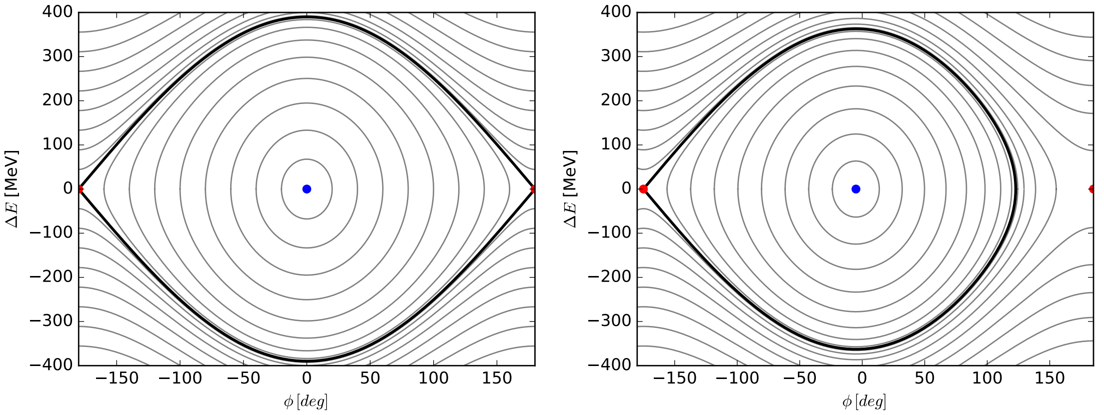

(a) Stationary bucket

(b) Accelerating bucket

Figure 1.2 – Particle trajectories in phase space in the LHC at 450 GeV and 6 MV rf voltage for the stationary case (left) and during acceleration for $\phi_s = 4.8$ deg (right). The solid black line shows the separatrix of the rf bucket. Blue points are stable fixed points and red points are unstable fixed points.

It is possible to define a region of the phase space where the motion of the particles is stable and describes closed trajectories around a stable fixed point. Acceleration of bunched beams is only possible for particles inside this region, which is called an rf bucket. The limit of this region is known as the separatrix, also shown in Fig. 1.2.

The separatrix can be calculated from Eq. (1.31), considering that the particle energy corresponding to the Hamiltonian is constant over a trajectory. The separatrix passes through the unstable fixed point $(\pi - \phi_s, 0)$, and therefore the Hamiltonian value at the separatrix is

$$H_{\text{sep}} = U(\pi - \phi_s). \tag{1.33}$$

The trajectory of the separatrix in phase space is determined by $H = H_{\text{sep}}$, which leads to:

$$\frac{\Delta E}{\omega_o} = \sqrt{\frac{2\beta^2 E_o}{h\omega_o^2 \eta}\left[H_{\text{sep}} - U(\phi)\right]}. \tag{1.34}$$

The maximum of this trajectory, which is reached for $U(\phi) = 0$, gives the bucket height ΔE_{max}. The formula (1.34) used to define the separatrix can be used for the trajectory of any particle by replacing H_{sep} by H_i, which is the value of the Hamiltonian at the trajectory of the particle i.

The phase-space area enclosed by a trajectory is

$$\tilde{A} = \oint \frac{\Delta E}{\omega_o}\, d\phi. \tag{1.35}$$

which is a Poincaré integral invariant, as $\Delta E/\omega_o$ and ϕ are canonical coordinates, and therefore a constant of motion [11].

The phase-space area is usually expressed in units of eVs, and can be found from $\tilde{A}$ as

$$A = \oint \Delta E\, dt = \frac{\tilde{A}}{h}. \tag{1.36}$$

In particular, the phase-space area inside the separatrix is called the bucket area. For a stationary bucket in a single rf system, the bucket area (in eVs) can be calculated analytically [8]:

$$A_B = \oint \sqrt{\frac{2\beta^2 E_o}{h^3 \omega_o^2 \eta}\left[H_{\mathrm{sep}} - U(\phi)\right]}\, d\phi = 8\sqrt{\frac{2\beta^2 E_o\, q\, V_{\mathrm{rf}}}{h^3 \omega_o^2 |\eta| \pi}}. \tag{1.37}$$

1.1.6 Bunch parameters

Synchrotrons are usually operated, at least during acceleration, with bunched beams. A bunch is a group of particles that perform synchrotron oscillations inside an rf bucket. The number of particles forming a bunch depends on the accelerator design and its applications, and can typically vary between 10^9 and 10^{15}.

Longitudinal emittance

In order to avoid particle losses, the particles of a bunch are often not distributed over the full rf bucket but restricted to a certain fraction of the phase space. The phase-space area filled by a bunch is called the full longitudinal emittance ε. The full emittance can be calculated from the area enclosed by a single-particle trajectory that contains all bunch particles using Eq. (1.36):

$$\varepsilon = \oint \frac{\Delta E}{h\omega_o}\, d\phi. \tag{1.38}$$

Liouville's theorem [12] states that the particle distribution function of a bunch in phase space, $F(\phi, \Delta E/\omega_o)$, is constant along the trajectories in a conservative system. This implies that the longitudinal emittance is an invariant and the distribution function can be written as a function of the Hamiltonian:

$$F(\phi, \frac{\Delta E}{\omega_o}) = F(H). \tag{1.39}$$

The longitudinal emittance can also be preserved during acceleration and during changes of the accelerator parameters, provided that all changes are done adiabatically. The condition for adiabatic motion is [8]

$$\alpha_{\mathrm{ad}} = \frac{1}{\omega_s^2}\left|\frac{d\omega_s}{dt}\right| \ll 1, \tag{1.40}$$

where α_{ad} is the adiabaticity coefficient. For small values of α_{ad}, the parameters of the Hamiltonian change slowly and therefore the Hamiltonian can be considered quasi-static.

Under non-adiabatic changes, the emittance can be increased as a result of beam instabilities or by some techniques, for example by injecting band-limited noise in the rf voltage amplitude or phase [13, 14]. Some mechanisms can also reduce the emittance, as synchrotron radiation or cooling techniques (non-conservative systems).

Particle distribution in phase space

The particle distribution can be very different from one accelerator to another, and even for different modes of operation of a given accelerator. There are many analytical distributions that are used for theoretical calculations and macroparticle simulations, and some examples of distributions that can be used for proton beams are [15]

$$\text{Binomial:} \qquad F(H) = F_o\left(1-\frac{H}{H_o}\right)^n \tag{1.41}$$

$$\text{Parabolic amplitude:} \qquad F(H) = F_o\left(1-\frac{H}{H_o}\right) \tag{1.42}$$

$$\text{Parabolic line density:} \qquad F(H) = F_o\left(1-\frac{H}{H_o}\right)^{1/2} \tag{1.43}$$

where F_o is a normalization factor, n is a free parameter, and H_o is the value of the Hamiltonian along the trajectory that encloses all particles. These distributions are shown in Fig. 1.3.

Another distribution that is often used is the Gaussian distribution, also shown in Fig. 1.3 and defined as

$$F(H) = F_o\, e^{-2H/H_o}. \tag{1.44}$$

The Gaussian distribution is a special case, as it has infinitely long tails that fill the rf bucket. In this case, H_o corresponds to the value of the Hamiltonian of a trajectory that contains 4-σ (~95%) of the particles.

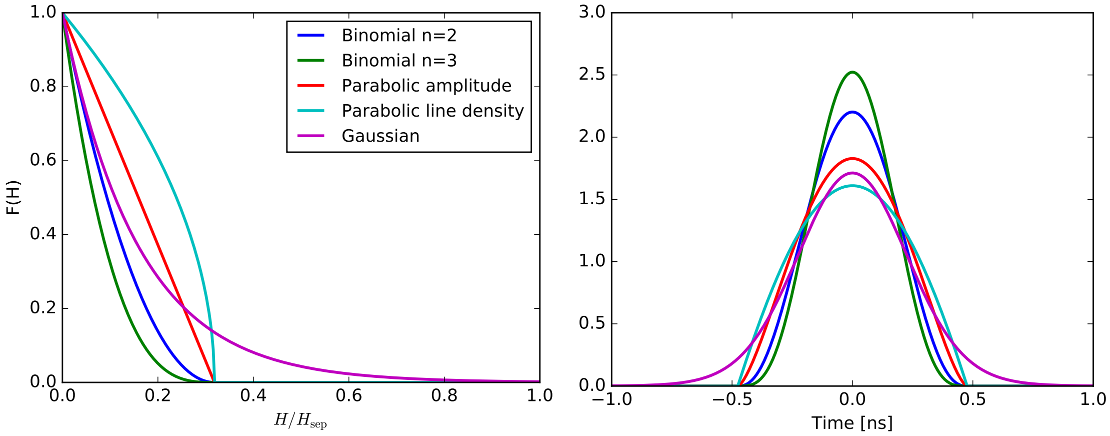

(a) Distribution function

(b) Line density

Figure 1.3 – Example of different distribution functions (left) and their corresponding line density in an accelerator with a single rf system (right).

Bunch length

As there is no direct method to measure the longitudinal emittance in circular accelerators, a parameter that is generally used in measurements is the bunch length. If all accelerator parameters are known, including the potential-well distortion effect described later in this chapter, the bunch length can be used to infer the emittance.

The full bunch length τ corresponds to the maximum phase excursion performed by the particles of a bunch. In this thesis, it is expressed in units of time.

In many practical situations, the particle distribution is close to a Gaussian (1.44) with tails that completely fill the rf bucket. In these cases, it is common to use a statistical quantity to define the bunch length. For example, the rms bunch length τ_{rms} can be defined as the rms of the phase oscillation amplitude of all the particles.

Other definitions of bunch length can be calculated from the projection of the distribution function on the phase axis, known as the bunch profile or line density $\lambda(\phi)$:

$$\lambda(\phi) = \lambda_o \int_{-\infty}^{\infty} F\left(\phi, \frac{\Delta E}{\omega_o}\right) d\left(\frac{\Delta E}{\omega_o}\right), \tag{1.45}$$

where λ_o is a normalization factor that can be found from

$$\int_{-\infty}^{\infty} \lambda(t)\, dt = 1. \tag{1.46}$$

Figure 1.3 shows the line densities corresponding to the distribution functions defined above, calculated for an accelerator with a single rf system.

The line density can be fitted by any function, and one example is the Gaussian fit. The value of σ obtained from the fit can be used to compute the 4-σ bunch length as $\tau_{4\sigma} = 4\sigma$. The full width at half maximum τ_{FWHM} of the line density can also be used to calculate σ for Gaussian bunches, using the following relation:

$$\tau_{4\sigma} = \frac{2}{\sqrt{2\ln 2}}\,\tau_{\mathrm{FWHM}}. \tag{1.47}$$

In the following, we use the FWHM method to calculate $\tau_{4\sigma}$ from measurements, even for non-Gaussian bunches.

These definitions of bunch length can be used to compute the longitudinal emittance in cases when the full emittance is not practical (bunches with long tails). The emittance is defined in these cases as the phase-space area enclosed by the trajectory of a particle which performs synchrotron oscillations with an amplitude equals to the bunch length.

1.1.7 Synchrotron frequency distribution

In Section 1.1.3, the synchrotron frequency was calculated for small amplitude oscillations by linearization of the phase around the synchronous phase. However, due to the non-linearities of the rf voltage each particle performs synchrotron oscillations at a different frequency depending on the amplitude of the oscillations.

From the second equation of motion (1.22), the synchrotron period can be calculated by integrating dt over a particle trajectory:

$$T_s = \oint dt = \oint \frac{\beta^2 E_o}{h\omega_o^2\eta}\,\frac{1}{(\Delta E/\omega_o)}\,d\phi, \tag{1.48}$$

and the synchrotron frequency f_s can be expressed as a function of the Hamiltonian of a particle as

$$f_s(H) = \frac{1}{T_s(H)} = \left[\sqrt{\frac{\beta^2 E_o}{2h\omega_o^2\eta}}\oint \frac{d\phi}{\sqrt{H-U(\phi)}}\right]^{-1}. \tag{1.49}$$

Equation (1.49) can be used for any potential well and it is used in Chapter 4 for double rf operation. For the stationary case (no acceleration) in an accelerator with a single rf system, the synchrotron frequency distribution can be calculated as [10]

$$f_s(\hat{\phi}) = f_{so}\,\frac{\pi}{2K\big(\sin(\hat{\phi}/2)\big)}, \tag{1.50}$$

where $\hat{\phi}$ is the phase amplitude of the synchrotron oscillations and $K(\phi)$ is the complete elliptic integral of the first kind:

$$K(\phi) = \int_0^{\frac{\pi}{2}} \frac{d\theta}{\sqrt{1-\phi^2 \sin^2\theta}}. \tag{1.51}$$

For small amplitude oscillations Eq. (1.50) can be approximated by

$$f_s(\hat{\phi}) \simeq f_{so}\left(1-\frac{\hat{\phi}^2}{16}\right). \tag{1.52}$$

Figure 1.4 shows the normalized synchrotron frequency distribution calculated using Eq. (1.50) and compared to Eq. (1.52).

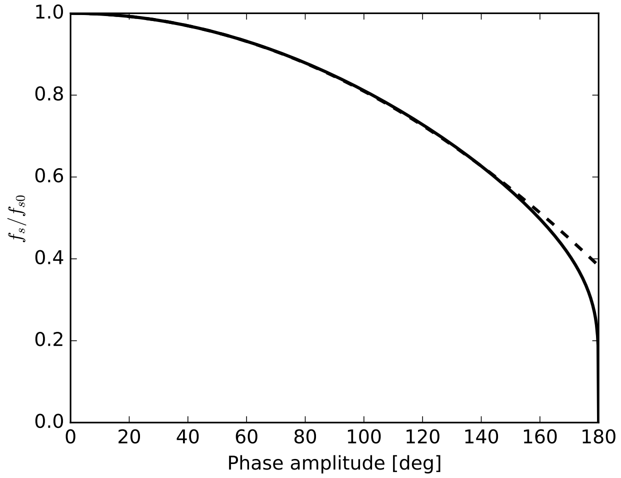

Figure 1.4 – Normalized synchrotron frequency distribution with respect to the phase oscillation amplitude in a single rf system calculated using Eq. (1.50) (solid line) the approximated formula (1.52) (dashed line).

The spread in synchrotron frequencies can produce a natural stabilizing mechanism, known as Landau damping (see Section 1.2.3), which is very important for the operation of synchrotrons.

Another consequence of the spread in synchrotron frequencies is the filamentation process of a mismatched bunch. A bunch can be mismatched at injection when it is not injected into the center of the rf bucket (energy or phase error) or when it comes from an accelerator with a different rf bucket parameters (e.g., length or height). The mismatch can also be produced by a non-adiabatic change of the accelerator parameters, as for example the rf voltage (amplitude, phase, or frequency). In those cases, the spread in synchrotron frequencies produces a dilution of the phase-space density as the particles follow the trajectories defined by the Hamiltonian. The filamentation process results in a longitudinal emittance increase of the bunch.

1.1.8 Action and Angle coordinates

In some situations, it can be more convenient to express the Hamiltonian using another set of canonical coordinates called action-angle (J,ψ) [9, 10].

The action coordinate can be defined as

$$J = \frac{1}{2\pi} \oint \left(\frac{\Delta E}{h\omega_o} \right) d\phi, \tag{1.53}$$

which, when comparing with Eq. (1.35), is proportional to the phase-space area enclosed by a particle trajectory. For a conservative system, J is a constant of motion and the first Hamilton equation is

$$-\frac{\partial H}{\partial \psi} = \frac{dJ}{dt} = 0. \tag{1.54}$$

This implies that the Hamiltonian only depends on the action. For this reason, in the stationary case, the particle distribution in phase space defined in Section 1.1.6 can also be expressed as a function of the action:

$$F(\phi, \frac{\Delta E}{\omega_o}) = F(J). \tag{1.55}$$

The second Hamilton equation can be used to calculate the angle coordinate:

$$\frac{\partial H}{\partial J} = \frac{d\psi}{dt}. \tag{1.56}$$

The right-hand side term of Eq. (1.56) is equal to the synchrotron frequency. This relation can be used to calculate the angular synchrotron frequency distribution as

$$\omega_s(J) = \frac{\partial H}{\partial J}. \tag{1.57}$$

1.2 Wakefields and impedances

Until now we have considered the single-particle motion in a synchrotron in the longitudinal plane without considering neither the interaction with other particles nor with the vacuum chamber and other accelerator components. These interactions are nevertheless of special importance for the study of the particle motion in a synchrotron, as they can degrade and limit the accelerator performance.

In the following, we consider a particle traveling at approximately the speed of light ($v = \beta c$, $\beta \approx 1$) and that is not affected by its own induced electromagnetic fields. In this case, the electric field generated by the particle is perpendicular to the motion of the particle and there is no electric field in front of the particle. When the particle traverses a discontinuity in the vacuum chamber (change of chamber cross section, rf cavity...) or a vacuum chamber made of a not perfectly conducting material, an electromagnetic field is excited behind the particle called wakefield (see e.g., [16]).

In order to study the effect of the wakefields, we consider a witness particle that is traveling at a constant distance Δz from the source particle and with the same speed. As the self-excited magnetic field is perpendicular to the motion, only the electric field affects the witness particle in the longitudinal plane. This particle experiences an impulse, which can be described by the longitudinal wake function $W(\Delta z)$ in terms of induced voltage per unit charge, defined as the integral of the electric field in the longitudinal direction $E_z(z,t)$ over the accelerator component of interest:

$$W(\Delta z) = -\frac{1}{q}\int_0^L E_z(z, t = \frac{z+\Delta z}{\beta c})\, dz, \tag{1.58}$$

where L is the length of the component. The wake function can also be defined as a function of the difference in arrival time between the trailing particle and the source particle:

$$\Delta t = -\frac{\Delta z}{\beta c} = \frac{\Delta \phi}{h \omega_o}, \tag{1.59}$$

which is used below for convenience.

For a bunch with a line density $\lambda(t)$, the voltage induced by the bunch (also called wake potential) can be calculated as

$$V_{\text{ind}}(t) = -N_b\, q\, \lambda(t) * W(t) = -N_b\, q \int_{-\infty}^{\infty} \lambda(\tau)\, W(t-\tau)\, d\tau, \tag{1.60}$$

where the symbol $*$ denotes a convolution and $\lambda(t)$ should be normalized as

$$\int_{-\infty}^{\infty} \lambda(t)\, dt = 1. \tag{1.61}$$

As a result of the interaction of the beam with the accelerator impedance, the particles see a total voltage V_t that is the sum of the rf voltage V_{rf} and the induced voltage V_{ind}:

$$V_t(t) = V_{\text{rf}}(t) + V_{\text{ind}}(t). \tag{1.62}$$

In certain cases, it can be more convenient to perform the calculations in the frequency domain, as the convolution in the time domain corresponds to a multiplication in the frequency domain. The Fourier transform of the wake function is known as the beam-coupling impedance $Z(\omega)$, or simply impedance, which is expressed in units of ohm [16]:

$$Z(\omega) = \int_{-\infty}^{\infty} W(t)\, e^{-j\omega t}\, dt. \tag{1.63}$$

Given that the wake function is real, the impedance is therefore a Hermitian function. The real part of the impedance is an even function and is often called resistive impedance; whereas the imaginary part is an odd function and is referred to as the reactive impedance. Depending on the sign of the reactive impedance it can be either inductive or capacitive. According to the sign convention used in Eqs. (1.58) and (1.63), a positive imaginary impedance is inductive and otherwise it is capacitive. The opposite sign convention is used in some literature (e.g., [17]).

The induced voltage defined by Eq. (1.60) can also be calculated in the frequency domain, taking into account that a convolution in the time domain transforms to a multiplication in the frequency domain:

$$V_{\text{ind}}(t) = -\frac{N_b\, q}{2\pi} \int_{-\infty}^{\infty} Z(\omega)\, \Lambda(\omega)\, e^{j\omega t}\, d\omega, \tag{1.64}$$

where $Z(\omega)$ is the longitudinal impedance and $\Lambda(\omega)$ is the beam spectrum, defined as the Fourier transform of the line density:

$$\Lambda(\omega) = \int_{-\infty}^{\infty} \lambda(t)\, e^{-j\omega t}\, dt. \tag{1.65}$$

Depending on the time the wakefield lasts after a bunch passage and the distance between bunches, we can distinguish between short-range (single-bunch effects) and long-range wakefields (multi-bunch effects). Examples of short-range wakefields are the resistive wall impedance of the vacuum chamber or the space-charge effect, the latter being the result of the repulsive force between particles of the same charge inside the bunch. Long-range wakefields are often produced by cavity-like objects and the main representative example is the rf cavities.

For long-range wakefields, the inherent periodicity of a circular accelerator must be taken into account. In the stationary case, for a non-varying beam spectrum $\Lambda_o(\omega)$, the induced voltage can be expressed as [15]

$$V_{\text{ind}}(t) = -\frac{N_b\, q\, \omega_o}{2\pi} \sum_{p=-\infty}^{\infty} Z(p\omega_o)\, \Lambda_o(p\,\omega_o)\, e^{j\, p\omega_o t}. \tag{1.66}$$

The impedance of each element can be estimated from electromagnetic simulations, bench measurements, or beam measurements. A useful approach is to model the impedance of each element, or even the full machine impedance, with a resonator model. The impedance of a resonator is

$$Z(\omega) = \frac{R_{sh}}{1 + j\,Q\left(\frac{\omega}{\omega_r} - \frac{\omega_r}{\omega}\right)}, \tag{1.67}$$

where R_{sh} is the shunt impedance, ω_r is the resonator frequency, and Q is the quality factor.

The corresponding wake function of a resonator is given by [16]

$$W(t) = \begin{cases} 0 & \text{if } t < 0, \\ \alpha\, R_{sh} & \text{if } t = 0, \\ 2\,\alpha\, R_{sh}\, e^{-\alpha\, t}\left[\cos(\bar{\omega}\, t) - \frac{\alpha}{\bar{\omega}} \sin(\bar{\omega}\, t)\right] & \text{if } t > 0, \end{cases} \tag{1.68}$$

where $\alpha = \omega_r/(2\,Q)$ and $\bar{\omega} = \sqrt{\omega_r^2 - \alpha^2}$. Depending on the decay rate α, the wakefield produced can be long-range (narrow-band resonator) or short-range (broad-band resonator).

1.2.1 Potential-well distortion

In the stationary case, for a stable bunch, the induced voltage distorts the rf potential well with respect to the ideal case $V_{\text{ind}}(\phi) = 0$, causing a shift of the stable fixed point and modifying the effective voltage seen by the particles. The latter leads to a shift in the synchrotron frequency and a change of the bunch length. These effects can usually be quantified and used to characterize the accelerator impedance, as we will see in later chapters.

In order to analyze the effects mentioned above, we consider the case with a single rf system and a bunch that is short compared to the rf wavelength. Then we can superimpose the impedance effect in Eq. (1.24) as

$$\frac{d^2\Delta\phi}{dt^2} + \omega_{so}^2 \Delta\phi = -\frac{\omega_{so}^2}{V_{\text{rf}}\cos\phi_s} V_{\text{ind}}(\Delta\phi). \tag{1.69}$$

Now combining this equation with Eq. (1.66) and expanding the exponential term around $\Delta\phi$, we get:

$$\frac{d^2\Delta\phi}{dt^2} + \omega_{so}^2 \Delta\phi = \frac{N_b\, q\, \omega_o\, \omega_{so}^2}{2\pi\, V_{\text{rf}}\cos\phi_s} \sum_{p=-\infty}^{\infty} Z(p\omega_o)\, \Lambda_o(p\,\omega_o) \left[1 + \frac{j\, p\, \Delta\phi}{h} - \frac{(p\,\Delta\phi/h)^2}{2} + \ldots\right]. \tag{1.70}$$

Synchronous phase shift

The first term of the expansion in Eq. (1.70) introduces a shift in the synchronous phase $\Delta\phi_s$. Taking into account that the wake function is real, then the real part of the impedance is even and the imaginary part is odd. In addition, we assume that the bunch line density is an even function of $\Delta\phi$, which is a good approximation for proton bunches with slow acceleration. Since it is also a real function, then the bunch spectrum is a real, even function.

With these considerations, the synchronous phase shift can be expressed as a function of the real part of the impedance [15]:

$$\Delta\phi_s = \frac{N_b\, q\, \omega_o}{2\pi\, V_{\mathrm{rf}} \cos\phi_s} \sum_{p=-\infty}^{\infty} \mathrm{Re}\{Z(p\omega_o)\}\, \Lambda_o(p\,\omega_o). \tag{1.71}$$

The physical interpretation is that the energy from the beam is dissipated in the resistive impedance and the synchronous phase is shifted so that the energy can be restored by the rf system.

A measurement of the synchronous phase shift could be used to probe the real part of the machine impedance. However, this phase shift is difficult to measure in practice, as it applies only for particles with small-amplitude phase oscillations. Other particles experience a different energy loss from the interaction with the impedance, and therefore a different phase shift.

Instead, one can measure the average energy loss over all the particles, seen as a shift of the bunch centroid with respect to the rf voltage $\Delta\phi_b$. This shift corresponds to an energy gain per turn that is compensating for the energy loss due to the interaction with the resistive impedance and can be written as

$$\Delta E_{b,\mathrm{rf}} = N_b\, q\, V_{\mathrm{rf}} \left[\sin(\phi_s + \Delta\phi_b) - \sin(\phi_s)\right] \simeq N_b\, q\, V_{\mathrm{rf}} \cos(\phi_s)\, \Delta\phi_b, \tag{1.72}$$

assuming that $\Delta\phi_b$ is a small value. The energy change due to the resistive impedance can be calculated through the loss factor $k_{||}$ [16]:

$$\Delta E_{b,Z} = -(N_b\, q)^2\, k_{||}, \tag{1.73}$$

with the minus sign meaning that the energy is lost and the loss factor defined as

$$k_{||} = \frac{\omega_o}{2\pi} \sum_{p=-\infty}^{\infty} \mathrm{Re}\{Z(p\omega_o)\} \left|\Lambda(p\,\omega_o)\right|^2, \tag{1.74}$$

where $|\Lambda(\omega)|^2$ is the power spectral density of the bunch. Here only the real part of the impedance is displayed as $|\Lambda(\omega)|^2$ is real and even.

Combining the last three equations and taking into account that $\Delta E_{b,\mathrm{rf}} + \Delta E_{b,Z} = 0$, we finally get that the bunch phase shift is

$$\Delta\phi_b = \frac{N_b\, q\, \omega_o}{2\pi\, V_{\mathrm{rf}} \cos\phi_s} \sum_{p=-\infty}^{\infty} \mathrm{Re}\{Z(p\omega_o)\} \left|\Lambda(p\,\omega_o)\right|^2. \tag{1.75}$$

The bunch phase shift is used in Chapter 3 to probe the resistive impedance of the LHC, and a similar approach is used in Chapter 5 to estimate the e-cloud in the LHC.

Synchrotron frequency shift

Similarly to the synchronous phase shift, the second term of the expansion in Eq. (1.70) is accountable for an incoherent synchrotron frequency shift [15]:

$$\frac{\omega_s^2 - \omega_{so}^2}{\omega_{so}^2} = \frac{N_b\, q\, \omega_o}{2\pi\, V_{\mathrm{rf}} \cos\phi_s} \sum_{p=-\infty}^{\infty} p\, \mathrm{Im}\{Z(p\omega_o)\}\, \Lambda_o(p\,\omega_o). \tag{1.76}$$

In this case, the same considerations as for the derivation of Eq. (1.71) can be applied. We take into account that the term p in Eq. (1.76) is odd and the sum depends only on the imaginary part of the impedance.

For a small synchrotron frequency shift $\Delta\omega_s = \omega_s - \omega_{so} << \omega_{so}$, as it is the case in the LHC, and assuming an inductive impedance with a linear dependence on frequency ($\mathrm{Im}Z/n = \mathrm{const}$, where $n = \omega/\omega_o$), then Eq. (1.76) can be approximated by

$$\frac{\Delta\omega_s}{\omega_{so}} \simeq \frac{N_b\, q\, \omega_o}{4\pi\, V_{\mathrm{rf}} \cos\phi_s} \mathrm{Im}Z/n \sum_{p=-\infty}^{\infty} p^2\, \Lambda_o(p\,\omega_o). \tag{1.77}$$

Measurements of the synchrotron frequency shift can therefore be used to estimate the reactive accelerator impedance. Different measurement methods are possible, and some of them, used in the LHC, will be described in Chapter 3.

Bunch lengthening

From Eq. (1.25), we get that the synchrotron frequency scales with the square root of the rf voltage:

$$\omega_{so} \propto \sqrt{V_{\mathrm{rf}}}. \tag{1.78}$$

The synchrotron frequency shift is related to the fact that the total voltage seen by the beam is modified by the induced voltage and the effective voltage is

$$V_{\mathrm{eff}} = V_{\mathrm{rf}} \left(\frac{\omega_s}{\omega_{so}}\right)^2. \tag{1.79}$$

For a synchrotron operating above transition and with an inductive impedance $\mathrm{Im}Z/n > 0$, as it is the case of the LHC, the effective voltage is smaller than the actual rf voltage.

Given a fixed longitudinal emittance, the bunch length therefore depends on the intensity. Taking into account the synchronous phase shift, the bunch length τ changes with respect to the zero-intensity bunch length τ_o as [15]

$$\left(\frac{\tau}{\tau_o}\right)^2 = \frac{\omega_{so}}{\omega_s} \sqrt{\frac{\cos\phi_s}{\cos(\phi_s + \Delta\phi_s)}}. \tag{1.80}$$

1.2.2 Instabilities

Besides the incoherent effects resulting from the potential-well distortion, the interaction of the beam with the accelerator impedance can also excite a coherent motion of the particles which can lead to beam instabilities.

Vlasov equation

Now we are interested in the time evolution of the particle distribution in phase space $F(\phi, \Delta E/\omega_o)$, which is described by the Liouville's theorem [12]. This theorem states that, in a collision-less system and in the absence of any damping mechanism, the distribution function is constant along the trajectories of the system:

$$\frac{dF}{dt} = 0. \tag{1.81}$$

The previous expression can also be written as a function of the phase-space coordinates:

$$\frac{\partial F}{\partial t} + \frac{\partial F}{\partial \phi}\frac{d\phi}{dt} + \frac{\partial F}{\partial(\Delta E/\omega_o)}\frac{d(\Delta E/\omega_o)}{dt} = 0, \tag{1.82}$$

which is known as the Vlasov equation [12].

For lepton accelerators, where synchrotron radiation damping is dominant, the Fokker-Planck equation should be considered instead [18].

Perturbation approach

A coherent motion of the bunch caused by the induced voltage due to the machine impedance can be treated as a perturbation F_p added to the stationary distribution function $F_o(H)$:

$$F\left(\phi, \frac{\Delta E}{\omega_o}, t\right) = F_o(H) + F_p\left(\phi, \frac{\Delta E}{\omega_o}, t\right). \tag{1.83}$$

Note that the distribution function depends on time and that the stationary distribution function should fulfill the Vlasov equation, taking into account that $\partial F_o/\partial t = 0$:

$$\frac{\partial F_o}{\partial \phi}\frac{d\phi}{dt} + \frac{\partial F_o}{\partial(\Delta E/\omega_o)}\frac{d(\Delta E/\omega_o)}{dt} = 0. \tag{1.84}$$

In a similar way, the line density can be expressed as the sum of a stationary term and a perturbation:

$$\lambda(\phi, t) = \lambda_o(\phi) + \lambda_p(\phi, t), \tag{1.85}$$

where the line density perturbation can be calculated as

$$\lambda_p(\phi,t) = \int_{-\infty}^{\infty} F_p\left(\phi, \frac{\Delta E}{\omega_o}, t\right) d\frac{\Delta E}{\omega_o}. \tag{1.86}$$

Finally, the total voltage seen by the particles is

$$V(\phi,t) = V_{\mathrm{rf}}(\phi) + V_{\mathrm{ind},o}(\phi) + V_{\mathrm{ind},p}(\phi,t), \tag{1.87}$$

where $V_{\mathrm{ind},o}(\phi)$ is the stationary component of the induced voltage, which produces the potential-well distortion described above, and $V_{\mathrm{ind},p}(\phi,t)$ is a perturbation that can be computed from the line density perturbation using Eq. (1.60).

Taking into account Eq. (1.84) and considering only the linear terms in the perturbation, the Vlasov equation can be written as

$$\frac{\partial F_p}{\partial t} + \frac{\partial F_p}{\partial \phi}\frac{d\phi}{dt} + \frac{\partial F_p}{\partial \Delta E/\omega_o}\frac{q}{2\pi}\left[V_{\mathrm{rf}}(\phi) + V_{\mathrm{ind},o}(\phi)\right] + \frac{\partial F_o}{\partial \Delta E/\omega_o}\frac{q}{2\pi}V_{\mathrm{ind},p}(\phi,t) = 0. \tag{1.88}$$

Equation (1.88) is called the linearized Vlasov equation, which can also be written as a function of the action-angle coordinates as [19]:

$$\frac{\partial F_p}{\partial t} + \omega_s(J)\frac{\partial F_p}{\partial \psi} - \frac{\partial U_{\mathrm{ind},p}}{\partial \psi}\frac{dF_o}{dJ} = 0, \tag{1.89}$$

where $U_{\mathrm{ind},p}(\phi,t)$ is an addition to the potential generated by the perturbation, calculated using Eq. (1.30):

$$U_{\mathrm{ind},p}(\phi,t) = -\frac{q}{2\pi}\int \left[V_{\mathrm{ind},p}(\phi,t) - V_{\mathrm{ind},p}(\phi_s,t)\right] d\phi. \tag{1.90}$$

The solutions of Eq. (1.89) determine the stability of the system for a given total potential well $U(\phi)$ and a stationary distribution function $F_o(H)$.

Coherent modes of oscillation

For a perturbation small as compared to the rf voltage, $V_{\mathrm{ind},p}(\phi) \ll V_{\mathrm{rf}}(\phi)$, the last term in Eq. (1.89) can be neglected and the solutions of the linearized Vlasov equation can be written in the form [19]:

$$F_{p,n}(J,\psi) = R_{m,n}(J)\, e^{jm\psi}\, e^{-j\omega t}, \tag{1.91}$$

where m is the azimuthal-mode number, which corresponds to oscillations at frequencies $\omega = m\omega_s(J)$ defined by potential-well distortion; the integer n describes another degree of freedom with perturbations in J; and $R_{m,n}$ determines the radial dependence of the solutions.

The azimuthal modes can be classified as dipole ($m = 1$), quadrupole ($m = 2$), sextupole ($m = 3$), etc. For instance, a dipole mode oscillation can be observed if the rf phase is shifted, and a quadrupole when a bunch is injected in a mismatched rf bucket.

In the general case, for a large number of particles, the last term in Eq. (1.89) has to be considered as well. Under those conditions, the solution of Eq. (1.89) can be presented as

$$F_p(J,\psi) = \sum_n F_{p,n}(J,\psi) = \sum_n R_{m,n}(J)\, e^{j\,m\psi}\, e^{-j\omega t}, \tag{1.92}$$

and ω becomes a complex number. If $\mathrm{Im}\omega > 0$, then an exponential growth appears and the beam is unstable. These solutions can be obtained and analyzed for different particle distributions and impedances. Examples can be found in Ref. [20].

1.2.3 Landau damping

In synchrotrons, the beam can eventually be stabilized by the so-called Landau damping mechanism. The theory of Landau damping was first derived for plasma and it describes the damping of longitudinal space-charge waves [21], which is the result of decoherence from the spread in the particle oscillation frequencies. A similar effect was later observed in particle accelerators [22], and since then it has proven to be an important mechanism for beam stabilization in many accelerators.

In the longitudinal plane, for bunched beams, Landau damping is provided by the spread in synchrotron frequencies inside a bunch; while for debunched beams, it is obtained through the spread in revolution frequency connected to the energy spread of the particles.

A stability threshold can be defined from the spread in synchrotron frequencies that is not enough to guarantee Landau damping, which occurs when the coherent frequency shift of the azimuthal mode m is smaller than one fourth of the synchrotron frequency spread [23]. A similar condition can be found for an accelerator with a purely reactive impedance $\mathrm{Im}Z/n$ and with a small resistive impedance treated as a perturbation [24], and the stability criterion can be expressed as

$$\mathrm{Im}Z/n < \frac{F\,|\eta|\,E}{q^2\,N_b\,\beta^2}\left(\frac{\Delta E}{E}\right)^2 \frac{\Delta\omega_s}{\omega_s}\,\tau, \tag{1.93}$$

where F is a form factor defined by the particle distribution, $\Delta\omega_s/\omega_s$ is the relative synchrotron frequency spread, and τ is the bunch length.

From Eq. (1.93), the scaling of the threshold of loss of Landau damping can be expressed [25] in terms of longitudinal emittance, bunch intensity, energy, and rf parameters as

$$(\mathrm{Im}Z/n)_{\mathrm{th}} \propto \frac{\varepsilon^{5/2}\,h^{7/4}}{N_b\,V_{\mathrm{rf}}^{1/4}\,E^{5/4}}. \tag{1.94}$$

Given the dependence of the stability threshold on the longitudinal emittance, a cure for loss of Landau damping can be achieved by increasing the emittance during the acceleration ramp (e.g., [26]). This can be done with a controlled longitudinal emittance blowup, for instance by injecting rf phase noise [13, 14] or phase modulation in an additional rf system [27].

1.3 Electron cloud

Another effect that may appear in accelerators of positively charged particles for high beam currents is the electron cloud (e-cloud) [28, 29]. The e-cloud is a process in which free electrons inside the vacuum chambers are accelerated by the electric field induced by a positively charged particle beam, hit the vacuum chamber wall and produce secondary electrons in a quantity that depends on the Secondary Electron Yield (SEY) of the vacuum chamber surface. For high values of the SEY, the e-cloud density can increase after each bunch passage in a sort of an avalanche effect that is usually referred to as e-cloud buildup. High e-cloud densities can produce harmful effects to the beam, such as transverse emittance growth leading to particle losses, transverse instabilities, heat load in the cryogenic system, etc. This effect has been observed and intensively studied in numerous particle accelerators around the world, for example in the Photon factory and in KEKB at KEK, in the BEPC at IHEP, in proton storages rings in Los Alamos and at BINP, or in the ISR and SPS at CERN (e.g., [30]).

The e-cloud effect depends on the beam parameters, because the number of electrons that are produced on each bunch passage is determined by the bunch intensity, length, and the transverse beam size. The bunch spacing is critical, since the e-cloud decays between the passage of two consecutive bunches. For large bunch spacing, the e-cloud can completely decay between two bunch passages, while for short bunch spacing the buildup can occur more rapidly.

In order to reduce the e-cloud effects, efforts are put in minimizing the SEY of the surface of the vacuum chambers. In the design phase of the accelerator, if e-cloud is found to be a potential limitation, a low-SEY coating of the vacuum chamber can be considered. For example, a TiZrV non-evaporable getter (NEG) coating [31] has been used in the LHC warm vacuum chambers [1]. Coating the vacuum chambers of accelerators that are in operation have also been suggested [32, 33, 34], and it is being discussed as a fallback solution for the HL-LHC case [4]. Another option to lower the SEY of the vacuum chambers which has been proven effective is scrubbing with beams [29]. The electrons impinging the surface of the vacuum chamber can reduce its SEY if the number of electrons (dose) is large enough. That requires a high e-cloud density, which is achieved by injecting bunch trains with the shortest bunch spacing and highest intensity possible. Obviously, as the e-cloud density is high, operation is only possible using stabilizing mechanisms, as for example high chromaticity values or an active transverse damper system.

In Chapter 5, a novel e-cloud density measurement method is presented. The interaction of the beam with the e-cloud results in an energy transfer from the beam to the e-cloud, which translates to a beam energy loss. Similarly to the phase shift caused by the resistive losses from the impedance, described in Section 1.2.1, this energy loss is compensated by the rf system through a phase shift. The bunch energy loss due to e-cloud has been calculated analytically [35] and in macroparticle simulations [36], and it was found to be dependent on the e-cloud density.

1.4 Macroparticle tracking simulations

Simulations codes are a useful tool for studies of intensity effects and instabilities in synchrotrons, especially when the machine impedance is too complicated to be studied analytically. These codes are also practical for analysis of the effect on the beam of the low-level rf loops (phase loop, synchro loop, and radial loop, described in Chapter 2), the controlled longitudinal emittance blowup by rf-noise injection, or to simulate the behavior of some instrumentation devices.

The most common approach for the simulation code when studying single-bunch instabilities is to use a macroparticle tracker. In these codes, a reduced number of particles are tracked to minimize the computational power needed, as the bunch in most of the real cases consists of a large number of particles (the LHC nominal bunch intensity is 1.15×10^{11}). Each simulated particle is called a macroparticle and accounts for a number of real particles, assuming that they follow approximately the same trajectories. For that reason, these simulation codes usually require a convergence analysis to find the optimum number of macroparticles required for accurate results.

The computational power required by macroparticle tracking codes scales, in general, with the number of bunches. Simulations of multi-bunch cases can therefore demand a computational power exceeding the capabilities of desktop computers, requiring in some cases the use of supercomputers. Nowadays, with the increasing computational power and optimization of the algorithms, it is becoming possible to simulate cases with a reduced number of bunches in normal desktop computers. However, at the moment of writing this thesis, it is still very challenging to simulate the LHC case, since the nominal number of bunches is 2880 (with 25 ns spacing) [1].

1.4.1 The Beam Longitudinal Dynamics simulation code (BLonD)

In Chapters 3 and 4, beam stability studies using macroparticle simulation will be presented. All simulations were performed using the macroparticle tracking code BLonD [37], recently developed in the BE/RF group at CERN. This code is based on a discretization of the equations of motion using the pair (Δt, ΔE) as phase-space coordinates, defined as the time and energy difference with respect to the design reference values. The tracking is performed in time steps of one revolution period, and at each step n the phase-space coordinates are updated according to the discretized equations of motion:

$$\Delta E[n+1] = \Delta E[n] + \sum_{k=1}^{N_{\mathrm{rf}}} q\, V_{\mathrm{rf},k} \sin\varphi_{\mathrm{rf},k}\,(\Delta t[n]) - (E_o[n+1] - E_o[n])\,, \tag{1.95}$$

$$\Delta t[n+1] = \Delta t[n] + \frac{\eta_o[n+1]\, T_o[n+1]}{\beta_s^2[n+1]\, E_o[n+1]}\,\Delta E[n+1], \tag{1.96}$$

where N_{rf} is the number of rf systems, $V_{\mathrm{rf},k}$ is the voltage of the k-th rf system, η_o is the zeroth order slippage factor, and $\varphi_{\mathrm{rf},k}$ is the rf phase angle defined by

$$\varphi_{\mathrm{rf},k}\,(\Delta t[n]) = \sum_{k=1}^{N_{\mathrm{rf}}} \frac{\omega_{\mathrm{rf},k}[i] - h_k[n]\omega_o[n]}{h_k[n]\omega_o[n]}\, 2\pi\, h_k + \omega_{\mathrm{rf},k}[n]\,\Delta t[n] + \phi_{\mathrm{offset},k}[n], \tag{1.97}$$

with $\omega_{\mathrm{rf},k}$ being the angular frequency of the k-th rf system, h_k its harmonic number, and $\phi_{\mathrm{offset},k}$ its phase offset.

The choice of these phase-space coordinates has several advantages, for example, it simplifies the implementation of low-level rf loops and the interaction of the beam with the machine impedance, including long-range impedances (e.g., high-Q resonators) which can couple bunches over many turns.

The code allows to treat collective effects either in the time domain, using a wakefield or a constant pure imaginary Z/n, or in the frequency domain, by inputting an impedance model. In either case, wakefields and impedances can be defined using a resonator model. It is also possible to model some elements in the time domain and others in the frequency domain within the same simulation.

Acceleration and all kinds other rf manipulations can also be simulated, with a single or multiple rf systems. A general implementation of low-level rf loops is available, including the phase loop, synchro loop, and radial loop, with parameters that can be adapted to the peculiarities of any machine.

Several options are implemented for the generation of the bunch distribution, with the possibility to initialize a bunch matched to the rf bucket starting from a distribution function or a line density, which can be chosen from the several options (Gaussian, binomial, parabolic, etc.) or inputted by the user.

The code is written in Python, with the most computation-demanding parts written in C++ and optimized for faster running time. It has been developed in a modular fashion, which allows the users to use only the modules they need and to easily implement new features depending on the requirements.

The reliability of the code has been verified by comparing with beam measurements in several machines and with benchmarks against results from other simulation codes. Apart from the comparison between LHC measurements and simulations shown in Chapter 3, simulations using BLonD have been compared with measurements in other CERN accelerators, as the SPS, the PS, and the PSB [38]. In addition, the code has been successfully benchmarked against other simulation codes as ESME [39], Headtail [40], and PyOrbit [41].

2 The LHC main parameters, rf system, and beam diagnostics

This chapter gives an overview of the beam and machine parameters of the LHC. Then, the main features of the LHC rf system are reviewed, with special attention to the low-level rf loops. Finally, the beam diagnostic tools used for the measurements that are presented in this thesis are also described here.

2.1 The LHC parameters

The relevant beam and machine parameters for nominal operation as defined in the LHC Design Report [1] are summarized in Table 2.1.

Table 2.1 – Summary of nominal beam and machine parameters [1].

		Injection	Collision
Beam parameters			
Proton energy	[GeV]	450	7000
Relativistic gamma γ		479.6	7461
Intensity per bunch N_b	[10^{11}]	1.15	
Number of bunches M		2808	
Bunch spacing	[ns]	25	
Bunch length (4σ)	[ns]	1.7	1.0
Longitudinal emittance (2σ)	[eVs]	1.0	2.5
Transverse normalized emittance	[μm rad]	3.5	3.75
Circulating beam current	[A]	0.582	
Machine parameters			
Ring circumference	[m]	26658.883	
Field of main bends	[T]	0.535	8.33
Bending radius	[m]	2803.95	
Momentum compaction α	10^{-4}	3.225	
Slip factor η	10^{-4}	3.182	3.225
Gamma transition γ_{tr}		55.76	

During operation in the run 1 and in the current run 2, some of the beam and machine parameters were different. The most significant change was the maximum beam energy, which was 3.5 TeV in 2010 and 2011, then increased to 4 TeV in 2012, and further increased to 6.5 TeV in the run 2 until the moment of writing this thesis (2016).

The bunch spacing was increased to 50 ns in the run 1 to cope with the strong e-cloud effect, but 25 ns were recovered in 2015 after a few periods of scrubbing with beams [42]. The larger bunch spacing used in the run 1 limited also the maximum number of bunches that could be injected to 1380. In order to compensate for the lower luminosity due to the reduced number of bunches in the run 1, the intensity per bunch was pushed up to about 1.7×10^{11} at injection. In the run 2, the nominal bunch intensity 1.15×10^{11} was used and a maximum of 2244 bunches were successfully brought into collisions by the end of 2015. However, new requirements on the filling pattern have reduced the number of bunches that can be injected into the LHC to a maximum of 2748.

The average bunch length was about 1.1–1.2 ns at injection due to the smaller longitudinal emittance injected from the SPS, as well as an rf voltage at injection different from the nominal one (discussed in the following section). At top energy, on the other hand, it had to be increased to 1.25–1.35 ns in comparison to the nominal flat-top values from Table 2.1 for different reasons: in the run 1 it was done to deal with the high beam-induced heating [43] and in 2015 to reduce the heat load in the cryogenic system due to e-cloud and to minimize the required rf power in the klystrons.

The transverse emittance was also smaller in the run 1, achieving 1.5 μm rad injected and 2.4 μm rad at collisions. Table 2.2 shows a summary of the beam parameters used in the LHC during the run 1 and the run 2 that are relevant for this thesis.

Table 2.2 – Summary of parameters for different beams injected into the LHC during the run 1 and the run 2.

Beam type	150 ns	75 ns	50 ns	25 ns
Bunch spacing [ns]	150	75	50	25
Number of bunches per train	8/12	8/24	12/24/36	24/48/72
Maximum number of bunches	368	936	1374	2748
Bunch intensity [10^{11}]	1.1–1.2	1.1–1.2	1.1–1.7	1.1–1.2
Bunch length (4σ) [ns]	1.2–1.6	1.2–1.6	1.2–1.6	1.2–1.6
Normalized transverse emittance [mm·mrad]	2.0-3.5	2.0-3.5	1.5-3.5	1.5-3.5

2.2 The LHC rf system

The LHC rf system is composed by 2 cryogenic modules per ring, each of them containing 4 superconducting rf cavities which operate at 400.8 MHz. Each cavity can provide a voltage of up to 2 MV, giving a maximum rf voltage available in the LHC of 16 MV. Figure 2.1 shows the

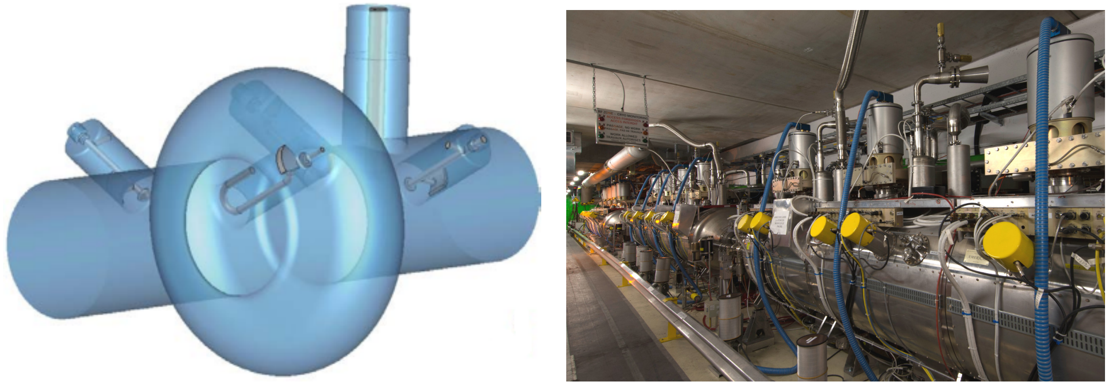

(a) Model of a single LHC rf cavity

(b) Cryogenic modules installed in Point 4

Figure 2.1 – Model of a LHC single rf cavity (left) and cryogenic modules containing the rf cavities installed in the LHC tunnel at the Interaction Point 4 (right).

model of a single rf cavity and the cryogenic modules installed at the Interaction Point 4 (IP4), a straight section of the LHC.

The rf cavities are driven by klystrons, one per cavity, each of them designed to deliver a power of up to 300 kW. The klystrons are also installed underground in IP4, in the cavern known as UX45, relatively close to the rf cavities.

The power coupler is variable and can change the loaded Q between 20 000, used for injection, and 60 000, used for acceleration and collisions. The lower loaded Q provides higher bandwidth to deal with transients at injection, while the higher loaded Q reduces the required power during the coast [44].

The main rf parameters are listed in Table 2.3. As mentioned above, these parameters were also modified in operation in the run 1 and the run 2. Most of the time the rf voltage at injection was 6 MV and the voltage at flat top was 12 MV, except during the last half of 2015 when 10 MV were used due to power limitations with high-intensity beams [45].

Table 2.3 – Summary of the nominal rf parameters [1].

		Injection	Collision
Revolution frequency f_{rev}	[kHz]	11.245	
rf frequency f_{rf}	[MHz]	400.8	
Harmonic number h		35640	
Total rf voltage V_{rf}	[MV]	8	16
Synchrotron frequency f_{so}	[Hz]	61.8	21.4
Bucket area A_B	[eVs]	1.46	8.7
Bucket half height $\Delta E/E$	[10^{-3}]	1	0.36

One more rf system at 200 MHz was foreseen [1] for capture the beams extracted from the SPS, but it was finally not installed. An impedance reduction campaign in the SPS [46] allowed to accelerate and extract LHC beams [47] with smaller longitudinal emittance and a bunch length of about 1.6 ns, which could be injected in the LHC with few particle losses.

2.2.1 Low-level rf loops

The low-level rf system comprises all the electronics and controls used to keep the rf parameters (voltage amplitude, frequency, and phase) according to the programmed values, and to minimize the effect of rf noise and transients on the beam.

Feedback loops around each cavity ensure a precise control of the amplitude and phase of the voltage seen by the beam. In general, the feedback system has to counteract the induced voltage due to the cavity impedance, which is called beam loading. For this purpose, the feedback reduces the effective cavity impedance. The electronics are installed underground in a Faraday Cage located in UX45. The functioning of the feedback system is not described here, but more details can be found in Ref. [48].

The classical implementation of the beam control system includes a phase loop to adjust the rf phase to match the beam phase and either a radial or a synchronization (synchro) loop, as they are exclusive. The radial loop controls the radial position of the beam acting on the rf frequency and the synchro loop keeps the rf frequency as programmed. The effect of both loops can be in contradiction and the control of the rf frequency would be degraded. All the loops of the beam control act on the frequency of the voltage-controlled crystal oscillator (VCXO), which generates the rf signal that is sent to the klystrons. In the LHC, the combination of a phase loop and a synchro loop is used. The modules related to beam control are installed in a surface building, called SR4. The implementation of the loops is described in more detail below.

Finally, the low-level rf system has to manage the beam transfer from the SPS to the LHC, requiring the synchronization of both machines for the bunch-to-bucket injection [49, 50].

A Longitudinal Damper was also proposed in the LHC Design Report [1], but not yet fully developed. The purpose of this system is to damp injection oscillations and coupled-bunch oscillations but, due to the limited bandwidth of the rf cavities, it could only damp low-order modes excited by the main cavity impedance. The system could also help reducing losses and emittance blowup at injection, but so far it was not really needed.

Phase loop

The phase loop adjusts the frequency of the VCXO to minimize the phase error signal, computed as the phase difference between the beam (400 MHz component) and the rf voltage. Thereby the phase noise is reduced and the beam can be stabilized against dipole oscillations and transients, leading to an increase in the beam lifetime. The gain of the loop must be high enough so that the rf frequency can be changed faster than a synchrotron period, otherwise filamentation would take over.

In the LHC, the phase error is calculated every turn for each bunch and then averaged over all bunches. This means that, in the multi-bunch case, the phase loop can only damp oscillations of the common mode (mode 0). The phase error signal can be used for diagnostics as a measurement of the bunch phase. More details on how the bunch and cavity phases are measured are given in the next section.

Synchro loop

The synchro loop compares either the phase of rf voltage or the beam phase with the phase of a precise frequency reference signal. In the LHC, the rf phase is used and a Direct Digital Synthesizer (DDS) generates the reference signal following the rf frequency program, which is calculated in turn from the magnetic field and radial steering programs. The loop then acts back on the frequency of the VCXO, so that the frequency sent to the klystrons is adjusted to the programmed one.

The time constant of the synchro loop should be longer than the synchrotron period (adiabatic), so that the longitudinal emittance is not increased. This requires that the dynamics of the synchro loop are modified according to the changes of the synchrotron frequency, which has to be calculated as described in Section 1.1.7.

Radial loop

Until now, the choice taken for operation of the LHC has been to use the synchro loop. Nevertheless, a transverse pickup is available in IP4 for radial position measurements and could eventually be used by a radial loop. In that case, the radial position would be compared to the radial steering program and the rf frequency would be modified in consequence. The time constant of this loop should also be longer than the synchrotron period, for the same reason as for the synchro loop case.

2.3 Longitudinal beam diagnostics of the LHC

The LHC relies on numerous diagnostic tools that are required for commissioning, operation, and studies. Here we describe the main devices used in order to perform the measurements presented in this thesis, which are the measurements of the longitudinal beam profile, the peak-detected Schottky spectrum, and the bunch phase. These diagnostic tools have been designed, installed, and commissioned in collaboration with colleagues from the BE-RF-BR, BE-RF-FB, BE-RF-CS, and BE-BI-QP sections at CERN[1]. In addition, a system called Beam

---

[1] Special thanks to Thomas Bohl (BE-RF-BR), Philippe Baudrenghien, Javier Galindo Guarch, Daniel Valuch, Urs Wherle (BE-RF-FB), Miguel Ojeda Sandonis (BE-RF-CS), and Tom Levens (BE-BI-QP) for their support in developing and setting up the beam diagnostics used in this thesis.

Quality Monitor (BQM) [51] automatically provides a series of bunch-by-bunch measurements, from which the bunch length values are widely used in this thesis.

2.3.1 Longitudinal bunch profile

Longitudinal bunch profile measurements in the LHC are carried out by using a fast oscilloscope connected to a longitudinal pickup.

The pickup is a wideband Wall Current Monitor (WCM) [52] of the coaxial type (bandwidth of ~ 3 GHz), named APWL [53]. This pickup has 8 outputs that can be used independently, provided that the other outputs are correctly loaded. In order for the measured signal to be independent of the transverse beam size or any transverse displacement of the beam, 4 diagonally opposed outputs can be combined (or even all of them) [54]. Given the versatility of this pickup, it is used for all the beam diagnostics described in this chapter.

Two LeCroy Wave Runner 104MXi oscilloscopes are connected to 4-combined outputs of two pickups (one per ring). The 1 GHz bandwidth of these scopes is not sufficient for high-accuracy measurements, but their signals are displayed in the CERN Control Center (CCC) for real-time bunch profile monitoring.

Another two scopes (one per ring) were installed in SR4 for more precise observations. These are faster scopes, Tektronix DPO7254, with a sampling rate of 40 GS/s and 2.5 GHz bandwidth. However, the long cables connecting the scope to the pickup introduce a distortion in the signal that can be seen, for example, in Fig. 2.2 as a long tail on the right-hand side of the bunch profile. For that reason, during a technical stop in the summer of 2012 another scope of the same model was installed underground in the Faraday Cage in UX45, connected to pickups on both rings. The shorter cables used helped to reduce the signal distortion.

Finally the scope installed in the Faraday Cage was moved during the Long Shutdown 1 to a gallery (UA43) that is parallel to the LHC tunnel, where LEP klystrons were located in the past. One of the scopes from SR4 was also moved there and each of them was connected to a different ring. In order to minimize the potential distortion that can be introduced by a combiner, it was decided to connect the scope to a single feedthrough.

The transfer function from the pickup to the scope was measured for the latest setup and it is shown in Fig. 2.3. It can be used to further improve the quality of the beam profiles. Figure 2.2 shows the difference between a measurement done in SR4 with the initial system in 2011 and another one done in 2015 with the scope in UA43 (also with corrections for the transfer function).

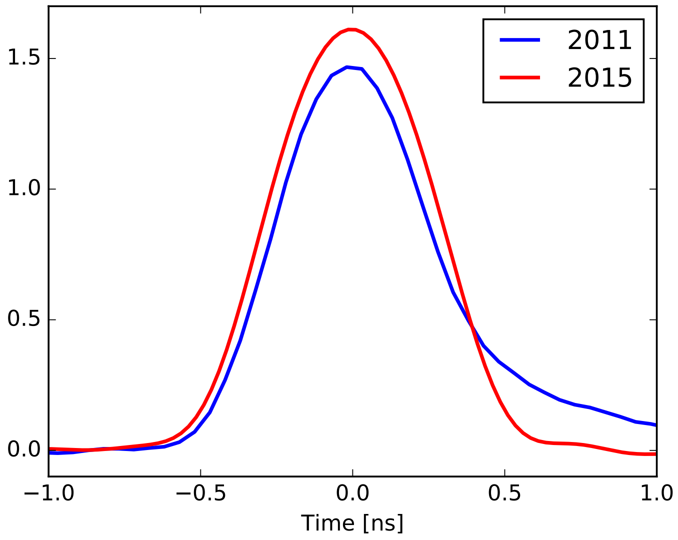

Figure 2.2 – Comparison of a bunch profile measured from SR4 in 2011 (blue trace) and another one measured in 2015 using the scope installed in UA43 (red trace), the latter with corrections for the transfer function of the signal chain. Note that the long tail on the right-hand side of the profile measured in 2011 is almost completely removed in the profile acquired using the upgraded system in 2015.

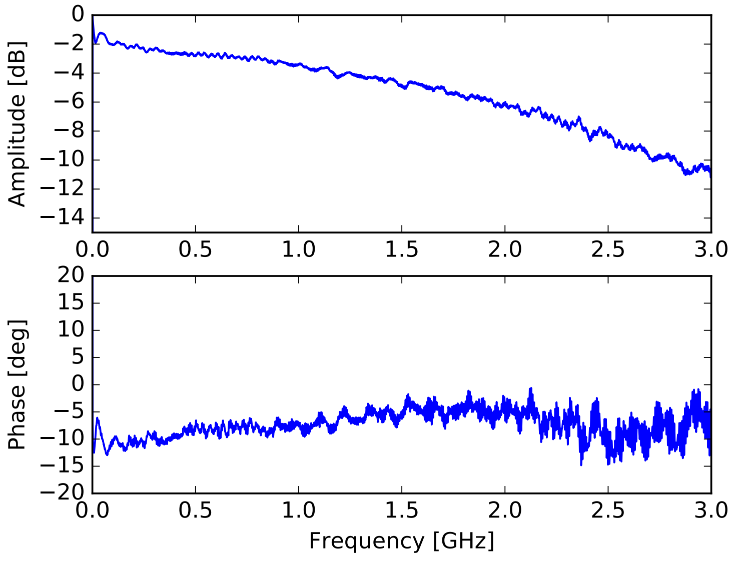

Figure 2.3 – Amplitude (top) and phase (bottom) of the transfer function from the pickup to the scope, for the upgraded system installed in UA43 and used in 2015. A linear fit was done to the phase data to subtract the linear component due to the signal delay in the cables.

2.3.2 Peak-detected Schottky spectrum

The peak-detected Schottky spectrum is a diagnostic tool that can be used to obtain the particle distribution in synchrotron frequencies (for stationary conditions) or to observe coherent bunch oscillations (e.g., [55, 56]).

There are three different types of peak-detectors in the LHC, all of them based on the classical peak detector using a fast diode, shown schematically in Fig. 2.4. All peak detectors are connected to APWL pickups. The values of the capacitor and resistors define the dynamics of the detector, and should be selected according to the machine revolution frequency and the range of bunch length. For a detailed explanation of the measurement principle, see Ref. [56].

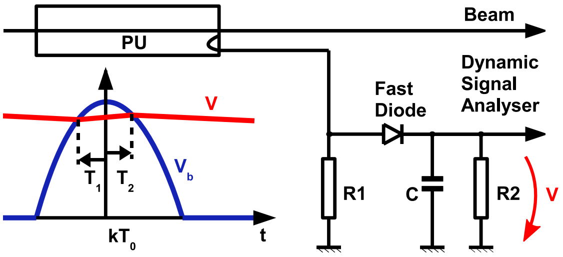

Figure 2.4 – Simplified schematic of a peak detector used in the LHC [56].

The first type is a wideband peak detector (SPS 10237L), which is optimized to sample the peak over a full turn. The electronics is integrated into a NIM [57] module, and there is one module per ring. The output of the module is the peak signal, which must be connected to a spectrum analyzer in order to obtain the peak-detected Schottky spectrum.

Another type is the gated peak detector (EDA-01937), which incorporates a fast gate that allows to select a single bunch for observation even if the machine is filled with more bunches. Also integrated into a NIM module, there are three of them available and can be used as required. Similar to the other module, the output is the peak signal. For spectrum measurements, a HP 3562A spectrum analyzer is usually used. This spectrum analyzer has two channels, so measurements are normally limited to either two bunches of one ring or one bunch per ring.

An optimized version of the gated peak detector has been developed [58] and a prototype has been built using a custom VME-crate based module [59]. The module implements 4 peak detectors that can be used in parallel, each of them equipped with an Analog-to-Digital Converter (ADC) for data acquisition. The VME module has a lower signal-to-noise ratio (SNR) compared to the NIM module. Four modules are currently in production and will be installed in the LHC in 2016.

The prototype was tested in the LHC in 2013 during the proton-ion run and then used during MDs in 2015. A comparison between measurements taken with the gated NIM and the VME modules is shown in Fig. 2.5. Although it was mentioned before that the SNR of the VME module is lower, in this example it is dominated by the noise in the ADC, which will be reduced in the final version by using a 24-bit ADC instead of the 16-bit ADC used in the prototype.

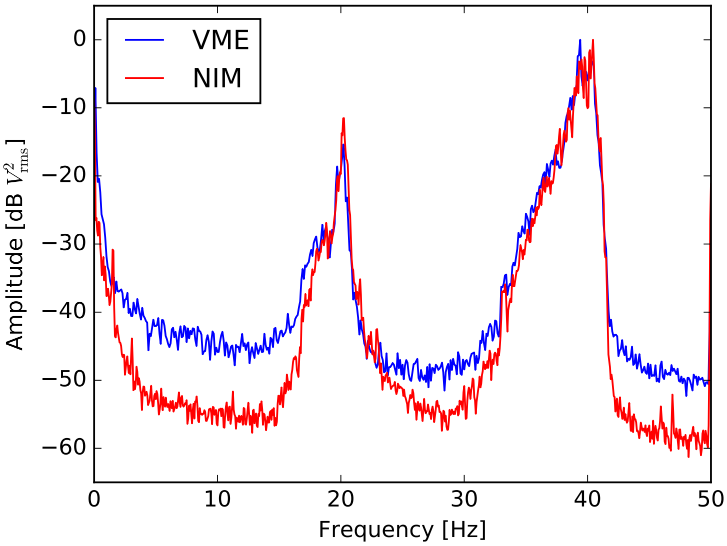

Figure 2.5 – Example of two peak-detected Schottky spectra showing the dipole and quadrupole bands (LHC at 6.5 TeV, $V_{\text{rf}} = 12$ MV, $f_{so} = 20.6$ Hz), taken at the same time using the VME (blue) and the gated NIM (red) modules.

2.3.3 Bunch phase

In the LHC, two beam phase modules (PM) [60] per beam (4 in total) are installed for bunch phase measurements. This signal can be used for resistive impedance measurements (described in Chapter 1, results presented in Chapter 3), or for e-cloud monitoring (see Chapter 5). One of the modules is used by the phase loop and the other one, installed during the Long Shutdown 1 and commissioned in 2015, is exclusively used for observations.

The PM determines the bunch phase as the difference between the beam pick-up phase and the rf voltage phase, as shown in the simplified scheme in Fig. 2.6. The beam pick-up is a wideband pickup of the APWL type that measures longitudinal bunch profiles. This signal is fed into a strip-line comb filter transforming a single pulse (a bunch profile) into a wavelet at 400.8 MHz lasting for 9 rf periods. The filter output is the beam signal input to the PM. The second rf input is the vector sum of the eight cavity-antenna signals. Appropriate delays are added to the cavity signals to compensate for the time of flight between the cavities. Two analog in-phase/quadrature (I/Q) demodulators transform the beam signal and cavity sum into (I,Q) pairs and an FPGA computes the phase and amplitude of both signals (see App. A). The effect of beam loading is excluded by measuring the real voltage in the cavities (for details see App. B).

The PM is capable of measuring every turn the bunch amplitude and phase, as well as the cavity voltage amplitude and phase for buckets spaced by 25 ns over the whole ring. The PM used by the phase loop has a limited memory that allows to measure bunch-by-bunch data in burst of 73 acquisitions at an adjustable rate, which is usually set to 5 revolution periods (0.45 ms). A typical burst therefore covers 33 ms, almost 2 synchrotron periods T_s at 450 GeV

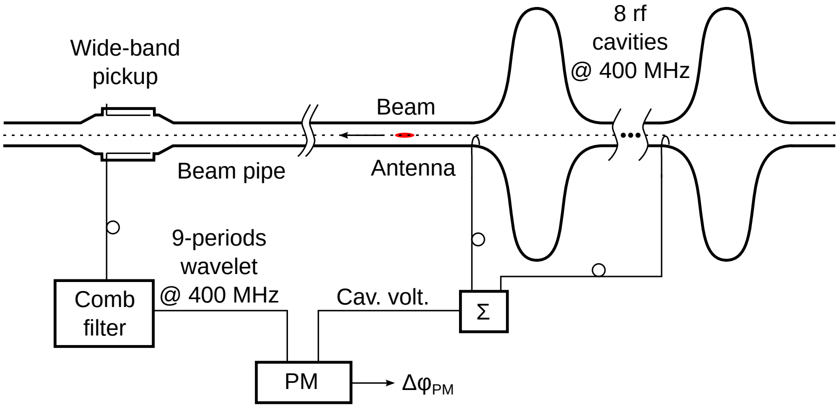

Figure 2.6 – Simplified scheme of the bunch phase measurement in the LHC. A wavelet is generated from the wideband pickup signal and its phase is compared in the beam phase module with the phase of the vector sum of the voltages of the eight rf cavities.

($T_s = 18$ ms for $V = 6$ MV). The other PM transfers the bunch-by-bunch, turn-by-turn IQ data through a fiber optic link to a high-performance server known as ObsBox [61]. An example of the bunch-by-bunch phase measurement is shown in Fig. 2.7, where the phase shift along the bunch train is caused by e-cloud effect.

The PM was designed for a phase accuracy of about 1 deg. However, for measurements of the impedance and e-cloud effect a higher accuracy is required, of the order of 0.01 deg for the former and 0.1 deg for the latter. To achieve these requirements, the sources of systematic errors were identified and corrections were implemented, as described below.

Measurement Corrections

After a bunch passage, reflections due to impedance mismatch in the signal transmission path affect subsequent bunch phase measurements. For high-accuracy results, it is necessary to remove these perturbations. The impulse response of the system from the pickup to the PMs (see Fig. 2.8) was measured with a single bunch and is used for correction of the multi-bunch data.

These reflections were identified during the run 1, and therefore they were taken into account when the observation system was installed during the Long Shutdown 1. Time-domain reflectometry measurements were done to identify possible sources of reflections and the signal routing was optimized, improving the impedance match at the pickup output. Shorter cables were used, with the aim of reducing the reflections and minimizing the signal distortion. The result is a clear reduction of the strongest reflection, visible in Fig. 2.8 (red trace).

Another correction applied to the raw data helps to minimize a systematic error which is introduced by the residual offsets of the I and Q components (I_o and Q_o, respectively) of the bunch signal (see also App. A for more details). The diagram in Fig. 2.9 shows that the error $\delta\varphi$

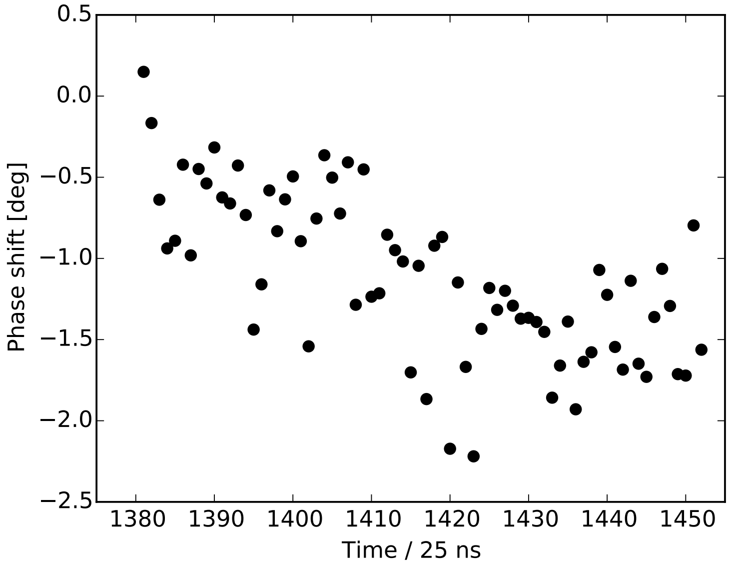

Figure 2.7 – Example of raw data for the phase shift along a bunch train of 72 bunches averaged over 73 acquisitions spaced by 5 turns. The phase shift along the bunch train is due to e-cloud effect. Measurements were taken on Beam 1 at injection energy at the beginning of the 2012 scrubbing run with 25 ns spaced bunches (Fill 3389, 6-12-2012). Average bunch intensity $\overline{N} \sim 1.1 \times 10^{11}$.

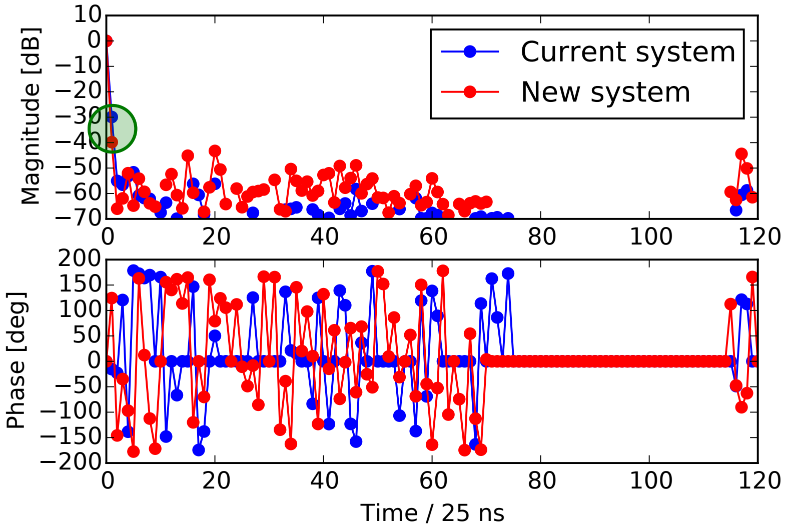

Figure 2.8 – Impulse response from the pickup to the phase module of the system used by the phase loop (blue) and of the observation system (red), measured with a single bunch during 3 μs. Note that the strongest reflection affects the following bunch (bucket position 1 in these plots, green circle) and in the observation system it is reduced by ~10 dB. Reflections below -70 dB are neglected.

in the phase measurement depends on the offsets and on the amplitude A and phase φ_{PM} of the bunch signal as

$$\delta\varphi = -\tan^{-1}\left[\frac{A_o \sin\left(\theta'_o\right)}{A - A_o \cos\left(\theta'_o\right)}\right], \tag{2.1}$$

where $\theta'_o = \varphi_{PM} - \theta_o$, $\theta_o = \tan^{-1}\left(Q_o/I_o\right)$, and $A_o = \sqrt{I_o^2 + Q_o^2}$.

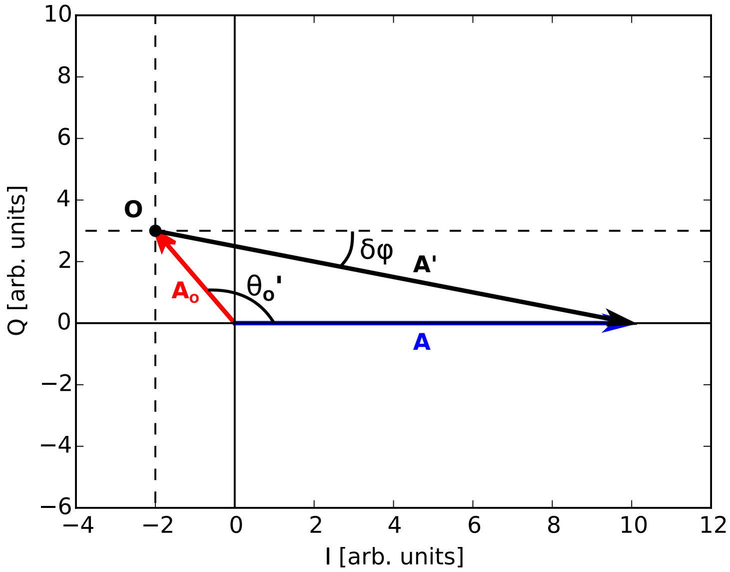

Figure 2.9 – Vector representation of the error introduced by the residual offsets of the I and Q components of the bunch signal for the case $\varphi_{PM} = 0$. The original vector $\mathbf{A}'$ (black) is defined from the real origin **O** to the end of the measured vector **A** (blue). The phase error $\delta\varphi$ is the angle between $\mathbf{A}'$ and **A**, and it depends on $|\mathbf{A}|$, $|\mathbf{A_o}|$ and θ'_o as defined in Eq. (2.1).

The values of I_o and Q_o are estimated in the IQ plane, averaging the noise measured in the empty buckets (assuming white noise). The standard deviation of this noise can be used to estimate the remaining error of the bunch phase measurements. For a bunch intensity of 1.1×10^{11}, the noise amplitude after corrections is typically ~1/700 of the bunch amplitude signal. In the worst case, which can happen when the angle between the noise and the bunch signals is 90 deg, it would lead to a phase error of ±0.08 deg.

The measured bunch phase after the corrections described above is shown in Fig. 2.10 (blue squares).

Data Post-Processing

The data post-processing significantly improves the measurement precision and consists of two steps that are applied to each bunch separately.

The first step should be performed differently depending on the system used for the phase

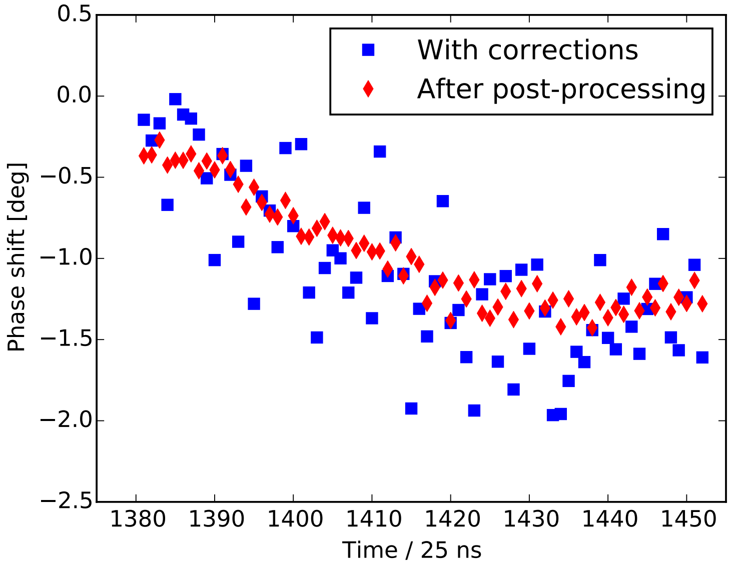

Figure 2.10 – Phase shift along the bunch train after corrections for systematic errors (blue squares) and after post-processing (red diamonds), applied to the measurements shown in Fig. 2.7. The phase shift along the bunch train due to e-cloud effect is smoother.

measurements. For the system used by the phase loop, the variation of the bunch phase in the 73 acquisitions is checked for each burst. If it is smaller than 1 deg, we assume that the bunch is not oscillating and the value of the bunch phase can be calculated as the average of the 73 acquisitions. In this case, the maximum error would be in the range $\pm 0.5\ \mathrm{deg}/\sqrt{73} = \pm 0.06$ deg. If the phase variation of a bunch is larger than 1 deg, the bunch phase is extracted from a sine-wave fit of the dipole synchrotron oscillations to minimize the measurement error, as shown in Fig. 2.11. For the observation system, as there is no memory limit, a larger number of turns can be acquired, increasing the precision and making the sine-wave fit optional. For e-cloud measurements, usually a burst of 2000 turns is acquired and averaged, which gives an error that is $\sqrt{2000} \approx 45$ times smaller than the amplitude of the oscillations or measurement noise.

Then, since the bunch phase is changing slowly during the time between bursts, the bunch phase is smoothed by applying a local linear regression with a moving window of 10 bursts. As shown in Fig. 2.10 (red diamonds), after the post-processing the resulting phase shift is smoother.

2.3.4 The LHC Beam Quality Monitor

The LHC Beam Quality Monitor (BQM) [51] is a system that uses longitudinal bunch profiles measured by a wall-current monitor (same type as described above, APWL) to determine several longitudinal beam parameters during the LHC cycle. The BQM checks the filling pattern and extracts the length, center position, and peak amplitude of each bunch, from

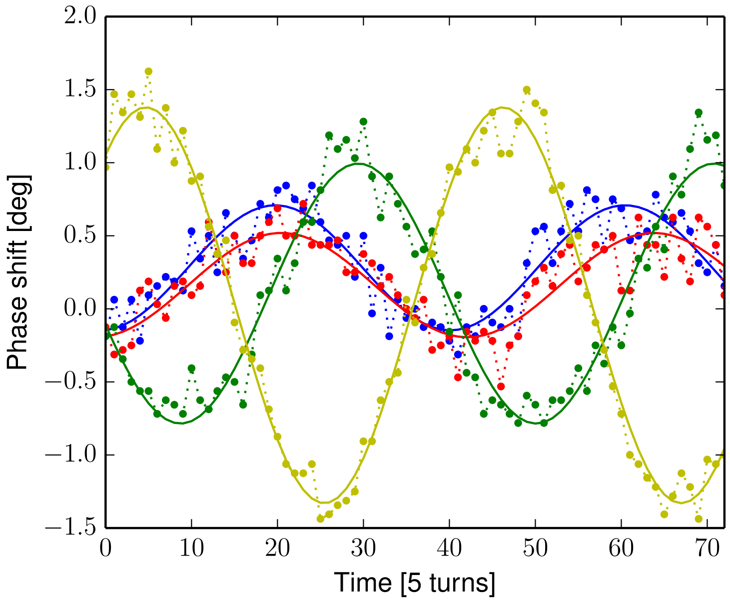

Figure 2.11 – Example of the sine-wave fit (solid lines) of the synchrotron oscillations measured for four different bunches (dots), as used in the data post-processing.

bunch profiles. All the measurements are stored in the logging database [62].

The bunch length is calculated from the FWHM of the profile, scaled as the 4σ length equivalent for a Gaussian bunch (as defined in Section 1.1.6). The BQM also corrects the bunch length for the distortion caused by the transfer function of the signal chain, providing a good measurement accuracy. The bunch center position is calculated as the average of the two points used for the calculation of the FWHM.

The bunch phase can also be computed by applying a linear fit to the bunch positions, assuming that the distance between the buckets is constant (~2.5 ns). Figure 2.12 shows an example of bunch phase measurements using bunch positions. Although the sampling rate of the acquisition card used by the BQM is relatively low (8 GS/s), the precision of the measurements is improved by the interpolation which is applied in the algorithm that calculates the bunch position. Averaging over a few measurements also gives much cleaner results. However, the phase shift due to transient beam loading is also included in these phase measurements and it is larger than the phase shift due to other effects of interest (impedance, e-cloud). This can be seen in Fig. 2.12 when comparing the BQM measurements with measurements taken by the phase module at the same time. The estimation of the phase shift due to the beam loading effect with the required accuracy is very complicated, and therefore bunch positions are not usable in practice.

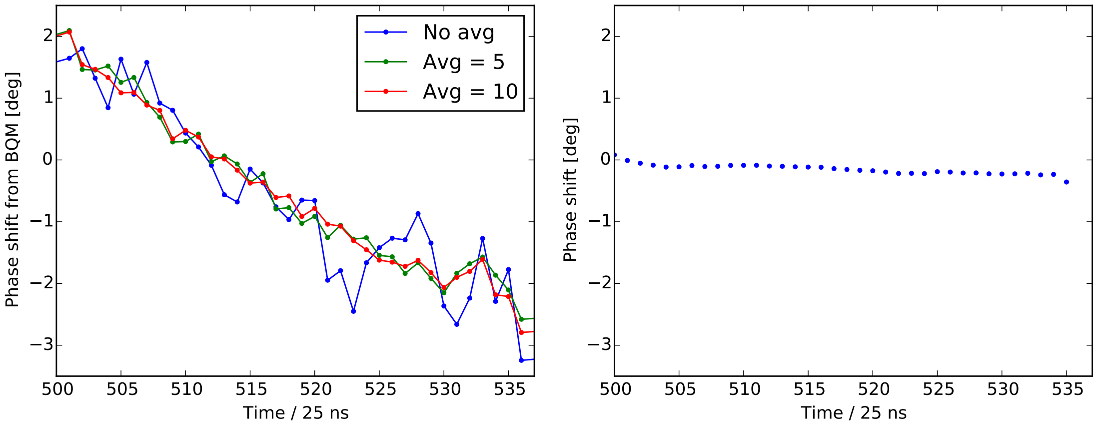

(a) From BQM (b) From phase module

Figure 2.12 – Bunch-by-bunch phase shift computed from bunch positions measured by the BQM (left) and by the phase module of the phase loop (right). The larger phase shifts in panel (a) are due to beam loading with the one-turn feedback off. Beam 2. Fill 2248 (25 ns, 24-10-2011).

3 Beam-based measurements of the LHC longitudinal impedance

This chapter is devoted to the validation of the LHC longitudinal impedance model with beam measurements. First, the main contributors to the longitudinal impedance will be detailed. Then measurements of the resistive and reactive part of the impedance with stable beam will be presented. Finally, loss of Landau damping observed at injection, during the ramp, and at flat top will be compared with results from macroparticle simulations.

3.1 The LHC impedance model

In the design phase of the LHC, the intensity effects were taken into consideration in order to verify that the LHC could be properly operated. For that purpose, the impedance was estimated [63] using the information available at the time, which did not include the design of some of the accelerator components. Following the updates of the design of the elements, the impedance model was re-evaluated several times, until it was finally included in the LHC Design report [1].

The impedance model was then later refined with more accurate calculations and measurements of the accelerator components when they were built [64], and it is still nowadays in constant evolution. Measurements with beams are an important step for the validation of the impedance model.

In the following, beam measurements are presented and benchmarked against the latest available version of the LHC longitudinal impedance model [65], which is shown in Fig. 3.1. This model includes the contributions from the beam screens in the cold magnets, the vacuum chamber in the warm sections, and a broadband resonator model that takes into account the pumping slots of the beam screens, the experimental chambers, the rf cavities, the Y-chambers, beam instrumentation devices, and the collimators. The narrowband impedances of the high-order modes of the rf cavities and experimental chambers are also incorporated into the model.

Thanks to the careful design of all the components, the longitudinal impedance of the LHC is relatively low. For example, the imaginary part of the low-frequency effective impedance ImZ/n is 0.09 Ω, to be compared to 5 Ω in the CERN SPS or 20 Ω in the CERN PS. This low impedance poses a challenge, as most of the traditional methods to measure the impedance are not directly applicable.

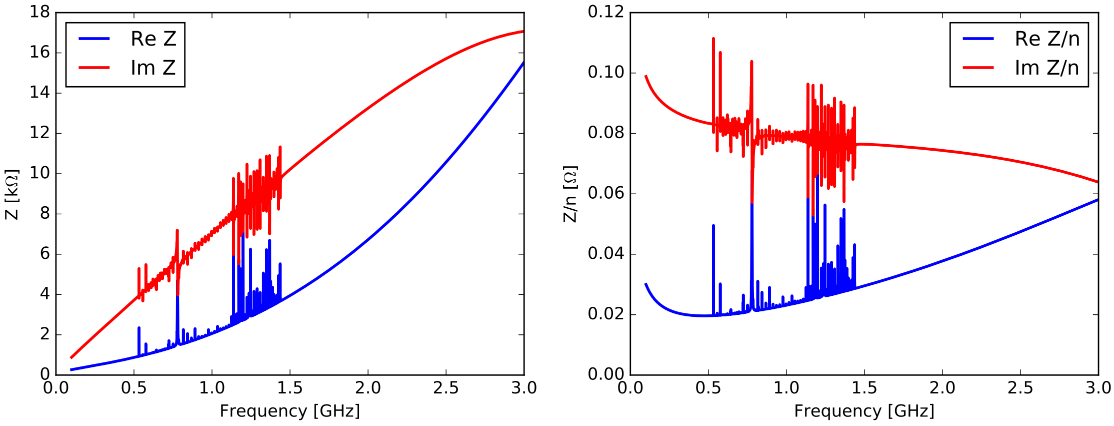

(a) Real and imaginary part of Z

(b) Real and imaginary part of Z/n

Figure 3.1 – Real (blue) and imaginary (red) part of the LHC impedance model [64], in natural scale (left) and divided by $n = \omega/\omega_o$ (right).

In addition, the peculiarities of the LHC operation complicate the measurements. For instance, as the acceleration ramp is extremely slow (10 – 20 min) compared to smaller, normal-conducting machines, single-bunch studies during the ramp and on the flat top are not feasible due to the excessive time that would be required. For that reason, most of the measurements were done by injecting 8 bunches spaced by one ninth of the ring (9.9 µs)[1]. We assumed that distance is sufficient to be able to neglect any interaction between bunches and was chosen to increase the statistics. With more knowledge acquired, the number of bunches was increased to 20 with a spacing of 4 µs and still no coupling between the bunches was observed.

For all the measurements presented below, we assumed that the impedance of both rings is identical, as they are approximately of the same length and both have practically the same machine components.

3.2 Resistive impedance

The resistive part of the impedance leads to a beam energy loss that is compensated by the rf system, and that can be measured from the bunch phase shift, as described in Section 1.2.1. The phase shift can be computed numerically using the LHC impedance model and Eq. (1.75), and the result is shown in Fig. 3.2. As one can see, the phase shift for bunches with a difference

---

[1] The ninth bucket cannot be filled as it falls inside the Abort Gap, a 3 µs gap that must contain no beam to allow the safe operation of the beam dump system [1].

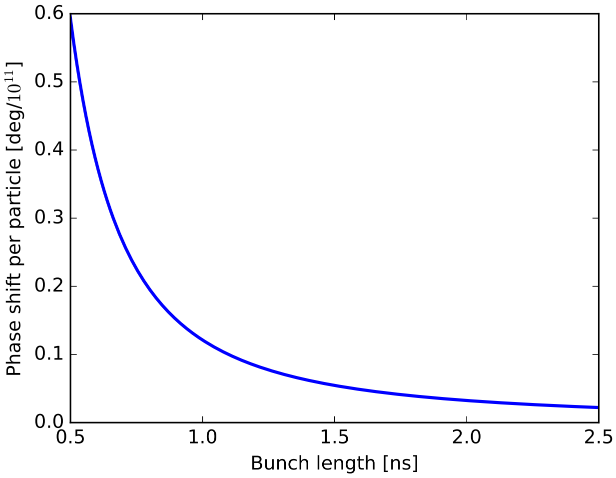

Figure 3.2 – Bunch phase shift per particle as a function of bunch length at 450 GeV with $V_{\mathrm{rf}} = 6$ MV, calculated using the LHC impedance model and Eq. (1.75).

in intensity of 1×10^{11} is expected to be smaller than 0.1 deg, so a very high accuracy is required for the phase measurements.

Although the total resistive impedance of the LHC is relatively small, it is not perfectly evenly distributed along the ring. There are several devices with a high resistive impedance compared to the rest of the machine. The beam energy loss due to those impedances is transferred to the devices, producing a heating (called beam-induced heating) that must be dissipated.

During the LHC run 1, and especially in 2011, operation was limited by beam-induced heating in some elements, as in the injection kickers (MKI) and some collimators. A few devices were even damaged, e.g., the synchrotron radiation telescope (BSRT) and the injection beam stopper (TDI) [43]. Since then, several measures have been put in place to avoid such problems [66]. For example, the bunch length during collisions was increased with respect to the nominal value (up to 1.35 ns, instead of 1 ns) and several devices were redesigned to reduce their resistive impedance (e.g., MKI, BSRT, TDI) or to improve the cooling capacities (collimators) [67].

3.2.1 Phase shift measurements

An attempt to probe the resistive part of the longitudinal impedance of the LHC was done using phase shift measurements, described in Section 2.3.3 [68].

Two MD sessions were devoted to these measurements in 2012, during which the phase shift dependence on bunch intensity was measured for 8 bunches with intensities in the range $(0.7-2.4) \times 10^{11}$. The first MD comprised three fills with different injected longitudinal emittances (0.8, 0.45, and 0.55 eVs) [69], and the second one had one long fill with small injected longitudinal emittances (0.45 eVs) [70].

Measurements were done at injection energy (450 GeV) and with an rf voltage of 6 MV, acquiring the phase of all bunches continuously for a long time to have a natural longitudinal emittance growth. This provided us with data for a wide range of bunch lengths, covering all values that are used in operation.

The results of both MDs, shown in Fig. 3.3, represent the phase shift per particle as a function of the average bunch length. A large difference is observed between Beam 1 (blue) and Beam 2 (red), and even between the different fills of Beam 2. A comparison with the estimation from the LHC impedance model, assuming Gaussian bunches, reveals up to a factor 3 larger than expected phase shift in measurements.

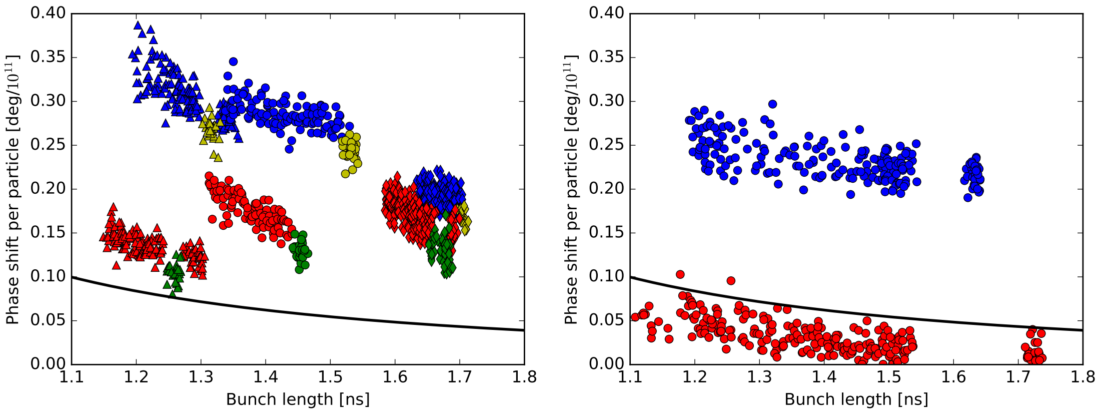

(a) MD #1 2012

(b) MD #2 2012

Figure 3.3 – Phase shift per particle as a function of bunch length measured at 450 GeV for Beam 1 (blue symbols) and Beam 2 (red symbols), compared to the estimation using Eq. (1.75) for Gaussian bunches (solid line). Data was acquired during the MDs on April 21, 2012 (left), and on June 20, 2012 (right). Note the reduction in the phase shift when the TDI jaws were retracted (yellow and green for Beam 1 and Beam 2, respectively). Different symbols are are used to indicate different fills. The rf voltage was 6 MV.

The reasons for the discrepancy between measurements and the model are being investigated. Given the extremely small phase shift due to the impedance, one potential issue would be a systematic error in the phase measurements that would depend on the amplitude of the measured signal at 400 MHz, which depends on the bunch intensity and length. Another error could be introduced by the spread in bunch length between the 8 bunches during the measurements, which was up to ±200 ps in some cases, and by a difference in the particle distribution between the bunches.

3.2.2 TDI impedance

Although the resistive impedance of the LHC could not be accurately estimated from the bunch phase shift, relative measurements were possible for movable devices with high impedance, as it is the case of the injection beam stopper (TDI), shown in Fig. 3.4. The TDI is a protection device consisting of two ~4.2 m long jaws that can be inserted very close to the beam (~7 σ) during the injection process to protect the machine in case of a kicker magnet fault [71]. There are two of them, one per ring. The relatively high resistivity of a portion of the jaw coating (Ti) and the proximity to the beam when the jaws are inserted, plus some geometrical considerations, make the resistive impedance of the TDI to account for about 15% of the total beam power loss at injection.

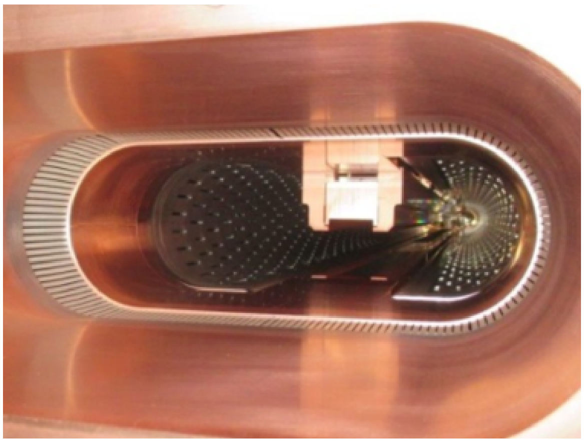

Figure 3.4 – Picture of the TDI with the upper jaw inserted and the bottom jaw retracted.

Following the LHC intensity ramp up in 2011, pressure rises in the region near both TDIs were later correlated with temperature increases of the TDIs [72]. The TDI beam screens were also deformed, probably due to heating, although other possibilities are not excluded (e.g., a beam impact). Beam measurements were carried out to check if the cause of those observations was related to beam-induced heating due to the TDI resistive impedance.

During the phase shift measurements shown in Fig. 3.3, the TDI jaws were retracted and inserted back to check whether its impedance could be estimated. A phase shift per particle of the order of 0.05 deg/10^{11} was measured for both TDIs, with an rf voltage of 6 MV, whereas a phase shift of the order of 0.01 deg/10^{11} is expected from simulations of the TDI impedance. The factor 5 larger shift observed was suspected to come from nonconformities in the TDIs.

During the Long Shutdown 1, the TDI beam screens were reinforced, but the geometry and the absorbing blocks were left unchanged (and therefore the impedance). Given that the pressure spikes and heating were still observed in 2015, more specific measurements were done. The bunch phase was measured for different TDI gap widths with a single bunch in each ring, with the bunch intensities being 0.93×10^{11} and 1.05×10^{11} for Beam 1 and Beam 2, respectively. Figure 3.5 shows the change of the bunch phase for each gap width, with a shift about twice larger for Beam 2, in agreement with the larger transverse tune shift seen in Beam 2. The dependence of the phase shift on the gap width, shown in Fig. 3.6, was found to be compatible with a resistive-wall impedance model, where the phase shift is inversely proportional to the gap width (e.g., [20]).

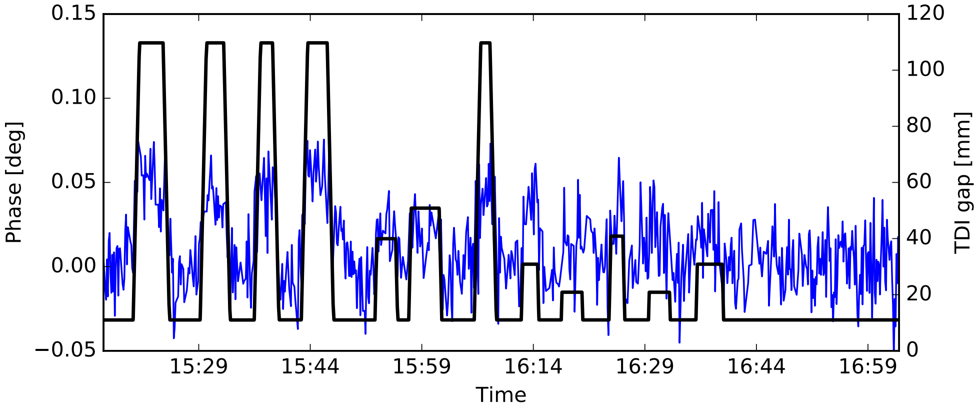

(a) Beam 1

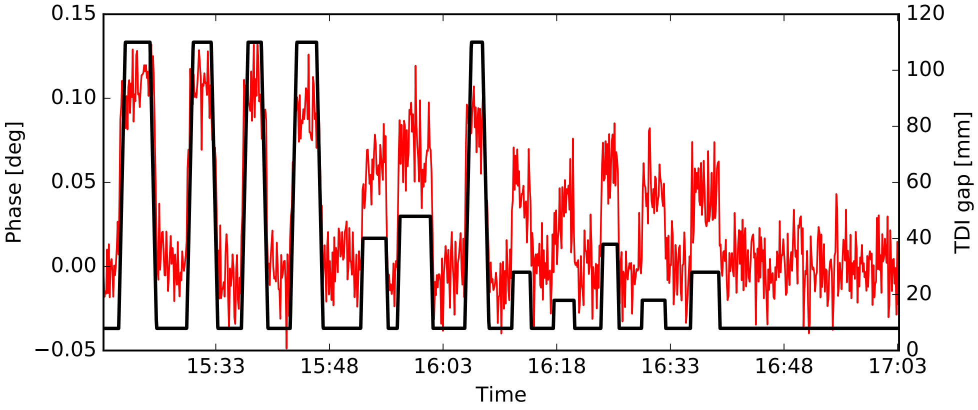

(b) Beam 2

Figure 3.5 – Measured bunch phase for Beam 1 (top, blue) and Beam 2 (bottom, red) during the movement of the TDI, shown together with the TDI gap (black). The bunch intensity was 0.93×10^{11} in Beam 1 and 1.05×10^{11} in Beam 2, and the rf voltage 6 MV. Data acquired on Oct. 30, 2015.

Later, a systematic analysis was run taking advantage of the fact that the TDI jaws are retracted at every fill before the acceleration ramp and that the bunch phase was automatically measured and logged during the second half of 2015. The phase shift was averaged for all bunches and it is shown in Fig. 3.7 for all the fills from August 2015 until the end of the proton run in November 2015. The factor two between measurements for Beam 1 and Beam 2 is present for all fills, and a linear dependence of the phase shift on the bunch intensity is observed, in agreement with Eq. (1.75). No apparent change of the phase shift per particle was noticed along time for different fills, meaning that the impedance did not change since the beginning of the run 2.

During the last year-end technical stop (YETS), the TDIs were taken out of the machine and their impedances were measured in January 2016 [73]. A damage was observed in the coating the TDI blocks, which was worse for the TDI of Beam 2, in agreement with these beam measurements. The power loss per particle was calculated using the measured impedances

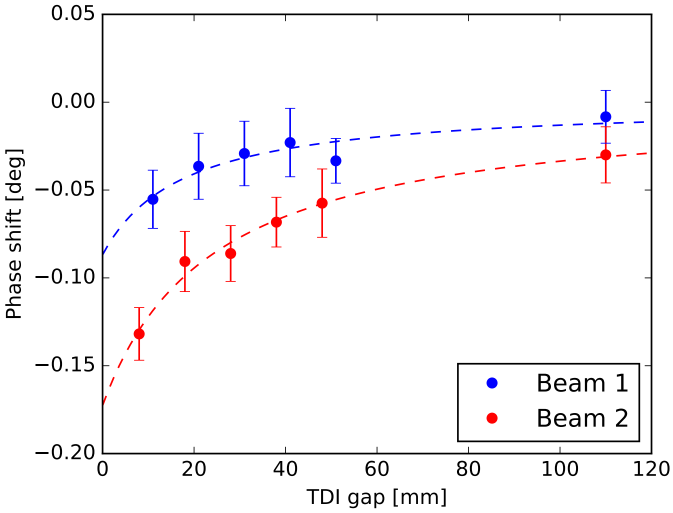

Figure 3.6 – Measured bunch phase shift $\Delta\phi_b$ for Beam 1 (blue circles) and Beam 2 (red circles) as a function of the TDI gap t_g, together with a fit $\Delta\phi_b \propto 1/t_g$ (dashed lines). The bunch intensity was 0.93×10^{11} in Beam 1 and 1.05×10^{11} in Beam 2, and the rf voltage was 6 MV. Data acquired on Oct. 30, 2015

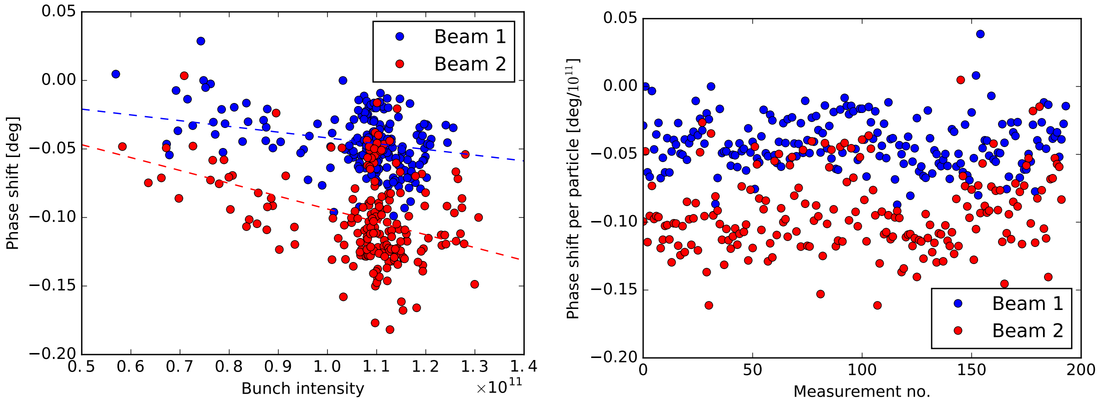

(a) Average phase shift as a function of the average bunch intensity

(b) Average phase shift evolution for different fills

Figure 3.7 – Average phase shift corresponding to the TDI retraction before the acceleration ramp in operational fills for Beam 1 (blue) and Beam 2 (red), as a function of the average bunch intensity (left) and the evolution over different fills (right). The dependence on bunch intensity is compatible with the effect of the resistive impedance (linear fit, dashed lines). The evolution along time suggests no further degradation of the TDI. The rf voltage was 6 MV during all the measurements.

and assuming a bunch length of 1.3 ns and a $\cos^2$ distribution, and it was found to be about 0.8×10^{-11} W for the TDI of Beam 1 and 1.2×10^{-11} W for the TDI of Beam 2. The phase shift per particle corresponding to that power loss is 0.04 deg/10^{11} for Beam 1 and 0.06 deg/10^{11} for Beam 2, which is in reasonably good agreement with the beam measurements shown in Fig. 3.7.

Before reinstalling the TDI back in the machine, the Ti-coated h-BN blocks were replaced with Cu coated graphite blocks, which have a reduced impedance and higher tolerance to coating problems. A new design is currently being developed for the HL-LHC, with an improved geometry to reduce also the high-order modes [74].

3.3 Reactive impedance

The effective reactive impedance can be estimated from measurements of the synchrotron frequency shift with intensity, as already mentioned in Section 1.2.1. Assuming Gaussian bunches, which is in general a good approximation in the LHC, with a 4-σ bunch length $\tau_{4\sigma}$, the expected synchrotron frequency shift can be found from Eq. (1.76):

$$\Delta f_s = f_{so} \left(\frac{2}{\pi}\right)^{1/2} \frac{16\, N_b\, q\, h^2\, \omega_o}{V_{\mathrm{rf}} \cos\phi_s\, (\omega_{\mathrm{rf}}\tau_{4\sigma})^3} \frac{\mathrm{Im} Z}{n}. \tag{3.1}$$

This formula is an approximation, as it was derived from the linearized equation of motion (1.69). To check the validity of this expression, the synchrotron frequency shift was computed numerically using Eq. (1.49) for the same bunch distribution, assuming a constant $\mathrm{Im}Z/n = 0.09\,\Omega$. The result is shown in Fig. 3.8, together with the shift calculated using Eq. (3.1). As can be seen, the approximation is very good in the bunch length range that we are interested in (1.0 – 1.6 ns).

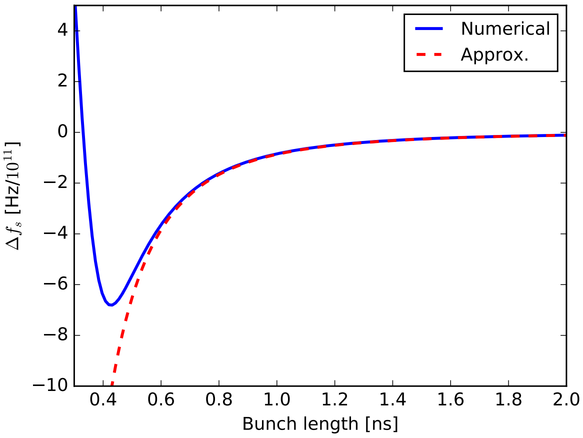

Figure 3.8 – Synchrotron frequency shift per particle as a function of the bunch length, computed numerically (blue) and using the approximated Eq. (3.1) (red), at 450 GeV and with V_{rf} = 6 MV. A pure imaginary impedance $\mathrm{Im}Z/n = 0.09\Omega$ and a Gaussian bunch with an intensity of 1×10^{11} were assumed.

Two methods were used to measure Δf_s in the LHC, from the peak-detected Schottky spectrum and applying an rf phase modulation. The details of each approach are described below.

3.3.1 Peak-detected Schottky spectrum

As already described in Section 2.3.2, the quadrupole line of the peak-detected Schottky spectrum can be used to get the particle distribution in synchrotron frequency [56], from which the incoherent synchrotron frequency can be obtained for bunches with different intensity and length.

Several measurements with different beam parameters were done in the course of the run 1. The most precise measurements were obtained during an MD session in 2012 [75]. For those measurements, 8 bunches with similar longitudinal emittance and different intensities, in the range (0.6–2.0) $\times 10^{11}$, were injected into each LHC ring.

Figure 3.9 shows the peak-detected Schottky spectrum for two bunches of Beam 1 with intensities of 6.2×10^{10} and 1.63×10^{11}, and a bunch length $\tau = 1.4$ ns. The frequency resolution of the measurement (0.2 Hz) is not sufficient to determine the synchrotron frequency shift with the required accuracy, but we can state that the shift in the quadrupole line is smaller than 1 Hz. For a difference in intensity of 1.0×10^{11}, we get an upper limit for the absolute value of the synchrotron frequency shift of 0.5 Hz, which is in agreement with the expected $\Delta f_s = -0.35$ Hz from Eq. (3.1).

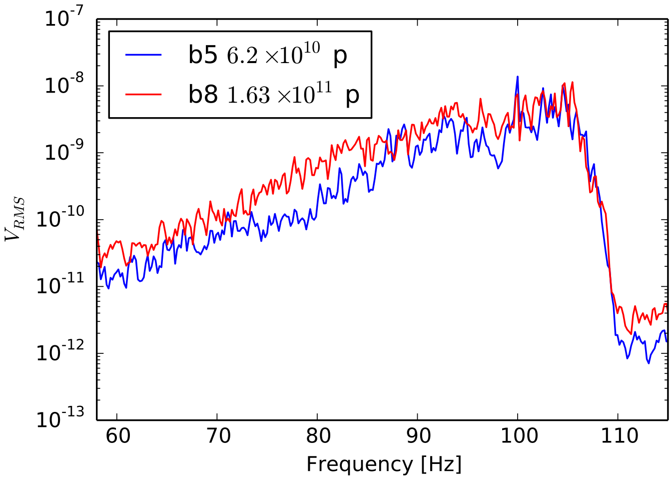

Figure 3.9 – Quadrupole line of the peak-detected Schottky spectrum of two bunches with different intensities and the same length $\tau = 1.4$ ns. The linear synchrotron frequency for zero intensity is $f_{so} = 55.1$ Hz for 450 GeV and $V_{\rm rf} = 6$ MV. During the measurements the phase loop was open. Data acquired during the MD on Nov. 28, 2012.

3.3.2 Sinusoidal rf phase modulation

Another set of measurements was made by applying an rf phase modulation at 450 GeV in order to estimate the incoherent synchrotron frequency shift [75, 76]. A sinusoidal rf phase modulation with a frequency slightly below the zero-amplitude synchrotron frequency should affect some particles and produce a parametric resonance inside the bunch (see e.g., [8]). If the modulation frequency is above the synchrotron frequency, then the bunch should not be excited.

A sinewave modulation with an amplitude of 0.25 deg was applied to the 8 bunches of Beam 2, which had similar longitudinal emittance and different intensities. The modulation frequency was reduced in steps of 0.1 Hz starting from the zero-amplitude linear synchrotron frequency (for zero intensity), which is f_{so} = 55.1 Hz for an rf voltage V_{rf} = 6 MV. The modulation was tested with a frequency of 55.3 Hz, higher than f_{so}, to verify that the bunches were not excited.

In order to check whether the bunches were affected by the phase modulation or not, the amplitude of the 400 MHz component of the bunch spectrum was observed. Figure 3.10 shows the derivative of this signal for each bunch, and its changes are correlated with the moments the rf phase modulation was applied.

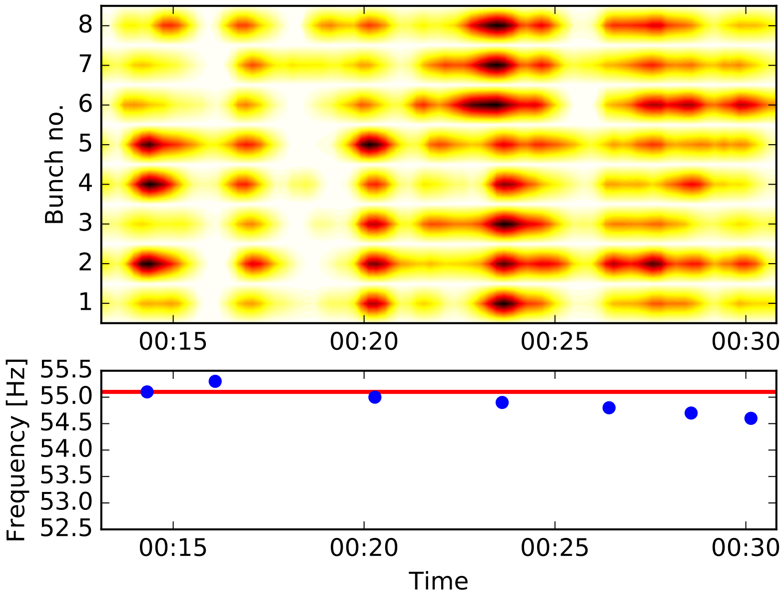

Figure 3.10 – Derivative of the 400 MHz component of the bunch spectrum for each bunch (top) and the frequency of the phase modulation at each time it was applied (bottom, blue circles). The linear synchrotron frequency (55.1 Hz) for zero intensity is shown for comparison (red line). Bunches can be considered as excited when the signal in the upper plot turns dark red or black. Data acquired during the MD on Nov. 28, 2012.

Measurements were done at injection energy and with the phase loop open, so the bunch length was increasing due to IBS and rf phase noise. This led to the fact that each bunch had a different length at the moment they were excited, making impossible a direct comparison.

Instead, these results were compared with the synchrotron frequency shift expected from Eq. (3.1). Table 3.1 summarizes the highest modulation frequency at which each bunch was seen to be excited, together with the corresponding bunch intensity and length at the moment of the phase modulation, and the synchrotron frequency shift expected for those parameters from Eq. (3.1).

Table 3.1 – Frequency of the sinusoidal rf phase modulation f_m at which each bunch was observed to be excited, bunch intensity and length at the moment of the phase modulation, together with the expected synchrotron frequency shift Δf_s calculated using Eq. (3.1) for $\mathrm{Im}Z/n = 0.09\ \Omega$.

f_m [Hz]	Bunch no.	N_b [10^{11}]	τ [ns]	Δf_s [Hz] (calc.)
55.1	2	0.81	1.18	-0.47
	4	0.66	1.20	-0.35
	5	0.71	1.23	-0.36
55.0	1	1.44	1.36	-0.54
	3	1.44	1.36	-0.54
54.9	6	2.04	1.41	-0.69
	7	1.93	1.38	-0.70
	8	1.84	1.43	-0.60

Although the relative frequency shift between different bunches agrees reasonably well with the expected values, the absolute frequency shift is off by about 0.3 – 0.4 Hz. This can be explained from the spectrum of the phase modulation that was applied (see Fig. 3.11). In practice, a pure monochromatic modulation is not achievable. The bandwidth of the modulation is defined by its length in time: the longer the excitation, the narrower the main lobe of the spectrum. In our case, the amplitude of the modulation was a trapezoid, in order to be adiabatic and to avoid exciting the particles in the bunch tails or coherent oscillation modes. Due to some hardware limitations, the length of a trapezoid was limited to 3.3 s, which gives a bandwidth of about ±0.3 Hz around the modulation frequency. By repeating the trapezoid three times, the main lobe becomes narrower, but the amplitude of the side lobes does not change, as shown in Fig. 3.11.

This method has potential to become one of the most accurate techniques to measure the synchrotron frequency shift in the LHC. The required improvements include a longer excitation time, which is already available, and possibly measurements at top energy, which will benefit from lower IBS growth rate. Bunch lengths should be well defined by the controlled emittance blowup during the ramp, with a smaller spread between the bunches. In addition, smaller bunch lengths could be achieved at high energy, which should increase the synchrotron frequency shifts and ease the measurements.

The rf phase modulation can also be used to flatten the particle distribution in phase space when applied at a frequency slightly lower than the synchrotron frequency (~3% below f_{so}). This method has already been used for different purposes in various machines, as for example

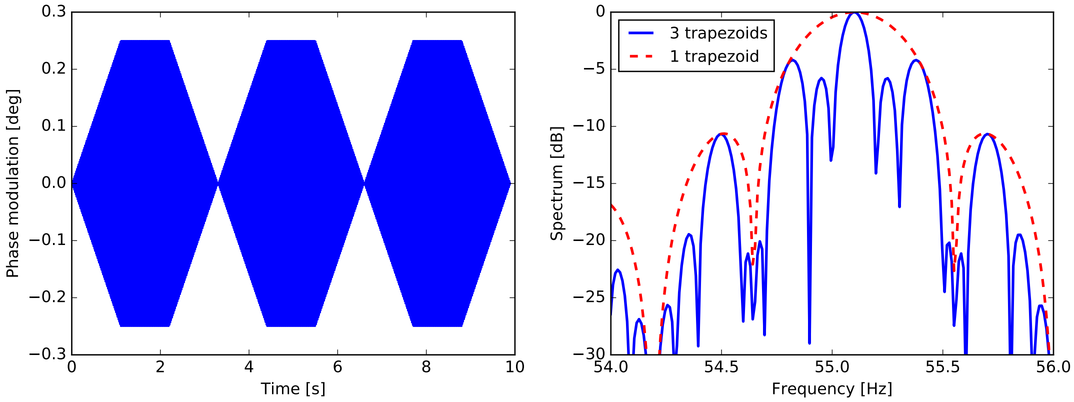

(a) Phase modulation in time domain

(b) Power spectrum of the phase modulation

Figure 3.11 – Phase modulation in time domain (left) and its normalized power spectrum (right), as applied during the MD. This example corresponds to 3 trapezoids, each of them with a length of 3.3 s, an amplitude of 0.25 deg, and a frequency of 55.1 Hz. Note the side lobes with about -4 dB amplitude at ±0.3 Hz with respect to the modulation frequency. The spectrum for the case with a single trapezoid is shown for comparison (dashed red line).

to reduce the space-charge effect in the CERN PS [77, 78] or to stabilize the beam in the Fermilab Tevatron [79], and it has been tested in the LHC in order to reduce the beam-induced heating in some machine components [75]. It is also being considered to be used in the LHC in 2016 for controlled emittance blowup at top energy with nearly no losses, which can be useful for bunch length leveling and for beam stability.

3.4 Measurements of the loss of Landau damping threshold

Measurements of the loss of Landau damping threshold were found to be the most accurate method to probe the reactive part of the LHC longitudinal impedance. Several MD sessions were devoted to study the single-bunch stability in the LHC, including observations during the acceleration ramp and measurements at a constant beam energy. The goal was to check whether the stability threshold is compatible with the loss of Landau damping, and to precisely determine the stability threshold, which can be then used to estimate the imaginary part of the effective impedance. Here we review the most important results obtained during the run 1 and the first year of the run 2 (2015).

3.4.1 Loss of Landau damping during the ramp

Longitudinal instabilities were observed in the LHC for the first time at the beginning of the run 1 in 2010, when one bunch with nominal intensity ($\sim 1.15 \times 10^{11}$) was injected into each ring and became unstable during the acceleration to 3.5 TeV [80]. The longitudinal emittance of those bunches was about 0.38 eVs, much smaller than the one in the LHC Design Report

(1.0 eVs). Later, bunches with emittances of 0.5 and 0.6 eVs were successfully accelerated to 3.5 TeV, but then they became unstable at flat top.

In order to confirm the source of this instability, a series of test fills were carried out during MD sessions, with the aim of checking if the instability threshold was following the scaling law of loss of Landau damping, described by Eq. (1.94).

In order to achieve a higher sensitivity in the measurements, it is a good choice to inject bunches with similar bunch intensities, but different longitudinal emittances. In that case, neglecting the dependence on the rf voltage ($E_{\mathrm{th}} \propto V_{\mathrm{rf}}^{1/5}$), the beam energy threshold E_{th} scales during the ramp as:

$$E_{\mathrm{th}} \propto \varepsilon^2. \tag{3.2}$$

To cope with the differences in bunch intensity, in our analysis we introduced a beam parameter ε_r, which can be considered as a rescaled longitudinal emittance, taking into account the scaling of the loss of Landau damping with intensity. The rescaled emittance ε_r is then defined with respect to the average bunch intensity $\overline{N}_b$ as

$$\varepsilon_r = \varepsilon \left(\frac{\overline{N}_b}{N_b} \right)^{2/5}. \tag{3.3}$$

We observed the bunch phase to determine whether bunches are performing dipole oscillations or not, and the threshold of stability is finally defined from the amplitude of these oscillations. This method requires that a threshold should be defined for the amplitude of the oscillations, and this can be rather complicated. In general, the amplitude of the dipole oscillations for stable bunches is mainly dominated by the measurement noise and rf phase noise, but it can also be affected by many different sources: slowly damped oscillations due to injection phase error, coupling with unstable bunches through the phase loop, etc. Therefore, a careful analysis of each particular case is required to differentiate between stable and unstable cases. As an example, Fig. 3.12 shows the amplitude of the dipole oscillations for a stable and an unstable bunch through the ramp.

This method is only valid for verification of the agreement between measurements and the scaling law of loss of Landau damping, and it cannot be used to determine the stability threshold accurately (nor the impedance). This is because the method is very sensitive to any change of the threshold of the phase oscillation amplitude, as the energy continuously changes during the ramp.

It is important to remember that the loss of Landau damping does not necessarily lead to instability, as already mentioned in Section 1.2.3. However, as many parameters are continuously changing during acceleration, the beam is easily excited, and undamped oscillations can be observed in case of loss of Landau damping.

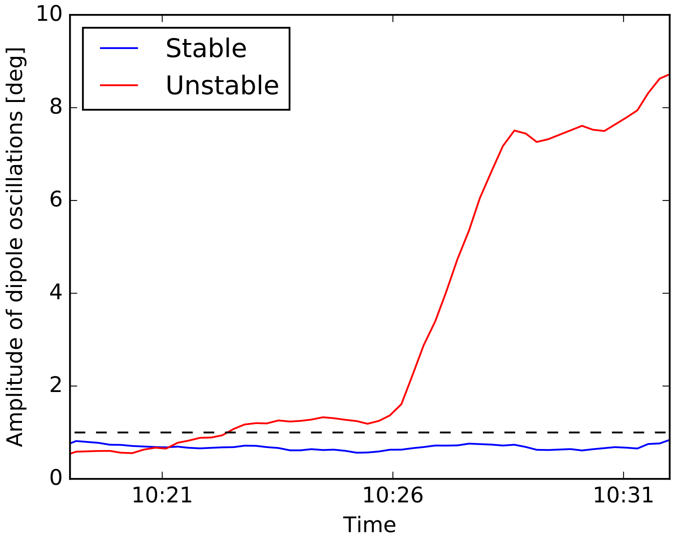

Figure 3.12 – Amplitude of the dipole oscillations for a stable (blue) and an unstable (red) bunch during acceleration to 4 TeV. The horizontal dashed line represents the threshold chosen for this case. The data has been smoothed for accurate determination of the threshold.

Acceleration to 3.5 TeV

In 2011, two MD sessions were dedicated to the study of loss of Landau damping during the acceleration ramp.

During the first MD in 2011 [81], 8 bunches with an intensity in the range $(1.4-1.6)\times10^{11}$ and different longitudinal emittances (0.3 – 0.7 eVs) were injected from the SPS. The longitudinal emittance range was covered by varying the parameters of controlled emittance blowup in the SPS. In the LHC, the phase loop was configured to lock only on the first injected bunch, and the bunches were accelerated to 3.5 TeV.

The bunch phase was measured during the acceleration, and the energy at which the bunches started to perform undamped dipole oscillations was considered to be the threshold. In Fig. 3.13, the energy threshold is shown as a function of the longitudinal emittance. A quadratic fit is also plotted to show a dependence similar to the expected from loss of Landau damping, shown in Eq. (3.2). The first results were not fully conclusive for various reasons. Indeed, due to the phase loop settings, the first bunch was stabilized and could not be considered. Also, as the phase loop reduces the rf phase noise, some bunches were very weakly excited and for those the threshold could not be properly defined.

During the second MD in 2011 [82], a similar experiment was carried out. In that case, the bunch intensity was slightly reduced and was in the range $(1.25-1.55)\times10^{11}$. The longitudinal emittance was in the range 0.4 – 0.55 eVs. The main difference from the previous MD was in the phase loop settings: this time it was used as in operation, acting on the average phase of all bunches.

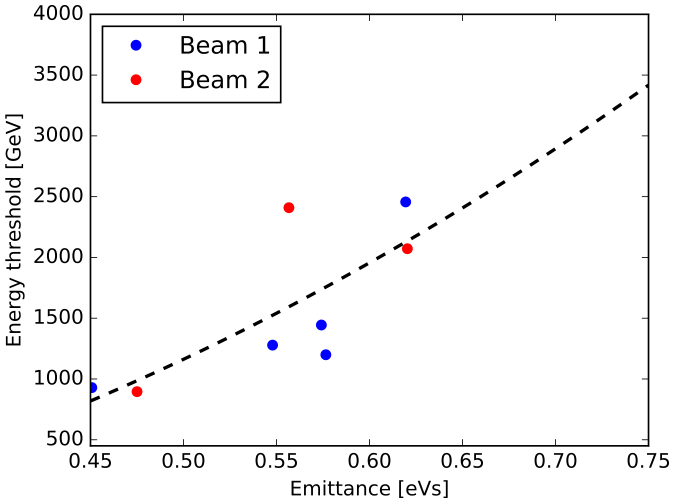

Figure 3.13 – Energy at which the bunch became unstable as a function of the scaled longitudinal emittance ε_r, for Beam 1 (blue) and Beam 2 (red). The dashed line is a quadratic fit $E_{\text{th}} \propto \varepsilon_r^2$. Data acquired during the MD on May 5, 2011. $\overline{N}_b = 1.5 \times 10^{11}$.

As in the previous MD, the bunch phase was monitored during the ramp. Some bunches became unstable, but the phase loop was coupling different bunches and made difficult to distinguish between those that lost Landau damping and those that were excited by the coupling through the phase loop.

Acceleration to 4 TeV

In 2012, the same test was repeated, this time with the phase loop off during the acceleration to 4 TeV [70]. The intensities of the 8 bunches injected in each ring varied from 7×10^{10} to 2.4×10^{11}, and the longitudinal emittance was in the range 0.55 – 0.7 eVs. In order to damp the injection oscillations, the phase loop was on at flat bottom and was open just before the start of the ramp.

The energy at which undamped oscillations were observed was defined as the stability threshold. Figure 3.14 shows the dependence of the threshold on the longitudinal emittance ε_r, rescaled according to Eq. (3.3). Some bunches with larger emittance and lower intensity remained stable during the ramp. The plot shows a very good agreement with the scaling of loss of Landau damping.

3.4.2 Loss of Landau damping at constant beam energy

In order to gain more knowledge about the single-bunch instability observed in the LHC, another series of MD sessions were devoted to measurements of the threshold of loss of Landau damping accurately.

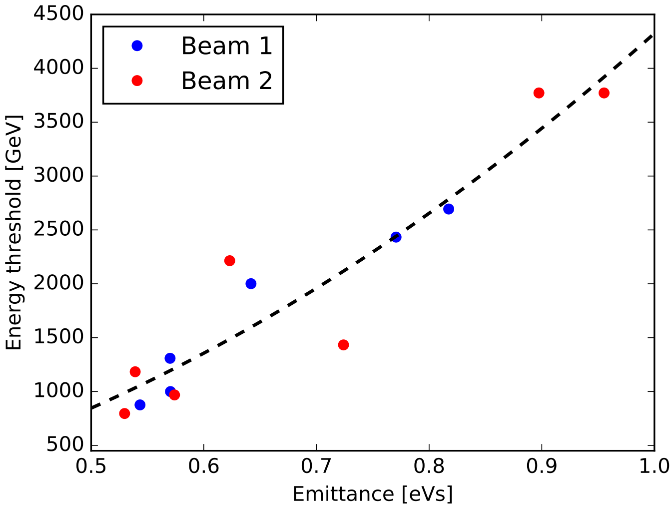

Figure 3.14 – Energy at which the bunch became unstable as a function of the scaled longitudinal emittance ε_r, for Beam 1 (blue) and Beam 2 (red). The dashed line is a quadratic fit $E_{\text{th}} \propto \varepsilon_r^2$. Data acquired during the MD on June 20, 2012. $\overline{N}_b = 1.93 \times 10^{11}$.

The scaling law of loss of Landau damping given by Eq. (1.94) can also be rewritten as a function of the bunch length τ:

$$(\text{Im}Z/n)_{\text{th}} \propto \frac{\tau^5 V}{N_b}. \tag{3.4}$$

The right-hand side of Eq. (3.4) is used in the following as a stability parameter ξ [83]

$$\xi = \frac{\tau^5 V}{N_b}. \tag{3.5}$$

In order to determine the stability threshold, first the stability parameter ξ is calculated for each bunch. Then we select from the unstable bunches the one with the highest ξ, and from the stable bunches the one with the lowest ξ. The average of these two values gives the stability threshold ξ_{th}, and the difference between them the error bar.

Determining the level of stability from measurements of the bunch phase can be rather intricate, for the same reasons as for the measurements during acceleration. The situation is different for the measurements done at injection as compared to the ones done at top energy, and each case is described below in detail.

Stability threshold at 450 GeV

At injection energy, the injection phase error can be used as the excitation needed to check if Landau damping is lost. However, it is a parameter that cannot be easily controlled and that dominates the bunch behavior after injection. For stable bunches, the injection phase error initiates slowly damped oscillations. For unstable bunches, it can produce undamped oscillations due to loss of Landau damping, but in some cases it can also be seen as damped oscillations due to filamentation, which causes longitudinal emittance blowup that stabilizes the bunch.

The criterion chosen to differentiate between stable and unstable bunches is to compare the growth rate of the amplitude of phase oscillations for different bunches a few minutes after injection. Figure 3.15 shows examples of the amplitude signal for stable and unstable bunches, the former with approximately zero growth rate, the latter with a positive growth rate.

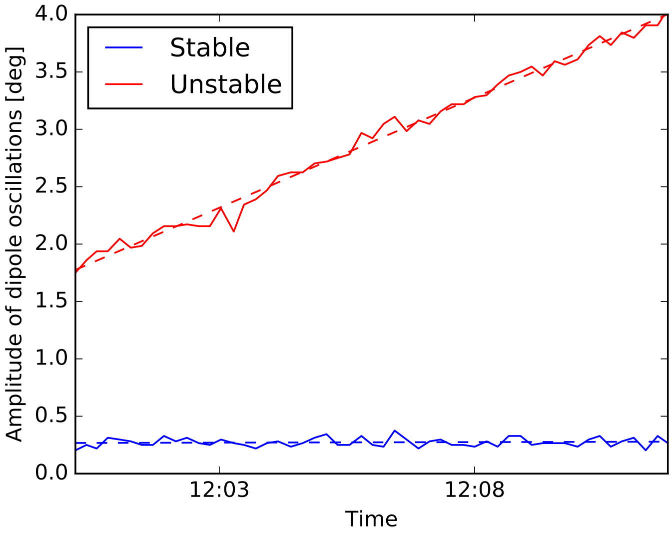

Figure 3.15 – Amplitude of the dipole oscillations for a stable (blue) and an unstable (red) bunch after injection (450 GeV). The dashed lines are linear fits to the amplitude signal, from which the growth rate is extracted. Data acquired during the MD on May 5, 2011.

Two MDs were carried out in 2011 for studies at injection energy. During the first one [81], eight bunches with similar emittances (0.35 – 0.4 eVs) and intensities ($\sim 1.6 \times 10^{11}$) were injected and the bunch phase was observed. The rf voltage at injection was 5 MV and the phase loop was locked on the first injected bunch. Some bunches of Beam 1 were unstable, but all bunches of Beam 2 were stable, as the injection phase errors were significantly larger for that Beam and caused emittance blowup at injection due to filamentation that stabilized the bunches. Measurement results based on the stability criterion described above are shown in Fig. 3.16. The stability threshold, defined from the stability parameter ξ in Eq. (3.5), was found to be $\xi_{\mathrm{th}} = (4.9 \pm 0.2) \times 10^{-5}\,(\mathrm{ns})^5\,\mathrm{V}$.

In the second MD [82], measurements were made during 6 fills at injection energy with the phase loop on, locked on all bunches. Different emittances (0.35 – 0.5 eVs) were injected in different rf voltages (3.8, 6, and 8 MV). In all cases, the dipole oscillations were damped by the phase loop and no instability was observed.

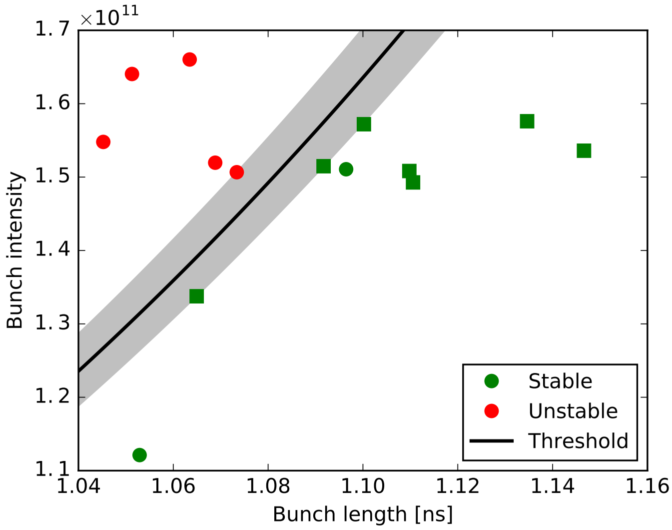

Figure 3.16 – Bunch intensity and length of stable (green) and unstable (red) bunches. The line is the estimated stability threshold at 450 GeV with 5 MV rf voltage. The shaded area represents the uncertainty in the measured threshold. Circles are used for Beam 1 and squares for Beam 2. Data acquired during the MD on May 5, 2011.

Stability threshold at 4 TeV and at 6.5 TeV

In order to find the stability threshold at the LHC flat top, it is important to keep the bunches stable during the acceleration, but some of them should become unstable after the arrival to the flat top. For that reason, in our measurements the phase loop was on both at injection, to damp oscillations due to injection phase errors, and also during the ramp, to minimize the rf phase noise. This should prevent the bunches that are at the limit of loss of Landau damping from becoming unstable. Then, on the flat top, the phase loop is kept closed for a few minutes in order to disentangle oscillations from transients that might occur at this moment. Finally, the phase loop was opened and this was used to excite the bunches, so that their stability could be observed.

To determine for which bunches oscillations are damped and for which they are not, the phase of each bunch was monitored. Taking into account the dependence of the instability threshold on the amplitude of the residual phase oscillations at injection energy and the possible excitation during the ramp, the threshold is defined for each particular fill and Beam by comparing with the bunches that show an approximately constant and small amplitude of dipole oscillations (stable). An example of these signals for stable and unstable bunches is shown in Fig. 3.17.

During an MD in 2012 [84], bunches of similar longitudinal emittance and different intensities in the range of $(0.5-1.5)\times 10^{11}$ were injected into each ring of the LHC. Then, they were accelerated to 4 TeV with controlled longitudinal emittance blowup using a target bunch length of 0.8 ns, which corresponds to an emittance of ~1 eVs at 12 MV. Due to time constraints, only 3 bunches per ring could be injected into the LHC. From these measurements, shown in Fig. 3.18, the stability threshold was found to be $\xi_{\text{th}} = (5.7 \pm 1.2) \times 10^{-5}\,(\text{ns})^5\,\text{V}$.

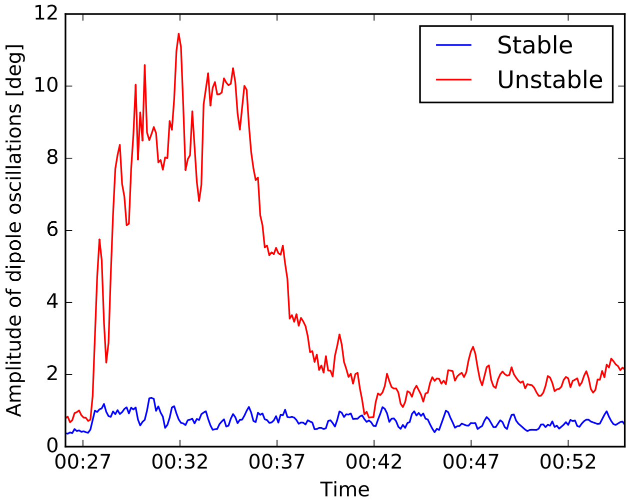

Figure 3.17 – Amplitude of the dipole oscillations for a stable (blue) and an unstable (red) bunch. The bunch phases were acquired a few minutes after arrival to flat top. The phase loop was opened at 00:27, and one of the bunches became very quickly unstable.

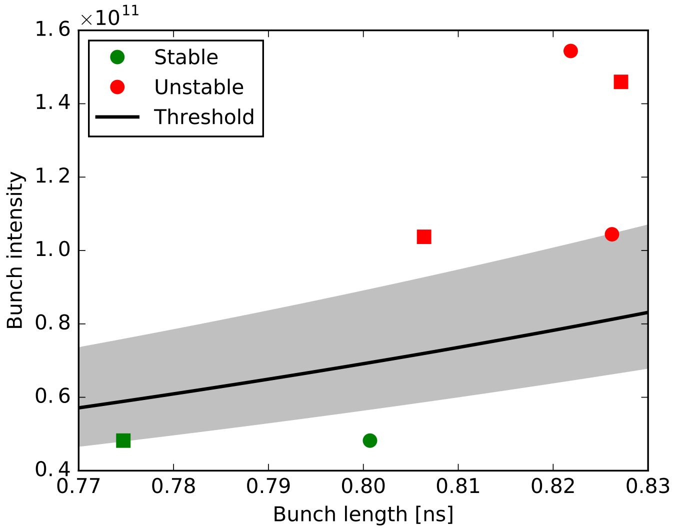

Figure 3.18 – Bunch intensity and length of stable (green) and unstable (red) bunches. The line is the estimated stability threshold at 4 TeV with 12 MV rf voltage. The shaded area represents the uncertainty of the measured threshold. Circles are used for Beam 1 and squares for Beam 2. Data acquired during the MD on Oct. 11, 2012.

In 2015, two similar MDs were carried out to obtain the stability threshold at 6.5 TeV with high accuracy [83]. During the first MD, we had two fills with similar conditions. Eight bunches with an emittance of about 0.45 eVs and intensities in the range $(0.4-1.6)\times 10^{11}$ were injected in each ring, and they were accelerated to 6.5 TeV with phase loop on and a target bunch length of 0.85 ns for the controlled longitudinal emittance blowup.

However, probably due to differences in bunch parameters, some bunches were not affected by the blowup. As a result, some bunches became unstable during the ramp and a large spread in bunch length was produced at arrival to flat top, as it can be seen in Fig. 3.19.

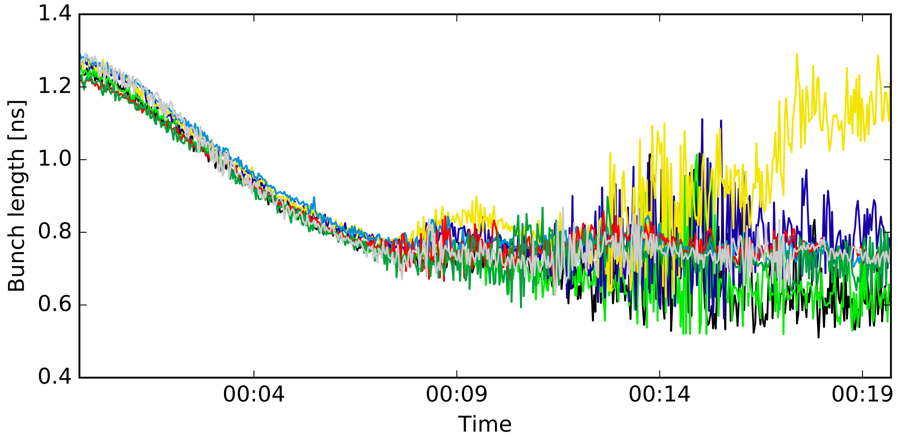

Figure 3.19 – Bunch length evolution during the ramp of the 8 bunches of Beam 2. Some bunches seem not to be affected by the controlled emittance blowup and become unstable. The unstable bunches then perform quadrupole oscillations and experience uncontrolled emittance blowup. Data acquired during the MD on July 20, 2015 (Fill 4024).

During the second MD, the same experiment was repeated, but this time injecting 20 bunches per ring. The intensity range was similar, $(0.4 - 1.4) \times 10^{11}$, and the longitudinal emittance was also around 0.45 eVs. In order to avoid problems with the controlled emittance blowup during the ramp, the blowup was done at 450 GeV. The rf voltage was increased to 16 MV to maximize the bucket area, required to blow the bunches up to 1.3 eVs (1.6 ns).

Based on the same criterion as used for the measurements at 4 TeV, the cases of stable and unstable bunches in Beam 1 and 2, for both MDs, are shown in Fig. 3.20 as functions of intensity and bunch length. The stability threshold was found to be $\xi_{\mathrm{th}} = (5.3 \pm 0.7) \times 10^{-5}\,(\mathrm{ns})^5\,\mathrm{V}$ from measurements in the first MD and $\xi_{\mathrm{th}} = (4.8 \pm 0.7) \times 10^{-5}\,(\mathrm{ns})^5\,\mathrm{V}$ from the second MD. If we combine both results, we get a threshold of $\xi_{\mathrm{th}} = (5.0 \pm 0.5) \times 10^{-5}\,(\mathrm{ns})^5\,\mathrm{V}$.

Summary of stability threshold measurements

Figure 3.21 summarizes all the measurements of the stability threshold done in the LHC between 2011 and 2015. Note the good agreement between measurements made for different beam parameters and at various energies.

For simplicity, the uncertainty in measurements of the bunch length and intensity has been neglected in the calculation of the error bar of the stability threshold. This approximation is acceptable if the number of measurements is sufficiently large. Therefore, the results of measurements at 450 GeV and 4 TeV are not very reliable, as only a reduced amount of data was available and a small range of bunch intensities and lengths were covered.

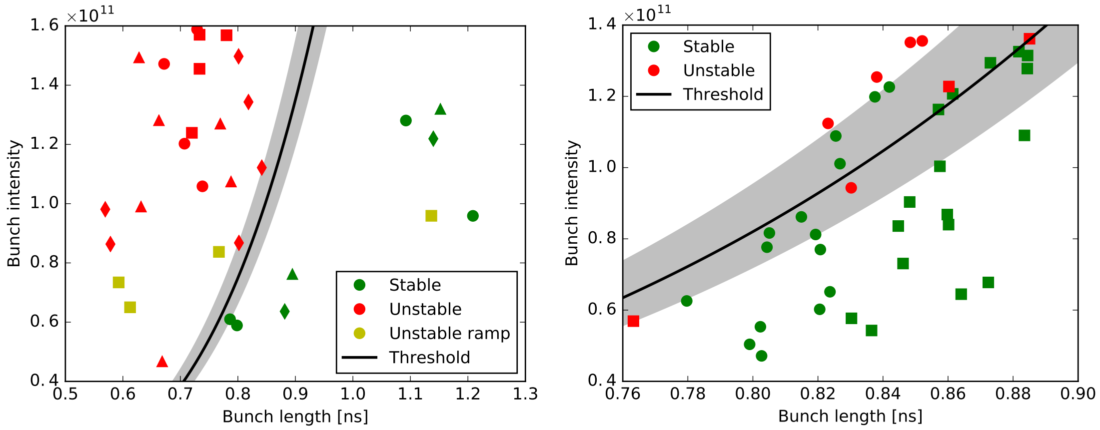

(a) MD #1 2015

(b) MD #2 2015

Figure 3.20 – Cases of stable (green) and unstable (red) bunches in the intensity and bunch length range covered by the two MDs in 2015. The line is the estimated stability threshold at 6.5 TeV with 12 MV rf voltage. The shaded area represents the uncertainty of the measured thresholds. Circles are used for Beam 1 and squares for Beam 2. On the left plot, diamonds are used for the second fill of Beam 1 and triangles for the second fill of Beam 2. Yellow squares are used for bunches that were unstable during the ramp and were not considered in the calculation of the threshold. Data acquired during the MDs on July 20, 2015 (left) and on Aug. 27, 2015 (right).

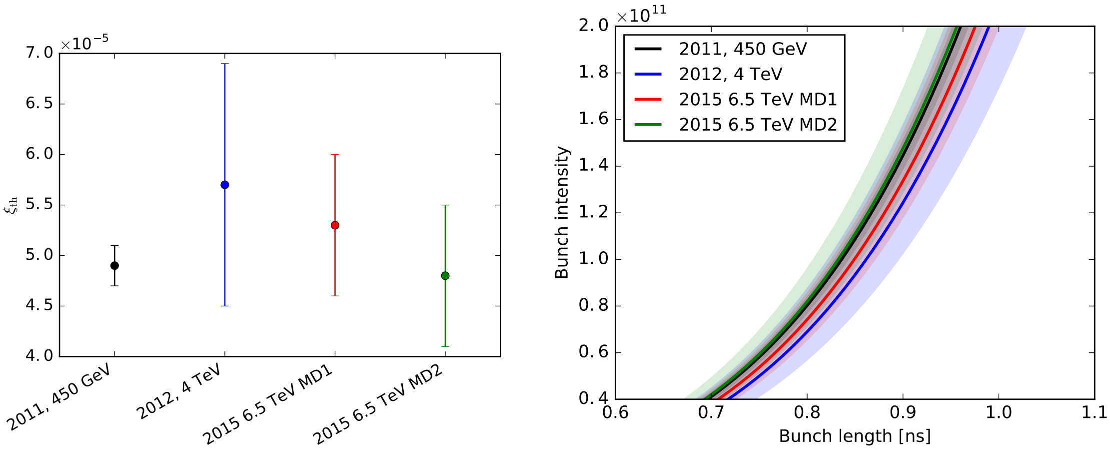

(a) Stability parameter found from different measurements

(b) Stability threshold as a function of bunch intensity and length at 12 MV

Figure 3.21 – Stability thresholds measured in 2011 at 450 GeV and 5 MV (black curve), in 2012 at 4 TeV with 12 MV (blue curve), and in 2015 at 6.5 TeV and 12 MV rf voltage during the first MD (red curve) and the second MD (green curve). On the left plot, the measured stability parameter ξ is shown. On the right plot, the stability threshold is represented as a function of bunch intensity and length at 12 MV. The shaded areas indicate the uncertainty of the measured threshold. The threshold measured at 450 GeV was scaled to 12 MV using Eq. (3.4).

In the following, we use the combined threshold measured at 6.5 TeV:

$$\xi_{\mathrm{th}} = (5.0 \pm 0.5) \times 10^{-5}\,(\mathrm{ns})^5\,\mathrm{V}, \tag{3.6}$$

which was obtained from three fills, a larger number of bunches, and is covering a wide range of bunch intensities and lengths (72 measurement points in total).

As follows from the value of ξ_{th} in Eq. (3.6), for a nominal bunch length of 1.05 ns (corresponding to an emittance of 2.07 eVs in 12 MV at 6.5 TeV), the threshold bunch intensity is $(3.1 \pm 0.3) \times 10^{11}$. Inversely, for the LHC nominal intensity of 1.15×10^{11}, the threshold emittance is (1.41 ± 0.05) eVs, corresponding to a bunch length of (0.86 ± 0.02) ns in 12 MV at 6.5 TeV.

The measured stability threshold defined by Eq. (3.6) was used to estimate the effective reactive impedance of the LHC using Eq. (1.93) and a value of $\mathrm{Im}Z/n \approx 0.05\ \Omega$ was obtained using a form factor $F = 1$. In order to match the impedance model value of $\mathrm{Im}Z/n = 0.09\ \Omega$, a form factor $F = 1.8$ has to be used.

3.4.3 Multi-bunch instability

During the design phase of the LHC, special attention was paid to minimizing the number of narrow-band impedances, as well as on reducing their shunt impedance and quality factor, so that the LHC could operate well below the coupled-bunch instability threshold since the start of the LHC operation. Several measurements have been done at injection energy and flat top, and no couple-bunch modes have been observed so far.

In 2011, bunch trains with different number of bunches with the LHC nominal bunch intensity and a small longitudinal emittance were injected into the LHC. In some cases, growing dipole oscillations were observed after injection, but after a small longitudinal emittance blowup due to IBS, the oscillations were slowly damped (see an example in Fig. 3.22). However, no coupled-bunch modes developed. The example in Fig. 3.22b shows the evolution of the stability parameter ξ with time for three equal bunch trains. Some bunches of the first two bunch trains were below the loss of Landau damping threshold defined by Eq. (3.6) after injection and became unstable, in agreement with the bunch phase observations in Fig. 3.22a . These results are therefore compatible with the single-bunch loss of Landau damping threshold shown above.

During the LHC run 2, in 2015, a longitudinal instability was observed at the end of two very long physics fills (~24 h) with up to 2040 bunches per ring. This instability is the result of the bunch shrinkage due to synchrotron radiation damping at 6.5 TeV [85]. Again, there was no sign of coupled-bunch instability and the threshold is in remarkably good agreement with single-bunch measurements of loss of Landau damping. Figure 3.23 shows the evolution of the stability parameter ξ from Eq. (3.5) during the fill, and when it crosses the threshold value measured with single bunches, the number of unstable bunches starts to increase. The bunch

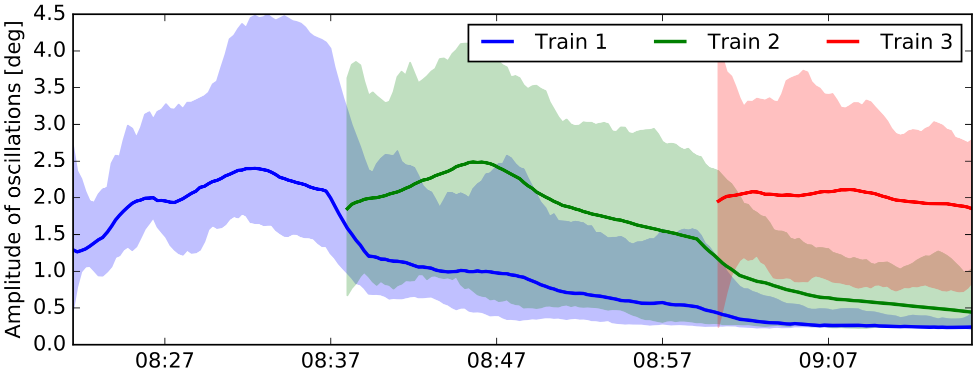

(a) Amplitude of dipole oscillations

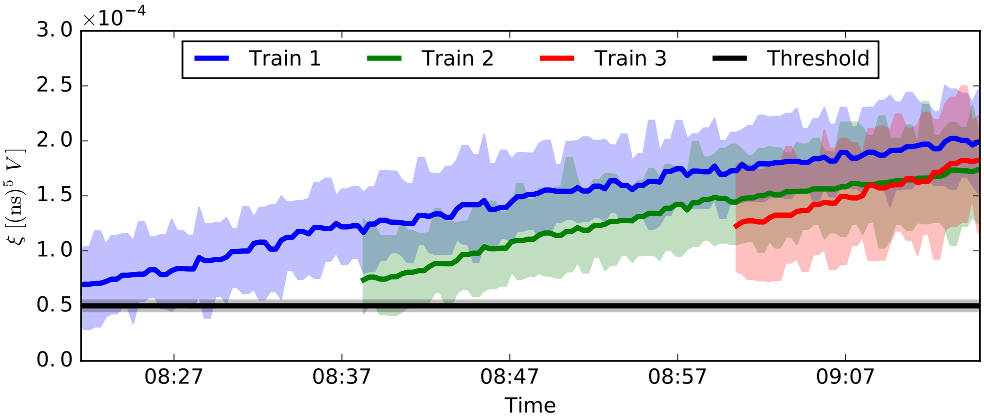

(b) Stability parameter ξ

Figure 3.22 – Average amplitude of the dipole oscillations (top) and stability parameter ξ (bottom) for 3 different bunch trains in Beam 1 after injection, together with shaded areas indicating the range covered from maximum to minimum values inside the bunch train. The first train had 12 bunches and the other two had 36 bunches each. The black line on the bottom plot is the measured stability threshold defined by Eq. (3.6), and the shaded black area is the uncertainty of the measured threshold. Some bunches of the first two bunch trains are below the stability threshold and perform dipole oscillations. The bunches of the last bunch train had a slightly larger longitudinal emittance and are more stable. Data acquired during the MD on May 8, 2011 (Fill 1772).

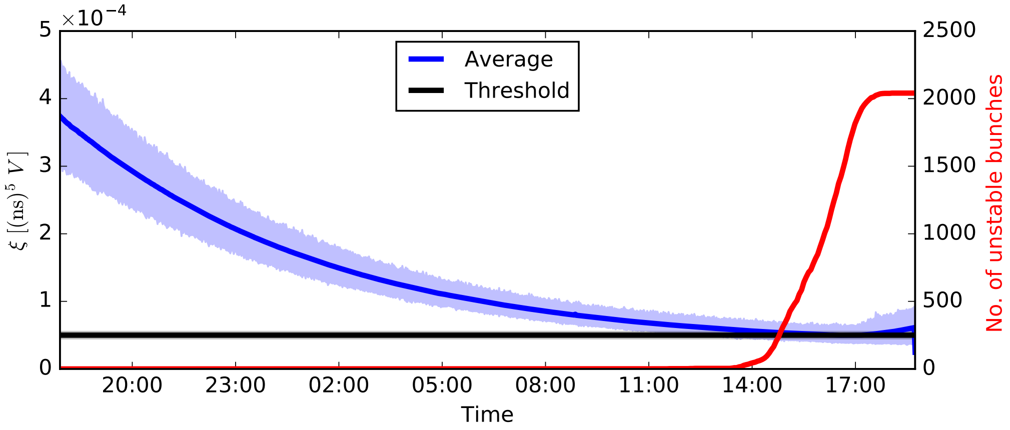

(a) Beam 1

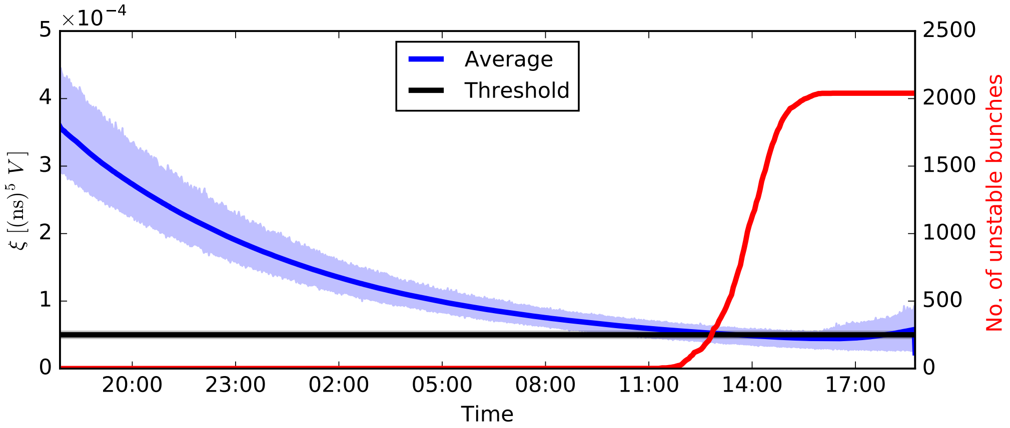

(b) Beam 2

Figure 3.23 – Evolution of the stability parameter ξ from Eq. (3.5) during the Fill 4538 (2015), averaged for all bunches (blue curve), together with the stability threshold (black line) for Beam 1 (top) and Beam 2 (bottom) defined by Eq. (3.6). The shaded blue area is the stability parameter variation from bunch-to-bunch. The red curve shows the number of bunches becoming unstable after the stability threshold is crossed.

intensity and length at the onset of the instability is shown in Fig. 3.24 for each bunch and they agree very well with the single-bunch threshold defined by Eq. (3.6).

The growth rate of the amplitude of the oscillations is very slow, of the order of hours. For example, when the beams were dumped in Fill 4538 (Fig. 3.23), the maximum amplitude of oscillations observed was around 10 deg and the LHC experiments were not concerned. However, the instability led to uncontrolled longitudinal emittance blowup and a small decrease of the peak luminosity.

In the near future, the bunch intensity in the LHC may be increased, and the bunch length at arrival to the flat top could be reduced to 1 ns. In that case, the instability could appear earlier in the cycle and be of higher concern for the experiments. One possibility to overcome this

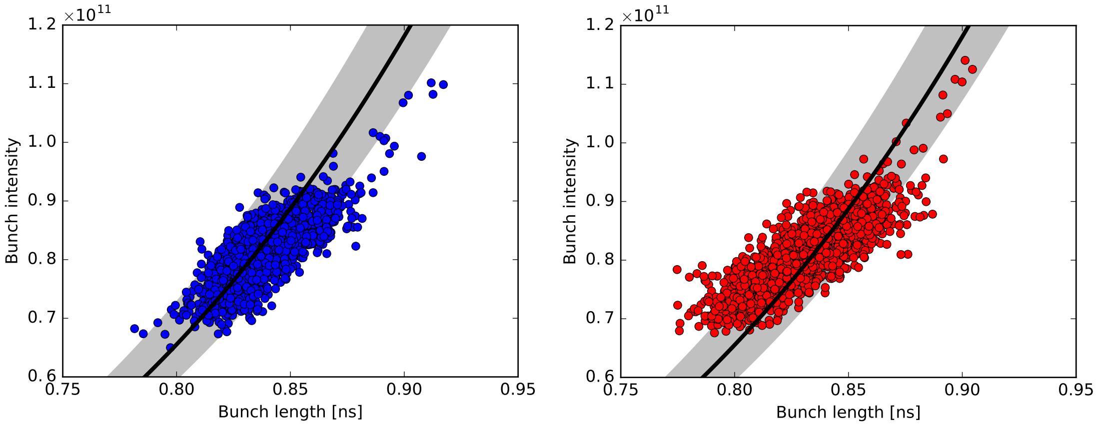

(a) Beam 1

(b) Beam 2

Figure 3.24 – Bunch intensities and lengths at the onset of the instability for Beam 1 (left) and Beam 2 (right) during the Fill 4538 (2015). The black line is the measured single-bunch threshold of loss of Landau damping defined by Eq. (3.6) and the dashed area is the uncertainty of the measured threshold.

limitation would be to apply controlled longitudinal emittance blowup during collisions to counteract the effect of synchrotron radiation damping and keep an approximately constant bunch length. The operational blowup used during the ramp can cause high particle losses at flat top. For that reason, the preferred method is to blow the beams up with rf phase modulation, described in Section 3.3.2. This method is almost loss-free since it acts mainly on the bunch center and changes the particle distribution inside the bunch without increasing the maximum bunch length.

3.5 Macroparticle simulations of loss of Landau damping

Macroparticle simulations using the BLonD code [37], introduced in Section 1.4.1, were carried out to validate the impedance model using measurements of the threshold of loss of Landau damping presented in previous sections of this chapter.

The number of macroparticles used in the simulations was 5×10^5. This was the number found from a careful convergence analysis where the number of macroparticles was increased until no difference in the results was observed.

Since the threshold of loss of Landau damping depends on the distribution, taken into account by the form factor F_m in Eq. (1.93), in simulations, the particle distribution in phase space has to be similar to the one in the LHC. Measured bunch profiles (see Section 2.3.1) were compared with different analytical distributions. A good fit was found using the binomial distribution defined as a function of the action J with exponent $n = 2$:

$$F(J) = F_o \left(1 - \frac{J}{J_o}\right)^n, \tag{3.7}$$

where F_o is a normalization coefficient and $J_o = \varepsilon/(2\pi)$, with ε being the full bunch emittance. For short bunches, the projection of this distribution onto the time coordinate gives a bunch profile in the form

$$\lambda(t) = \lambda_o \left[1 - \left(\frac{2t}{\tau}\right)^2\right]^{n+1/2}, \tag{3.8}$$

where λ_o is a normalization coefficient and τ is the full bunch length corresponding to the action J_o. A comparison of the measured bunch profiles with the proposed fit is shown in Fig. 3.25. The fit is good both at injection and top energies, except immediately after arrival to flat top for emittances above nominal when the particle distribution has been modified by the controlled emittance blowup. In that case, the distribution function is flatter at the bunch center. Nevertheless, this case is not relevant for our simulations, as those long bunches are far from the instability threshold.

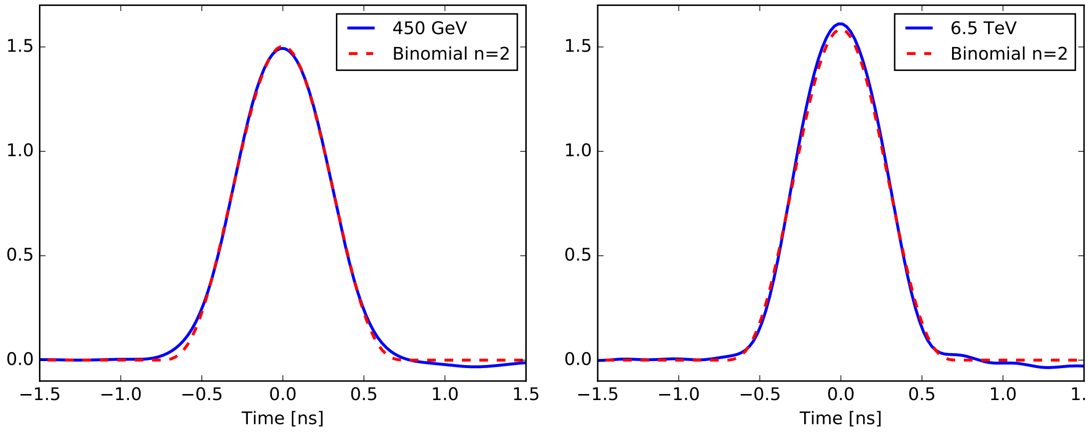

(a) 450 GeV

(b) 6.5 TeV

Figure 3.25 – Bunch profiles measured in the LHC at 450 GeV (left) and at 6.5 TeV (right), compared to a binomial profile with exponent $n = 2$ with the same FWHM (dashed red line).

In simulations, the bunch is populated by macroparticles using a random number generator, taking into account the particle distribution function defined above. In order to obtain a bunch that is matched to the bucket with intensity effects, the generation is done iteratively. First, the bunch is generated for zero intensity, and the profile is used to compute the induced voltage for the following step. Then, the intensity is being ramped up every step of the iteration. A few more iterations are done with the final intensity, until the distribution in phase space does not change significantly anymore. In general, about 10 iterations for ramping up the intensity and another 10 with constant intensity give converged results.

Once the bunch is generated and before the tracking starts, a 1 deg phase kick is applied to the bunch. This kick is small enough not to produce emittance blowup due to filamentation, but sufficiently large to excite a dipole motion to study the loss of Landau damping. The macroparticles are then tracked for 5×10^4 turns. This time corresponds to roughly 90 synchrotron periods at 6.5 TeV with 12 MV, 120 periods at 4 TeV with 12 MV, and 225 periods at 450 GeV with 5 MV. The simulated time has been proven to be long enough to observe whether the oscillations are damped or not.

The effect of the impedance is evaluated in the frequency domain, using the LHC impedance model described at the beginning of this chapter. The longitudinal profile is calculated in this step using 50 bins per bucket, which allows to compute the beam spectrum for frequencies up to 10 GHz. Then the beam spectrum is multiplied by the impedance, which is equivalent to the convolution in the time domain in Eq. (1.60), and the induced voltage (wake potential) is obtained by an inverse Fourier transform as defined by Eq. (1.64)

The threshold of loss of Landau damping was defined in simulations from the amplitude of the bunch phase oscillations. Our stability criterion is to consider that a bunch is stable when the average of the amplitude over the last 2×10^4 turns is smaller than 0.2 deg. This value was chosen taking into account that after the phase kick, the bunch filaments and the amplitude of the oscillations can be reduced, as shown in Fig. 3.26 for three bunches with different intensities.

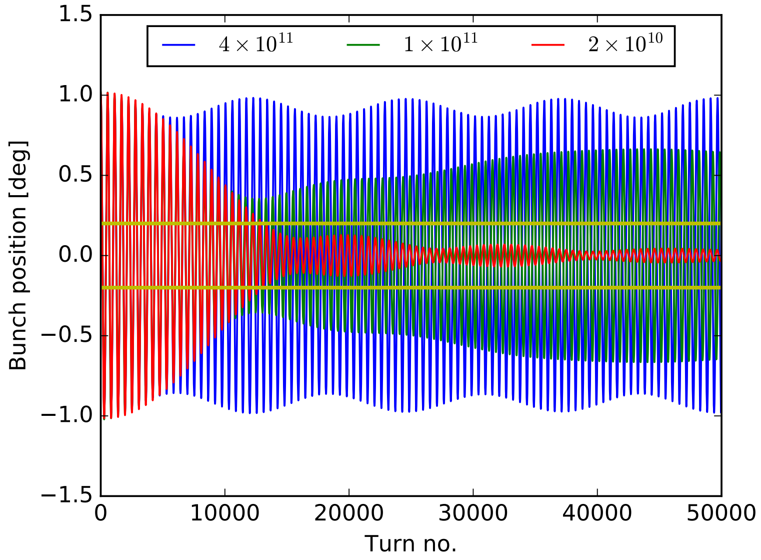

Figure 3.26 – Phase oscillations of bunches with $\varepsilon = 1$ eVs and three different intensities at 6.5 TeV with $V_{\text{rf}} = 12$ MV. The yellow line is the stability criterion, according to which only the bunch with an intensity of 2×10^{10} is stable. Note that the reduction of the oscillation amplitude during the first $\sim 1.5 \times 10^4$ turns is caused by filamentation after the phase kick.

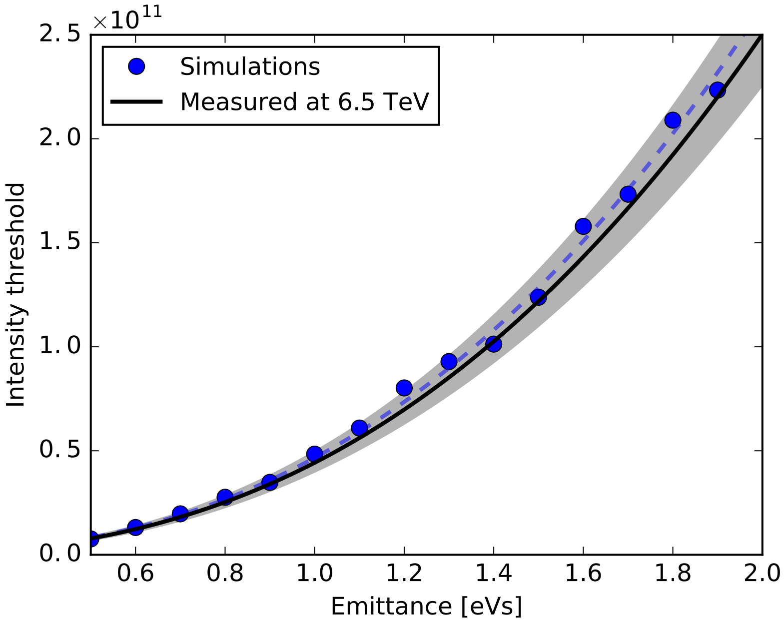

Figure 3.27 – Intensity thresholds of loss of Landau damping as a function of the emittance found from simulations (circles), and from measurements (solid line), for a bunch at 6.5 TeV with an rf voltage of 12 MV. The simulation data is fitted as $N_{th} \propto \varepsilon^{5/2}$ (dashed line), in agreement with the scaling of loss of Landau damping from Eq. (1.94). The measured threshold of loss of Landau damping defined by Eq. (3.6) agrees well with the results from simulations.

3.5.1 Simulation results and comparison with measurements

Figure 3.27 shows the intensity threshold for different longitudinal emittances found in simulations for a bunch with an rf voltage of 12 MV at 6.5 TeV. The dependence of the threshold on the longitudinal emittance is in good agreement with the expected scaling $N_{th} \propto \varepsilon^{5/2}$ from Eq. (1.94). The loss of Landau damping threshold measured at 6.5 TeV, defined by Eq. (3.6), is also in very good agreement with the results from simulations based on the current impedance model of the LHC.

Similar simulations were performed for other machine configurations to be able to compare them with the measurements done at 4 TeV and at 450 GeV. Results are shown in Fig. 3.28. In the two cases, both the scaling expected from loss of Landau damping and the threshold measured at 6.5 TeV (scaled in energy) are in good agreement with the simulations. For the case at 4 TeV, the threshold measured at 4 TeV is also shown for comparison, and agrees with the simulations as well, although the uncertainty of that threshold is much larger. The threshold measured at 450 GeV, however, has some deviation, probably due to the reduced number of bunches and the uncertainties in measurements of bunch length and intensity that were neglected.

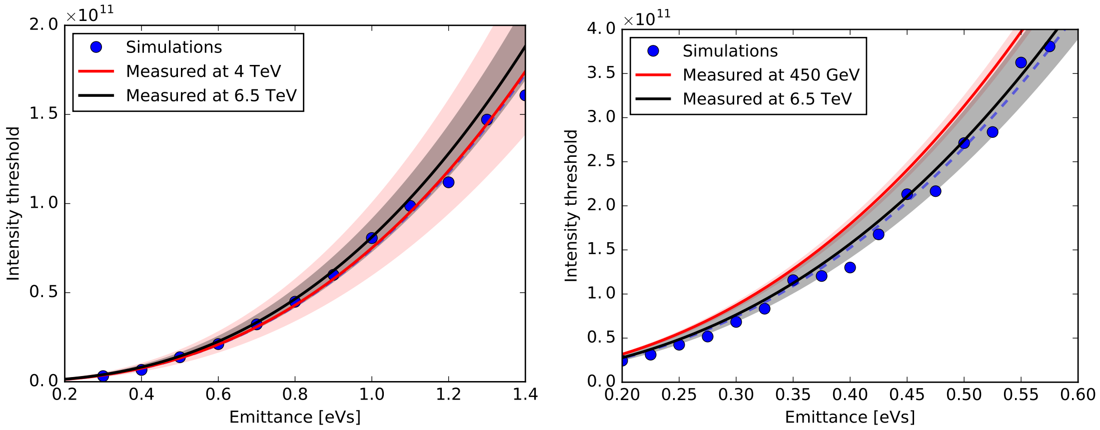

(a) 4 TeV

(b) 450 GeV

Figure 3.28 – Intensity thresholds of loss of Landau damping as a function of the emittance found from simulations (circles), for a bunch at 4 TeV with an rf voltage of 12 MV (left) and for a bunch at 450 GeV with an rf voltage of 5 MV (right). The data is fitted as $N_{th} \propto \varepsilon^{5/2}$ (dashed line), in agreement with the scaling of loss of Landau damping from Eq. (1.94). The measured threshold of loss of Landau damping at 6.5 TeV (black line), defined by Eq. (3.6), agree well with the results from simulations. Measurements done at 4 TeV (left, red line) also agree with the simulated threshold at the same energy, but some deviation is seen for the measurements done at 450 GeV (right, red line).

3.6 Conclusions

Beam-measurements of the LHC impedance using the traditional methods are challenging due to the very low impedance of the LHC. Bunch phase measurements were used for estimation of the resistive impedance, although their systematic errors are larger than the required accuracy. Nevertheless, relative measurements of the resistive impedance of the TDI movable jaws are in good agreement with bench-measurements.

The expected synchrotron frequency shift from potential-well distortion is also smaller than the resolution of the peak-detected Schottky spectrum [56]. A better resolution than in the peak-detected Schottky spectrum is achieved using a method based on exciting the beam with a sinusoidal rf phase modulation. Results using this technique are consistent with analytical estimations using the LHC impedance model.

The reactive impedance was also estimated from the loss of Landau damping threshold [24] and this approach is so far the most sensitive method. The stability thresholds observed during the ramp follow the analytical scaling of loss of Landau damping and measurements at flat top for different energies are in good agreement with analytical calculations and macroparticle simulations performed using the tracking code BLonD [37]. A similar simulation method will be used in the next Chapter to study the operation of the LHC with higher intensity beams.

4 Future LHC operation with higher intensity beams

In this chapter, we present estimations of the stability thresholds for HL-LHC beams based on the knowledge obtained in Chapter 3 on the LHC impedance and beam stability. Macroparticle simulations were carried out using an updated LHC impedance model that includes new machine elements. Operation with an additional rf system and its impact on beam stability is also considered.

4.1 The HL-LHC impedance model

The HL-LHC impedance model [86] is being developed using the LHC impedance model as a base. It includes the contributions of the new elements that will be installed in the HL-LHC and those which will be upgraded. Figure 4.1 shows the current state of the impedance model.

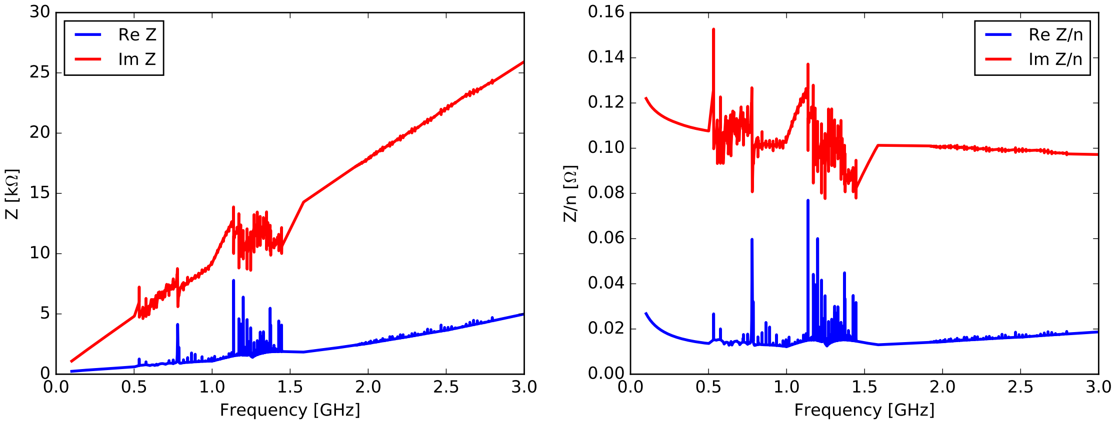

(a) Real and imaginary part of Z

(b) Real and imaginary part of Z/n

Figure 4.1 – Real (blue line) and imaginary (red line) part of the HL-LHC impedance model [86], in natural scale (left) and divided by $n = \omega/\omega_o$ (right).

One of the largest new contributions to the HL-LHC impedance is from the crab cavities [87]. These cavities are designed to deflect the beam transversely in order to compensate for the geometric luminosity-reduction factor. There are still two different designs being considered: the so-called "double quarter-wave resonator" (DQWR) and the "rf dipole" (RFD) cavities. For the study of loss of Landau damping for a single bunch the parameter of interest is $\mathrm{Im}Z/n$, which is similar for both types of cavities. The impedance model includes a purely inductive impedance of $\mathrm{Im}Z/n = 25$ mΩ that accounts for the effective impedance of the 16 crab cavities.

Other elements taken into consideration are the resistive-wall impedance of the new triplets beam screens, the higher-order modes (HOM) of the new experimental chambers, and the wire compensator for long-range beam-beam effects [88].

Besides the new contributions, certain existing collimators will be replaced by Molybdenum-coated collimators [89, 90], leading to a reduction of the total impedance by about 10%.

Compared to the LHC impedance model used in the previous chapter, the additional elements and upgrades of the existing elements result in an increase of ~20% in the effective reactive impedance $\mathrm{Im}Z/n$, becoming in this case about 0.11 Ω for 1 ns bunches.

4.2 HL-LHC machine and beam parameters

The HL-LHC machine parameters are practically the same as those of the LHC, with some small differences. For example, the optics will be slightly changed and that leads to a change in gamma transition, with the new value being $\gamma_{\mathrm{tr}} = 53.8$. Regarding the beam parameters, the most important change for beam stability is the increase of the bunch intensity up to 2.2×10^{11}, about a factor 2 higher than the LHC nominal intensity. A complete list of beam and machine parameters of the HL-LHC can be found in Refs. [4] and [91].

The rf voltage at injection energy (450 GeV) will be increased to 8 MV to cope with the larger longitudinal emittances expected from the SPS (0.7 eVs) [91] and the higher rf voltage at the SPS extraction (10 MV instead of 7 MV) [5]. Assuming up to 10% beam losses during the injection plateau, acceleration, and squeeze, a bunch intensity of about 2.4×10^{11} could be required at injection.

At top energy (7 TeV), the nominal longitudinal emittance is 2.5 eVs, corresponding to a bunch length of 1.08 ns in an rf voltage of 16 MV.

4.3 Longitudinal single-bunch stability

In order to define the single-bunch stability limits in the HL-LHC, macroparticle simulations of loss of Landau damping were carried out using the calculated HL-LHC impedance model described above. The same simulation settings were used as in the previous chapter (5×10^5 macroparticles, 5×10^4 turns, and 50 bins per bucket), as well as the same particle distribution function, see Eq. (3.7).

The intensity threshold at 450 GeV as a function of the longitudinal emittance determined from simulations is shown in Fig. 4.2a. For the expected emittance at injection, which corresponds to a bunch length of 1.4 ns, the intensity threshold at 450 GeV is 4.4×10^{11}, well above the required bunch intensity.

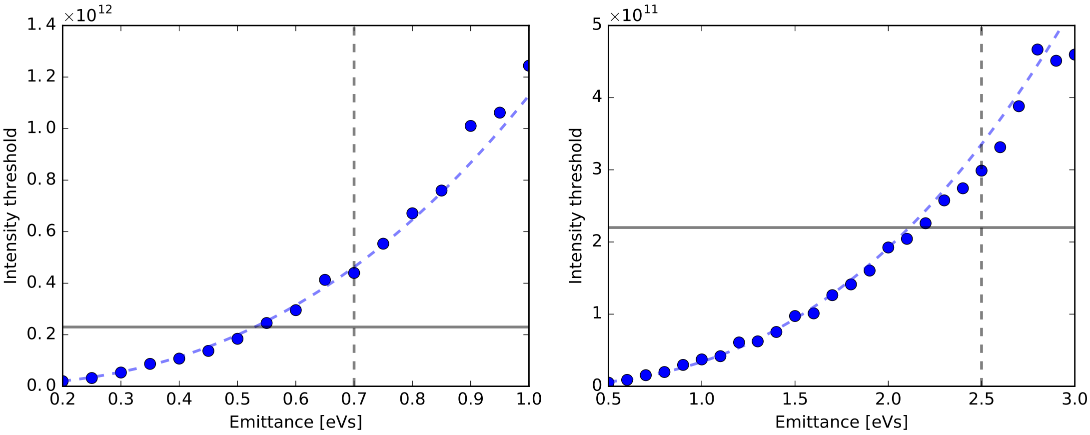

(a) 450 GeV

(b) 7 TeV

Figure 4.2 – Intensity threshold of loss of Landau damping as a function of the longitudinal emittance determined from macroparticle simulations (circles) for a single bunch at 450 GeV with V_{rf} = 8 MV (left) and at 7 TeV with V_{rf} = 16 MV (right), together with a fit $N_{th} \propto \varepsilon^{5/2}$ (dashed blue line), according to the scaling of loss of Landau damping (1.94). In both cases, the HL-LHC nominal bunch intensity (solid black line) is stable for the HL-LHC nominal emittance (dashed black line).

Results of a similar analysis done at 7 TeV with 16 MV are shown in Fig. 4.2b. The intensity threshold is found to be 3.0×10^{11} for the HL-LHC nominal emittance of 2.5 eVs, corresponding to a bunch length of 1.08 ns. Although the stability margin seems to be reasonably large, it is smaller than the factor two safety margin considered in previous studies [92]. It is important to keep in mind that the margin could be reduced if the impedance is increased by installing additional elements or in case that the calculated impedance of the new elements is underestimated.

For multi-bunch beams, a ∼15% spread in bunch length is typically observed in the LHC at arrival to the flat top. In that case, if the average bunch length is the nominal one, the shorter bunches would have a longitudinal emittance of about 2.1 eVs and therefore they would be at the limit of stability. A similar issue may arise at injection energy from the spread in bunch length of the beam extracted from the SPS.

A good agreement is observed between the thresholds determined from simulations at both energies and the scaling of loss of Landau damping (1.94), with the dependence of the intensity threshold N_{th} on the longitudinal emittance ε following the scaling law:

$$N_{\mathrm{th}} \propto \varepsilon^{5/2}. \tag{4.1}$$

Alternatively, the impedance threshold can be estimated analytically using Eq. (1.93). For the HL-LHC nominal parameters, the impedance threshold found using a form factor $F = 1$ is $(\mathrm{Im}Z/n)_{\mathrm{th}} = 0.15\ \Omega$ at injection energy and $(\mathrm{Im}Z/n)_{\mathrm{th}} = 0.1\ \Omega$ at flat top. However, these results are rather pessimistic compared to simulation results. Different form factors should be used in order to match the values obtained above from simulations, and they were found to be $F = 1.3$ at 450 GeV and $F = 1.5$ at 7 TeV.

4.4 Coupled-bunch stability

Analytical estimations of the coupled-bunch stability threshold in the HL-LHC were done, but assuming the accelerator is completely filled with bunches evenly spaced [93]. This assumption may result in a pessimistic estimation of the stability threshold. The complexity increases if the real filling pattern is taken into account, which includes trains with different number of bunches and spacing between bunches, as well as a ~3 μs abort gap. Additionally, macroparticle simulations are not feasible as the computational power required to perform them for the multi-bunch case largely exceeds the available computing resources, given the large number of bunches that can be injected into the HL-LHC (up to 2748).

As already mentioned in the previous chapter, no coupled-bunch instability has been observed in the LHC so far. However, the beam current in the HL-LHC will be approximately doubled and the impedance will be increased by the installation of new elements. In particular, the high-order modes of the crab cavities could be a potential issue.

Two different options have been considered to deal with unexpected coupled-bunch instabilities. One possibility is to install a longitudinal damper that could act against coherent oscillations, but the requirements of the system are too exigent [92]. In addition, experience with other types of active damping systems (as the LHC ADT) has shown that the systems need to be fine-tuned after any change of the beam parameters for optimum performance. Instead, a high-harmonic rf system [94] would be a less complex system that can considerably increase the stability threshold by providing a larger spread in synchrotron frequencies. The additional spread in synchrotron frequencies also increases the single-bunch and microwave stability margin, and being a passive system the setting up and operation is simpler than for an active damper. In addition, the frequency spread can also be beneficial for the controlled longitudinal emittance blowup, which was found to fail for bunches shorter than in normal operation (~0.8 ns) with small spread in synchrotron frequencies [95]. These advantages make the high-harmonic rf system an interesting option for HL-LHC.

4.5 Electron-cloud effect

The electron-cloud effect is considered to be another potential performance limitation for HL-LHC beams with 25 ns bunch spacing. Scrubbing with beams is the proposed mitigation method to reduce the SEY of the beam screens [96]. A reduction of the SEY below 1.3 – 1.4

is required to keep the e-cloud induced heat load lower than the cooling capacity of the cryogenic system [97]. However, it is not known yet if this scenario is feasible.

There are several backup scenarios in case the SEY reduction achieved by scrubbing is not sufficient. One of them is the use of beams with a spacing of 50 ns, which requires an increase of the bunch intensity to about 3.1×10^{11} in order not to lose luminosity. An alternative filling scheme with 25 ns bunch spacing where 8 bunches are followed by 4 empty slots (8b4e) [98] has also been tested as a valid option to significantly reduce the e-cloud effect, requiring to increase the bunch intensity to 2.7×10^{11} to compensate for the reduced number of bunches. According to the stability threshold calculated above, in both cases the stability margin is reduced and the beam could suffer from beam instabilities. An 800 MHz high-harmonic rf system could be used to increase the stability margin for these alternative schemes.

Given the dependence of the e-cloud on bunch length [99], another fallback scheme is to use longer bunches (~2 ns) in a 200 MHz rf system to reduce the e-cloud effect in the dipoles. The beam dynamics considerations of these options are described in a later section of this chapter.

4.6 Double rf operation

As operation with two rf systems is considered an interesting option to increase the stability margin in the HL-LHC, here we describe some beam dynamics aspects of operation in a double rf system and the effect on beam stability.

In an accelerator operated with two rf systems, the total external voltage V_{rf} seen by the particles can be expressed as

$$V_{\mathrm{rf}}(\phi) = V_1 \sin\phi + V_2 \sin\left[n\left(\phi + \Phi_2\right)\right], \tag{4.2}$$

where V_1 is the voltage of the main rf system, $V_2 = r\,V_1$ is the voltage of the second rf system, r is the voltage ratio between the two rf systems, $n = h_2/h_1$ is the ratio between the harmonic numbers of both rf systems, and Φ_2 is the phase shift between the two rf systems (at the main frequency).

The additional nonlinearity introduced by the high-harmonic rf system produces changes on the rf bucket and on the synchrotron frequency distribution that strongly depend on the phase shift between the two rf systems Φ_2. The two modes of operation that are most frequently used are called bunch-lengthening mode (BLM), with the two rf systems in counterphase:

$$n\,\Phi_2 = (1-n)\,\phi_s + \pi, \tag{4.3}$$

and bunch-shortening mode (BSM), with the two rf systems in phase:

$$n\,\Phi_2 = (1-n)\,\phi_s. \tag{4.4}$$

The names of the operation modes are explained by the fact that for a given longitudinal emittance, in BLM bunches become longer and flatter, and in BSM bunches are shorter with a higher peak line density, as represented in Fig. 4.3. However, this effect is only apparent for low harmonic ratios n.

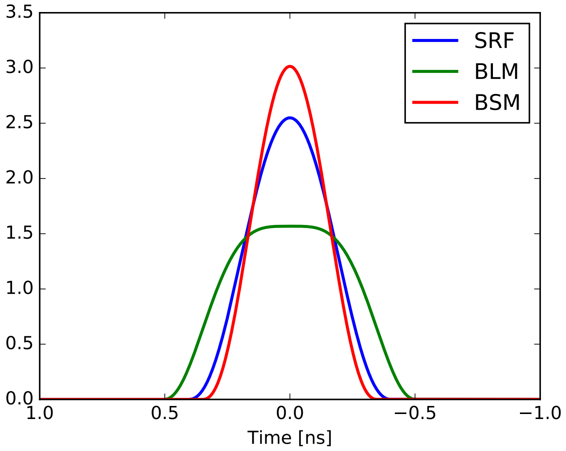

Figure 4.3 – Example of the bunch profile for different modes of operation in a double rf system: single rf (SRF, blue), bunch-lengthening mode (BLM, green), and bunch-shortening mode (BSM, red). The main rf system is at 400 MHz, with 16 MV, and the second harmonic has a voltage of 8 MV.

4.6.1 Potential well in a double rf system

The potential well in a double rf system can be calculated using Eq. (1.30) and it can be expressed as

$$\begin{aligned} U(\phi) &= V_1\left[\cos\phi - \cos\phi_s + (\phi-\phi_s)\sin\phi_s\right] + \\ &+ \frac{V_2}{n}\left[\cos(n\phi + n\Phi_2) - \cos(n\phi_s + n\Phi_2) + (\phi-\phi_s)\sin(n\phi_s + n\Phi_2)\right] \end{aligned} \tag{4.5}$$

In BSM, using Eq. (4.3), a Taylor expansion of the potential well about ϕ_s gives the expression for small amplitudes of oscillation $\Delta\phi = \phi - \phi_s \approx 0$:

$$U(\Delta\phi) \simeq V_1\left(\frac{1}{2} + \frac{r\,n}{2}\right)\Delta\phi^2, \tag{4.6}$$

which has a similar dependence on $\Delta\phi$ as in the single rf case ($r = 0$).

In BLM, the coefficient of the term $\Delta\phi^2$ can become close to 0 for $r \approx 1/n$, and the following term of the Taylor expansion is needed. In this case, the expansion of the potential well about ϕ_s can be written as

$$U(\Delta\phi) \simeq V_1\left(\frac{1}{2} - \frac{r\,n}{2}\right)\Delta\phi^2 + V_1\left(\frac{1}{24} + \frac{r\,n^3}{24}\right)\Delta\phi^4. \tag{4.7}$$

4.6.2 Synchrotron frequency distribution in a double rf system

The synchrotron frequency for zero-amplitude oscillations in a double rf system can be found similarly as it was done for a single rf in Section 1.1.3. In this case, we substitute the rf voltage in Eq. (1.23) by the total rf voltage defined by Eq. (4.2):

$$\frac{d^2\phi}{dt^2} - \frac{h\,\omega_o^2\,q\,\eta}{2\pi\,\beta^2\,E_o}\left[V_{\mathrm{rf}}(\phi) - V_{\mathrm{rf}}(\phi_s)\right] = 0. \tag{4.8}$$

A Taylor expansion of Eq. (4.8) about ϕ_s is given by

$$\frac{d^2\Delta\phi}{dt^2} + \frac{\omega_{so}^2}{V_1\,\cos\phi_s}\left[V_1\,\cos\phi_s - V_2\,n\,\cos(n\phi_s + n\Phi_2)\right]\Delta\phi = 0, \tag{4.9}$$

where it was introduced the synchrotron frequency of the single rf case ω_{so} defined by Eq. (1.25). Finally, the zero-amplitude synchrotron frequency in a double rf system $\omega_{so}^{\mathrm{DRF}}$ can be expressed as:

$$\omega_{so}^{\mathrm{DRF}} = \omega_{so}\sqrt{1 + r\,n\,\frac{\cos\left(n\phi_s + n\Phi_2\right)}{\cos\phi_s}}. \tag{4.10}$$

The synchrotron frequency distribution in a double rf system, calculated using Eq. (1.49), is plotted in Fig. 4.4 for several harmonic ratios n, a voltage ration $r = 1/n$, and for both modes of operation. The higher the harmonic ratio, the larger is the synchrotron frequency spread. However, in BLM, as well as in BSM for $n > 2$, there is a region with $\omega_s'(J) \simeq 0$ where Landau damping is lost [100, 101, 102], and that poses a limit for the maximum longitudinal emittance.

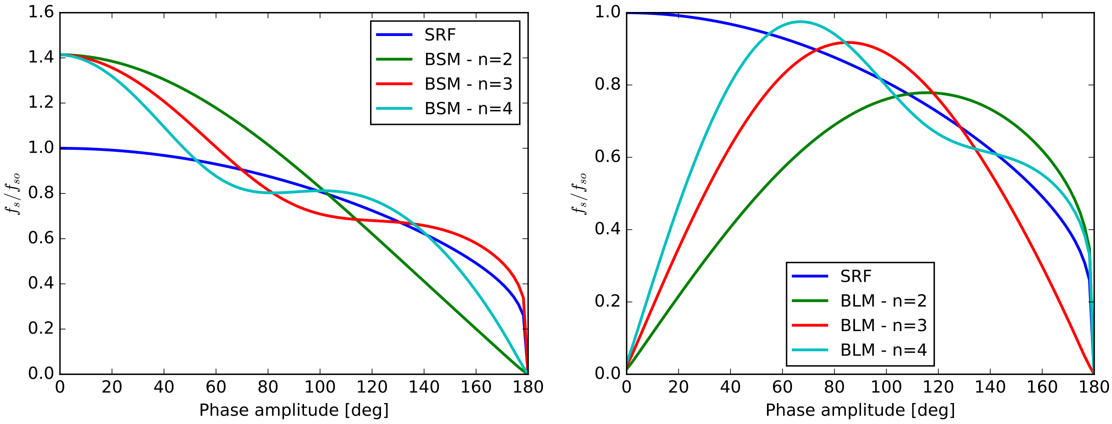

(a) BSM (b) BLM

Figure 4.4 – Synchrotron frequency distribution for different harmonic ratios n and for $r = 1/n$, in BSM (left) and BLM (right). Note that for higher harmonics a region with $\omega_s'(J) \simeq 0$ moves closer to the bucket center.

It is common to use a voltage ratio $r = 1/n$, which is interesting because it provides a large spread in synchrotron frequencies that is beneficial for Landau damping. For lower voltage ratios, the frequency spread is reduced, and for higher voltage ratios, the beam dynamics starts to be dominated by the high-harmonic rf system.

For HL-LHC, a harmonic ratio $n = 2$ is being considered. Although the required voltage is higher than for a higher harmonic, it provides enough synchrotron frequency spread. Also, the region with $\omega_s'(J) \simeq 0$ is only present in BLM and it is farther from the bucket center than in the cases for higher n. Therefore, it offers a large limit for the maximum stable longitudinal emittance in both operation modes (BSM and BLM).

4.6.3 Loss of Landau damping scaling in a double rf system

The analytical scaling of loss of Landau damping, presented in Section 1.2.3, was derived for a single rf system and can be different in a double rf system. It also depends on the mode of operation of the high-harmonic rf system. The dependence of the intensity threshold on the longitudinal emittance for constant energy can be found from Eq. (1.93).

In BSM, the potential well for particles with small synchrotron oscillations derived in Eq. (4.6) is $U(\Delta\phi) \propto \Delta\phi^2$, as in a single rf, and therefore the same relations are still valid:

$$\tau \propto \varepsilon^{1/2}, \quad \frac{\Delta E}{E} \propto \varepsilon^{1/2}, \text{and} \quad \frac{\Delta\omega_s}{\omega_s} \propto \varepsilon, \tag{4.11}$$

with the same scaling as for single rf:

$$N_{\text{th}} \propto \varepsilon^{5/2}. \tag{4.12}$$

In BLM, the potential well for small oscillations is $U(\Delta\phi) \propto \Delta\phi^4$ for a voltage ratio $r \approx 1/n$, and the following relations [8] are used:

$$\tau \propto \varepsilon^{1/3}, \quad \frac{\Delta E}{E} \propto \varepsilon^{2/3}, \text{and} \quad \frac{\Delta\omega_s}{\omega_s} \propto \varepsilon^{1/3}. \tag{4.13}$$

The scaling is found to be

$$N_{\text{th}} \propto \varepsilon^2. \tag{4.14}$$

For sufficiently small voltage ratios, $r \ll 11/\left(12\,n + n^3\right)$, the potential well in BLM becomes proportional to $\Delta\phi^2$ and the same scaling as in BSM and single rf can be applied.

These scalings of loss of Landau damping for BSM and BLM are compared with results of macroparticle simulations in the following sections of this chapter.

4.7 Power requirements for the HL-LHC main rf system

In the HL-LHC, as in most accelerators of high-intensity beams, the voltage induced in the cavities by the beam is responsible for a change in the amplitude and phase of the rf voltage (beam loading). Feedbacks are usually used to counteract the beam loading effect and keep the rf voltage amplitude and phase according to the design values. Depending on the method used for beam-loading compensation, the operation of the harmonic rf system can be affected.

In order to keep the rf voltage constant and a uniform bunch spacing, the required klystron power during the time intervals with beam P_b and without beam $P_{\overline{b}}$ can be expressed for the stationary case (no acceleration) above transition ($\phi_s = \pi$) as [103]

$$P_b = \frac{1}{8}\frac{V_{\text{cav}}^2}{Q_L R/Q} + \frac{1}{2} Q_L R/Q \left(\frac{V_{\text{cav}}}{R/Q}\frac{\Delta f}{f} + \frac{I_{\text{rf,pk}}}{2}\right)^2, \tag{4.15}$$

$$P_{\overline{b}} = \frac{1}{8}\frac{V_{\text{cav}}^2}{Q_L R/Q} + \frac{1}{2} Q_L R/Q \left(\frac{V_{\text{cav}}}{R/Q}\frac{\Delta f}{f}\right)^2, \tag{4.16}$$

where V_{cav} is the rf voltage in a cavity, Q_L is the loaded quality factor of the cavity, R/Q is the normalized shunt impedance of the rf cavity, $\Delta f/f$ is the relative cavity detuning, and $I_{\text{rf,pk}}$ is the peak beam current component at the rf frequency, which can be calculated as

$$I_{\text{rf,pk}} = 2 f_b N_b q \frac{1}{T_b}, \tag{4.17}$$

where N_b is the number of particles per bunch, q is the charge of a particle, T_b is the bunch spacing, and f_b is the bunch form factor calculated as the normalized amplitude of the beam spectrum at the main rf frequency (between 0 and 1). In the following, we will assume Gaussian bunches with a form factor f_b defined as a function of the 4-σ bunch length $\tau_{4\sigma}$ by

$$f_b(\tau_{4\sigma}) = e^{-\frac{\left(\pi \tau_{4\sigma} f_{\text{rf}}\right)^2}{8}}. \tag{4.18}$$

From Eqs. (4.15) and (4.16), the so-called half-detuning scheme can be defined for a value of the cavity detuning $\left(\Delta f/f\right)_{\text{HD}}$ such that the klystron power is kept constant over the periods with and without beam ($P_b = P_{\overline{b}}$). In this case, the detuning is found to be

$$\left(\frac{\Delta f}{f}\right)_{\text{HD}} = -\frac{1}{4} R/Q \frac{I_{\text{rf,pk}}}{V_{\text{cav}}}. \tag{4.19}$$

The value of the loaded Q_L can be optimized to minimize the rf power from Eqs. (4.15) and (4.16). Figure 4.5 shows the power requirements of the LHC cavities for different values of the loaded Q_L for the operational parameters at 6.5 TeV used in 2015. It can be seen that for a $Q_L \approx 6 \times 10^4$, the required power is about 200 kW, which is below the rf power available in the LHC (300 kW per klystron).

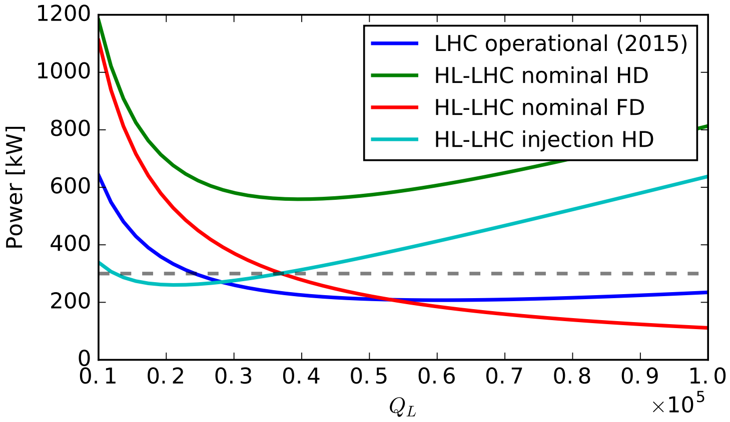

Figure 4.5 – Required rf power as a function of the loaded Q_L for the operational LHC parameters at 6.5 TeV (blue line, $N_b = 1.15 \times 10^{11}$, $\tau = 1.2$ ns, $V_{\text{cav}} = 1.5$ MV), for the nominal HL-LHC parameters at 7 TeV ($N_b = 2.2 \times 10^{11}$, $\tau = 1.08$ ns, $V_{\text{cav}} = 2$ MV) for operation in half detuning (green line) and in full detuning (red line), and for HL-LHC parameters at injection energy (cyan line, $N_b = 2.4 \times 10^{11}$, $\tau = 1.4$ ns, $V_{\text{cav}} = 1$ MV). The dashed line is the 300 kW power limitation of the LHC klystrons.

However, the rf power requirements for the HL-LHC beam current at 7 TeV, shown also in Fig. 4.5, largely exceed the available rf power. For the optimal loaded $Q_L \approx 4 \times 10^4$, the rf power in half-detuning scheme is around 600 kW per klystron.

An alternative scheme has been proposed for HL-LHC to cope with this power limitation [103], known as full-detuning scheme. In this mode of operation, the rf voltage amplitude is kept at the design value but the rf phase is allowed to slip for each bunch with respect to the design phase. This method allows to further reduce the required rf power and make it almost independent of the beam current.

The cavity detuning $\left(\Delta f / f\right)_{\text{FD}}$ needed for operation in full detuning is

$$\left(\frac{\Delta f}{f}\right)_{\text{FD}} = -\frac{1}{2} R/Q \frac{I_{\text{rf,avg}}}{V_{\text{cav}}} = -R/Q \frac{f_b I_{\text{DC}}}{V_{\text{cav}}}, \tag{4.20}$$

where $I_{\text{rf,avg}}$ is the average beam current component at the rf frequency and I_{DC} is the DC beam current.

The required rf power P_{FD} is

$$P_{\text{FD}} = \frac{1}{8} \frac{V_{\text{cav}}^2}{Q_L R/Q}. \tag{4.21}$$

For the nominal HL-LHC beam and rf parameters, Fig. 4.5 shows the rf power requirements calculated using Eq. (4.21). For a loaded $Q_L = 6 \times 10^4$, which is currently used in the LHC at top energy, we get that power requirement is of about 185 kW per klystron, independently of the beam current.

An algorithm to continuously adjust the cavity phase according to the beam current has been proposed [104] and it was successfully tested in the LHC in 2012 [105].

At injection energy, operation in half detuning is preferable, since it provides a uniform bunch spacing that eases the injection process from the SPS. In this case, the klystron power required is about 260 kW (see Fig. 4.5), which is below the power limit.

4.8 Operation with an extra 800 MHz rf system

A design based on a scaled version of the 400 MHz cavities (see Fig. 4.6) has been developed to be used as an 800 MHz high-harmonic rf system for HL-LHC [106]. The impedance of these cavities is $R/Q = 45\ \Omega$ at their operating frequency and are equipped with a power coupler capable of delivering 300 kW.

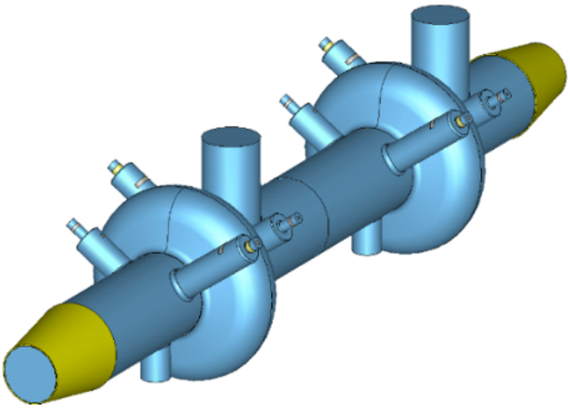

Figure 4.6 – Model of two 800 MHz rf cavities for HL-LHC [106].

The power requirements for these cavities are very different for each mode of operation when the main harmonic rf system (400 MHz) is operated in full-detuning scheme [107]. In BSM, the required power is reduced compared to the requirement for half-detuning scheme, and 4 cavities providing 2 MV each would be enough with 120 kW per klystron. In BLM, on the contrary, the power requirements are increased. For an operating rf voltage of 1 MV, the required power is about 300 kW per klystron and a minimum of 8 cavities would be needed. Some extra cavities may be required to increase the operational margin to allow for regulation of the beam loading compensation, and to achieve the necessary phasing between the two rf systems.

The longitudinal single-bunch stability at 7 TeV is studied below for the different operation modes of the double rf system. Then the effect of an additional phase shift (error) between the two rf systems is also analyzed. Other options with a lower voltage of the second harmonic rf system and with lower voltages of both rf systems are also considered.

4.8.1 Longitudinal single-bunch stability at 7 TeV

The intensity thresholds at 7 TeV were found for both modes of operation using macroparticle simulations, and they are compared to the single rf case in Fig. 4.7. For BLM, as the average synchrotron frequency is lower, the simulations had to be run for 1×10^5 turns. For the HL-LHC nominal bunch length of 1.08 ns, the emittance in BSM is 3 eVs and it gives an increase of the intensity threshold to 1.1×10^{12}. In BLM, the same bunch length is obtained for an emittance of 1.8 eVs, and the intensity threshold is about two times higher than in BSM, being in this case 2.14×10^{12}.

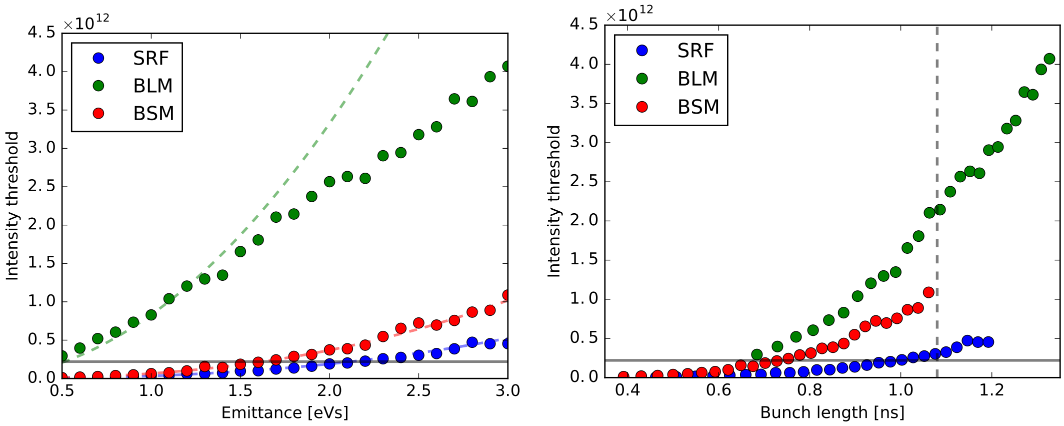

(a) Intensity thresholds vs emittance

(b) Intensity thresholds vs bunch length

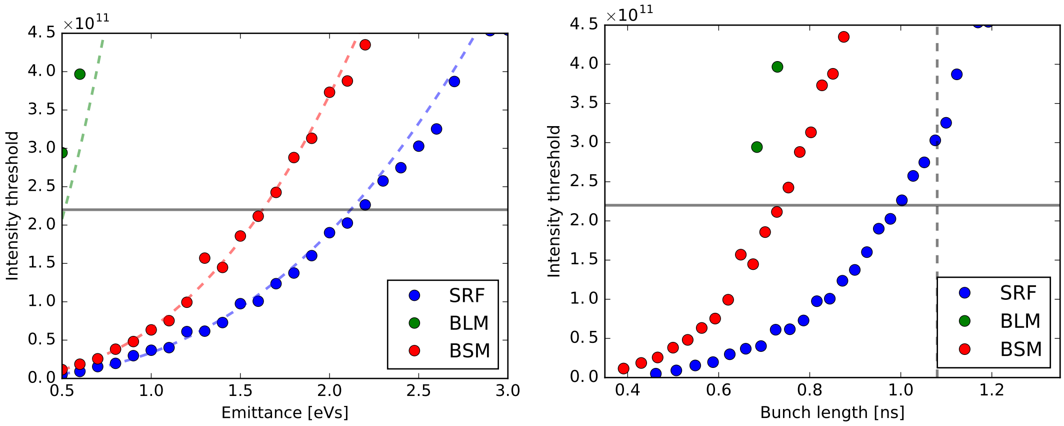

(c) Intensity thresholds vs emittance (zoom)

(d) Intensity thresholds vs bunch length (zoom)

Figure 4.7 – Intensity threshold as a function of the longitudinal emittance (left) and bunch length (right) at 7 TeV, for a 400 MHz system operating at 16 MV as a single rf (blue), and with an 800 MHz rf system operating at 8 MV in BLM (green) and in BSM (red). Note that although a very large gain is observed for BLM for a given emittance, it is reduced if compared in terms of bunch length. The data is fitted according to the analytical scaling of loss of Landau damping for the different operation modes (dashed colored lines), described in Section 4.6.3. The HL-LHC nominal bunch intensity is shown for reference (horizontal line), as well as the HL-LHC nominal bunch length (right plots, vertical dashed line). Bottom plots, zoom of top plots on intensity range around the HL-LHC nominal intensity.

A very good agreement is observed for the scaling of loss of Landau damping (4.12) calculated in Section 4.6.3 for BSM. However, for BLM the discrepancy is quite big for emittances higher than about 1.5 eVs. The reason could be that, close to the instability threshold, the bunch intensity is rather high and therefore so is the induced voltage. The high induced voltage distorts significantly the potential well, the synchrotron frequency spread is reduced, and the stability threshold is finally lower than expected. Figure 4.8 shows an example of how the synchrotron frequency distribution changes in BLM when the intensity effects are taken into account.

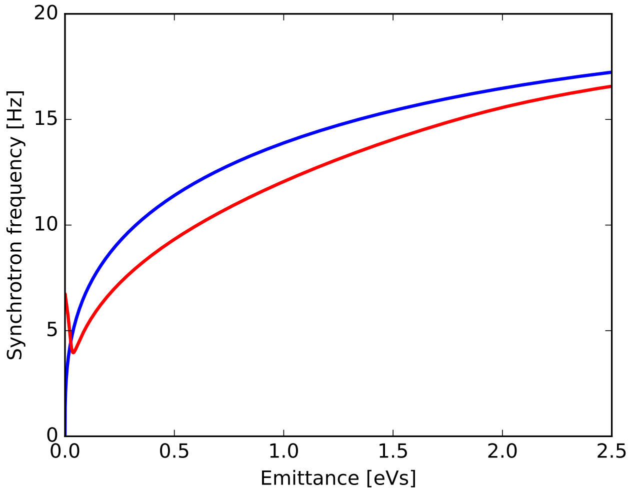

Figure 4.8 – Synchrotron frequency distribution as a function of the single-particle longitudinal emittance $\varepsilon = 2\pi J$, without intensity effects (blue) and for a bunch of 2 eVs with an intensity of 2.0×10^{12} (red). Calculated for a main rf system at 400 MHz and 16 MV, a high-harmonic system at 800 MHz with 8 MV operated in BLM. The bunch has a binomial distribution, defined by Eq. (3.7), with $n = 2$.

4.8.2 Effect of a phase shift between the two rf systems on beam stability

The phase swing allowed by the full-detuning scheme can pose a challenge in case it is used in combination with a high-harmonic rf system, as it would require a very accurate phase synchronization between both rf systems. The situation becomes crucial for operation in BLM, as the rf power required for the phase alignment is greatly increased [108]. In addition, this mode of operation is particularly sensitive to a phase shift between the two rf systems. Figures 4.9 shows how the profile is modified for different phase shifts in BLM and BSM, which implies also a change in the beam spectrum. The synchrotron frequency distribution is also considerably distorted, as shown in Fig. 4.10, which has consequences on beam stability.

The phase variation introduced in the full-detuning scheme corresponds to a maximum shift in the bucket centers along the bunch trains of about 85 ps [108]. At 400 MHz, this is equivalent to a phase shift of 12.5 deg.

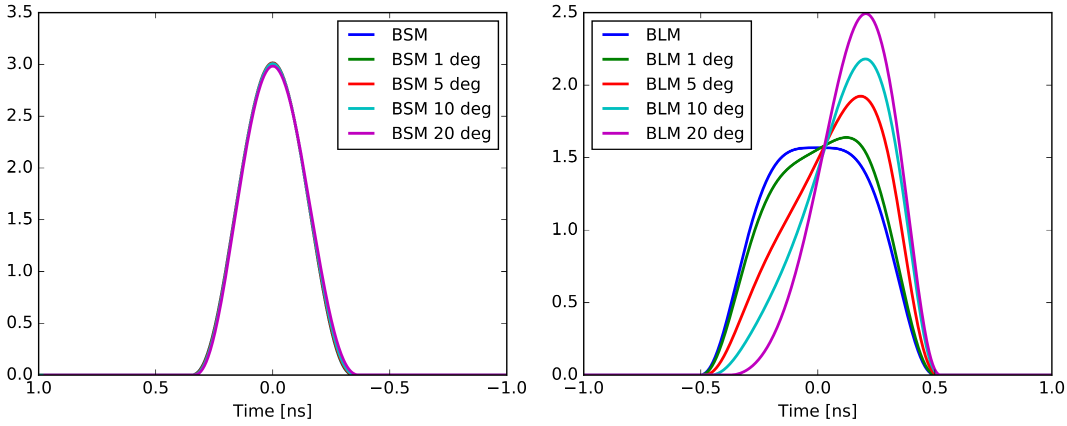

(a) BSM

(b) BLM

Figure 4.9 – Bunch profile distortion for different phase shift Φ_2 between the two rf systems, in BSM (left) and in BLM (right), for a voltage ratio $r = 1/2$. Note the small effect on the bunch shape for BSM and the significant change of the bunch profile in BLM, even for small phase shifts.

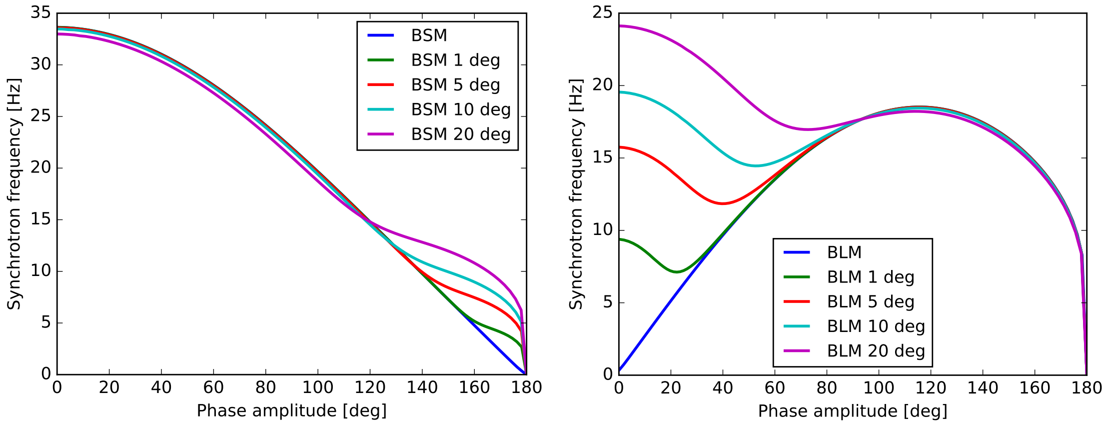

(a) BSM

(b) BLM

Figure 4.10 – Synchrotron frequency distribution in BSM (left) and in BLM (right) for different phase shift Φ_2 between the two rf systems and for a voltage ratio $r = 1/2$. Note the small effect on the outer part of the bucket (usually not filled) for BSM and the significant change of the distribution for small amplitude oscillations in BLM, where the bunch lays, even for small phase shifts.

The effect of a phase shift between the two rf systems on beam stability was also analyzed in simulations. Figure 4.11 shows the results for phase shifts of $\pm 1, \pm 5, \pm 10$, and ± 20 deg, for the two modes of operation (BSM and BLM). As expected, no apparent effect is seen in BSM, even for phase shifts of ±20 deg. In BLM, the effect is more dramatic, with a reduction in the stability threshold of up to a factor 5 for the emittance of interest (~1.8 eVs), bringing the intensity threshold lower than that in BSM.

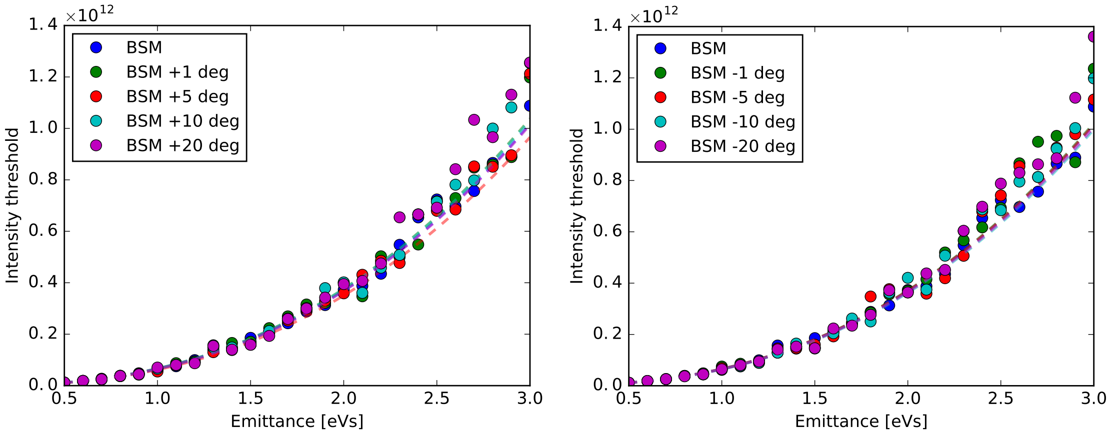

(a) BSM positive shift (b) BSM negative shift

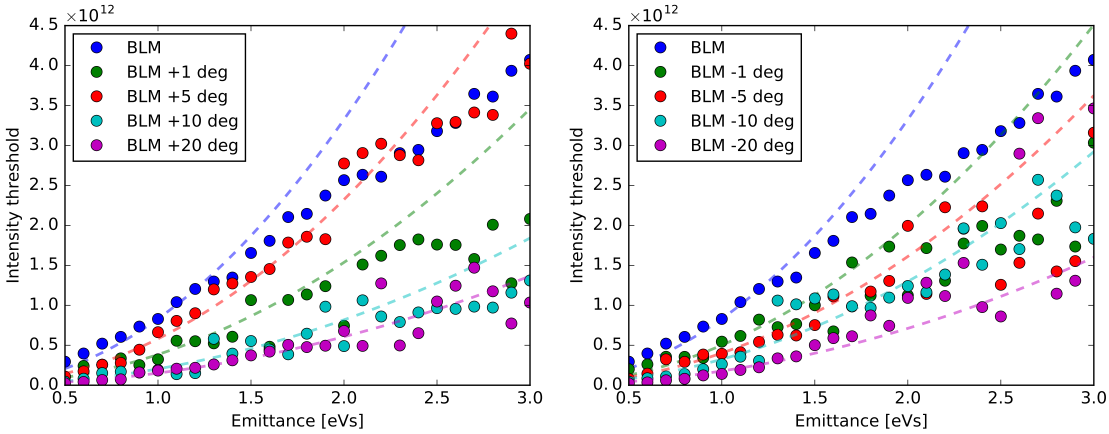

(c) BLM positive shift (d) BLM negative shift

Figure 4.11 – Effect of a phase shift on the intensity thresholds at 7 TeV in BSM (top) and in BLM (bottom), for a positive phase shifts (left) and for a negative phase shifts (right) from the ideal values of $\Phi_2 = \pi/2$ in BSM and $\Phi_2 = 0$ in BLM. Note that no apparent effect is observed in BSM even for a 20 deg phase shift, while in BLM the intensity thresholds are reduced even for a 1 deg phase shift. The data is fitted according to the analytical scaling of loss of Landau damping for the different operation modes (dashed colored lines), described in Section 4.6.3.

Given the stability issues with a phase shift and the requirement of a larger system for operation in BLM, it seems reasonable not to operate the high-harmonic rf system in this mode of operation under the full-detuning scheme. As the effect is significant even for small phase shifts (e.g., 1 deg), a very accurate phasing between the two rf systems (and higher power) would be required for operation in BLM even if the half-detuning scheme is used. It is important to note that the phase shift can be different for each bunch. In BLM, this means that the longitudinal profile would also be different from one bunch to another, which may not be desirable for the experiments.

4.8.3 Lower voltage ratio: $r = 1/4$

The stability threshold can also be increased by using a lower voltage of the high-harmonic rf system. Below, the case with $r = 1/4$ is analyzed, which does not provide a synchrotron frequency spread as large as for $r = 1/2$ (see Fig. 4.12). However, it is an interesting option for operation in BSM, as only 2 cavities would be required to keep the rf power below 300 kW per cavity.

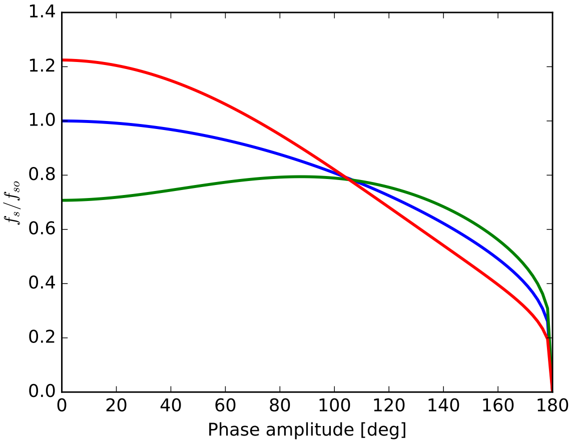

Figure 4.12 – Synchrotron frequency distribution for different modes of operation: single rf (blue), BLM (green), and BSM (red), calculated for a main rf system at 400 MHz with 16 MV, a high-harmonic system at 800 MHz with 4 MV, and a bunch with a binomial distribution defined by Eq. (3.7) with $n = 2$.

The intensity thresholds for the different modes of operation estimated by using macroparticle simulations are shown in Fig. 4.13. Both operation modes give sufficient improvement of the stability margin in comparison with a single rf system, although the thresholds for the HL-LHC nominal bunch length of 1.08 ns are lower as compared to the case with $r = 1/2$ due to the smaller spread in synchrotron frequencies. In BSM, the threshold is 7.7×10^{11} with a longitudinal emittance of 2.8 eVs, and in BLM it is 6.0×10^{11} for an emittance of 2.2 eVs.

For bunches shorter than 1 ns, the thresholds are comparable in both BSM and BLM, but above 1 ns the thresholds in BLM decrease. This is caused by the region in the synchrotron frequency distribution with $\omega_s'(J) \simeq 0$, visible in Fig. 4.12, as the small frequency spread in that region leads to a loss of Landau damping. The maximum of the synchrotron frequency distribution occurs for particles oscillating with 90 deg phase amplitude, which is covered by 1.25 ns long bunches. The reduction of the stability threshold starts for bunches slightly shorter than 1.25 ns, as the frequency spread near that area is also reduced.

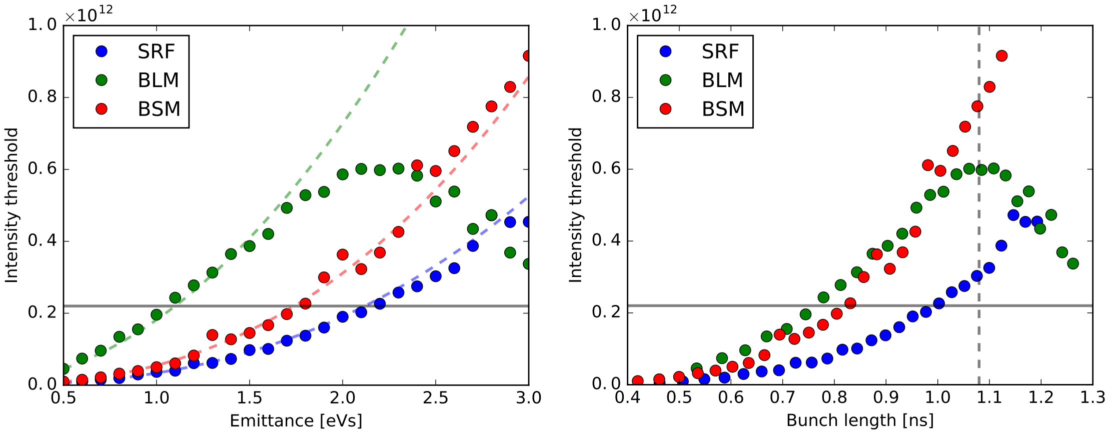

(a) Intensity thresholds vs emittance

(b) Intensity thresholds vs bunch length

Figure 4.13 – Intensity threshold as a function of the longitudinal emittance (left) and bunch length (right) at 7 TeV, for a 400 MHz system operating at 16 MV as a single rf (blue), and with an 800 MHz rf system at 4 MV ($r = 1/4$) in BLM (green) or in BSM (red). Note that the intensity thresholds are very similar in both BLM and BSM, but in BLM the thresholds decrease when the bunch covers the region with $\omega_s'(J) \simeq 0$. The data is fitted according to the analytical scaling of loss of Landau damping for the different operation modes (dashed colored lines), described in Section 4.6.3. The HL-LHC nominal bunch intensity is shown for reference (horizontal line), as well as the HL-LHC nominal bunch length (right plot, vertical dashed line).

It is important to note that, as the intensity threshold for BLM is lower, the effect of the induced voltage on the synchrotron frequency distribution is also smaller for intensities close to the stability threshold. For that reason, the results are in better agreement with the analytical scaling of loss of Landau damping in BLM described by Eq. (4.14) than in the case with $r = 1/2$.

4.8.4 Recovering the half-detuning scheme

Another interesting possibility for operation of the double rf system is to use a reduced voltage of 8 MV for the main rf system and run the high-harmonic system at 4 MV. This gives a reduction of the power required for beam loading compensation in the main rf system to approximately 280 kW per cavity, which is below the maximum power that the current LHC klystrons can provide [108].

For the 800 MHz harmonic rf system, 4 cavities can provide 1 MV each with a power requirement of 140 kW in both modes of operation, although it may be possible that BLM requires more power to obtain a phase synchronization with an accuracy of less than 1 deg.

The intensity thresholds found from macroparticle simulations for this rf configuration are shown in Fig. 4.14. In this situation, the distortion of the synchrotron frequency distribution in BLM becomes more important than in the cases with 16 MV for the main rf system. For that reason, the threshold in BSM is slightly higher than in BLM for any given bunch length.

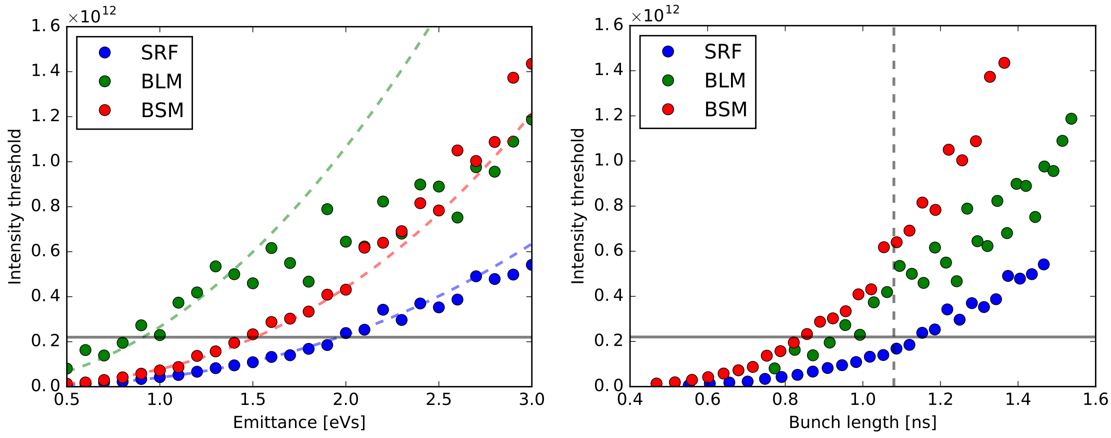

(a) Intensity thresholds vs emittance

(b) Intensity thresholds vs bunch length

Figure 4.14 – Intensity threshold as a function of the longitudinal emittance (left) and bunch length (right) at 7 TeV, for a 400 MHz system operating at 8 MV as a single rf (blue), and with an 800 MHz rf system at 4 MV in BLM (green) or in BSM (red). The data is fitted according to the analytical scaling of loss of Landau damping for the different operation modes (dashed colored lines), described in Section 4.6.3. The HL-LHC nominal bunch intensity is shown for reference (horizontal line), as well as the HL-LHC nominal bunch length (right plot, vertical dashed line).

In this case, the intensity threshold for a bunch with the HL-LHC nominal bunch length (1.08 ns) is 6.4×10^{11} in BSM (2.2 eVs) and 5.3×10^{11} in BLM (1.3 eVs). These values are lower than in the case with full voltage (16 MV and 8 MV for the 400 MHz and 800 MHz rf systems, respectively), but provide a sufficiently large margin for HL-LHC operation.

4.9 Operation with an extra 200 MHz rf system

As already mentioned in Section 4.5, longer bunches are possible in a 200 MHz rf system installed in the LHC and they could help reduce the e-cloud effect in the dipoles. In addition, capture losses could be reduced as the bucket has the same length as in the SPS. However, in order to compensate for the luminosity reduction for longer bunches from the geometric factor, the bunch intensity should be increased to about 2.4×10^{11} at 7 TeV and to 2.6×10^{11} at 450 GeV (taking into account beam losses) [109].

A design using superconducting $\lambda/4$ resonators (see Fig. 4.15) has been proposed for the 200 MHz rf system [108]. The impedance of the cavities would be $R/Q = 51\ \Omega$ and they would be fed by 500 kW power couplers.

For a total operating voltage of 6 MV at 7 TeV, 4 cavities per ring providing a voltage of 1.5 MV each would be needed. The power required at flat top is 470 kW for operation in half-detuning, which is within the limits.

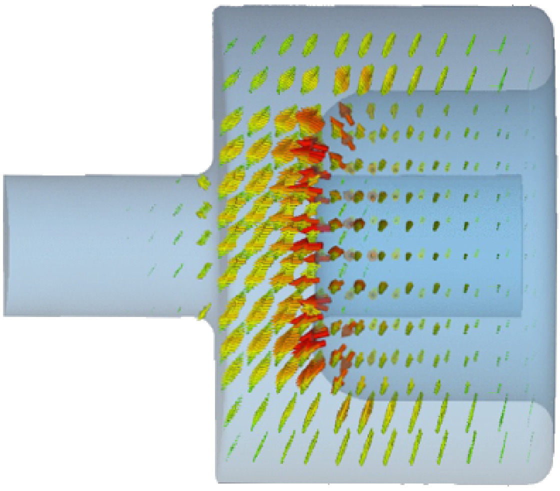

Figure 4.15 – Model of a superconducting $\lambda/4$ resonator, proposed to be used for the 200 MHz rf system for HL-LHC [108].

In this case, one 400 MHz cryogenic module per ring (4 rf cavities) would be kept in the machine for use as a second harmonic rf system to increase the stability margin. That system would be capable of providing the required 3 MV in half-detuning operation for a voltage ratio $r = 1/2$ at 7 TeV.

4.9.1 Longitudinal single-bunch stability at 450 GeV

At injection energy (450 GeV), with an rf voltage of 4 MV for the 200 MHz system, the HL-LHC bucket is matched to the SPS with an rf voltage at extraction of 10 MV. The single-bunch stability can be an issue at this energy, as the stability threshold scales as $N_{\mathrm{th}} \propto h^{7/4} V_{\mathrm{rf}}^{-1/4}$ for a given longitudinal emittance. Therefore, the threshold would be about 65% lower than that for a 400 MHz rf system.

It is also important to take into account that the effective reactive impedance will be also different, since it was calculated for 1 ns long bunches (see Section 4.1). The dependence of $\mathrm{Im}Z/n$ on the bunch length is shown in Fig. 4.16, and it can be seen that it increases for longer bunches. This is caused by the impedance contribution at low frequencies, mainly due to the resistive-wall impedance of the beam screens and collimators [86]. In particular, at 2 ns the effective impedance $\mathrm{Im}Z/n$ is about 10% higher than for 1 ns bunches.

The stability at 450 GeV was analyzed in macroparticle simulations. In this case, the synchrotron frequency for single rf is twice lower than in 400 MHz, since it scales as $f_{so} \propto \sqrt{V_{\mathrm{rf}} h}$. For that reason, simulations were done over 1×10^5 turns for single rf and BSM, and over 2×10^5 turns for BLM.

Results of macroparticle simulations are shown in Fig. 4.17. In single rf, the intensity threshold for the HL-LHC emittance at injection of 0.7 eVs (1.87 ns) is 1.6×10^{11}. This is, as expected,

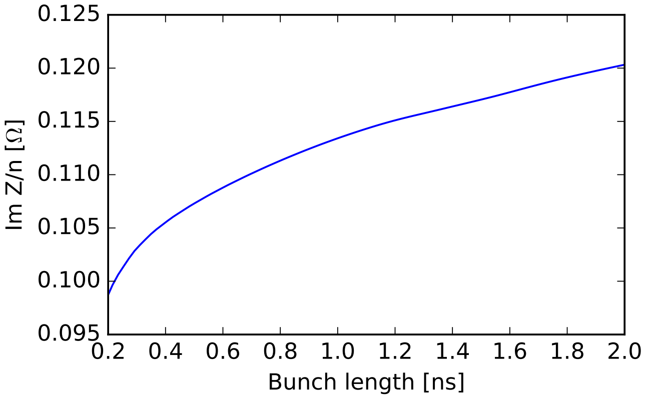

Figure 4.16 – Dependence of the effective reactive impedance on bunch length, calculated for a bunch with a binomial distribution defined by Eq. (3.7) with $n = 2$ and using the HL-LHC impedance model shown in Fig. 4.1.

lower than the required 2.4×10^{11}. That means that it is necessary to use the high-harmonic rf system at injection energy to avoid single-bunch instability. The second rf system would be operated with $r = 1/2$ (2 MV) to maximize the stability margin. In BSM, the stability threshold would be increased to 3.0×10^{11}, with the bunch length reduced to 1.62 ns for the same emittance. In BLM, the effect is stronger, with an intensity threshold of 1.3×10^{12} for a bunch length of 2.24 ns (0.7 eVs).

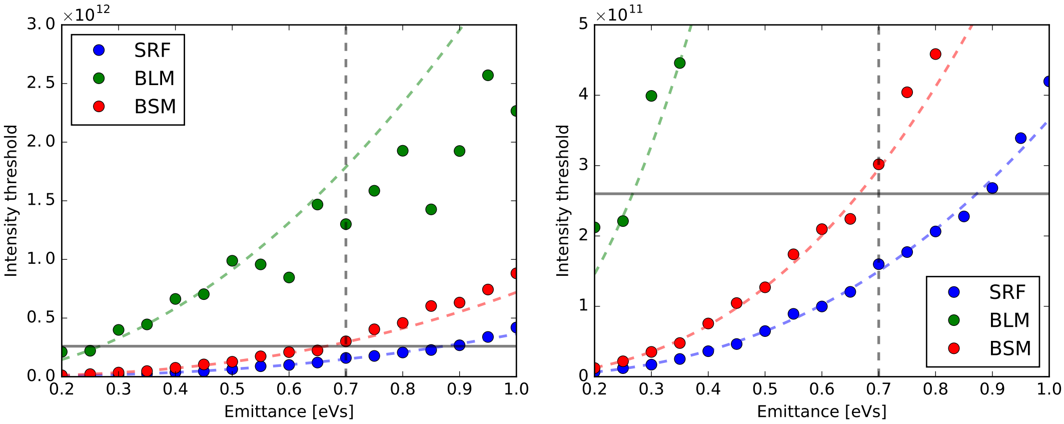

(a) Intensity thresholds vs emittance

(b) Intensity thresholds vs emittance (zoom)

Figure 4.17 – Intensity threshold as a function of the longitudinal emittance at 450 GeV, for a 200 MHz system operating at 4 MV as a single rf (blue), and with a 400 MHz harmonic system at 2 MV in BLM (green) or in BSM (red). The data is fitted according to the analytical scaling of loss of Landau damping for the different operation modes (dashed colored lines), described in Section 4.6.3. The HL-LHC bunch intensity at injection is shown for reference (horizontal line), as well as the HL-LHC nominal longitudinal emittance (vertical dashed line). Right plot, zoom of top plot on intensity range around the HL-LHC intensity.

4.9.2 Longitudinal single-bunch stability at 7 TeV

At 7 TeV, the situation is quite different. In this case, bunches would be 2 ns long for e-cloud mitigation [109]. For that bunch length and for a 200 MHz rf voltage of 6 MV, the longitudinal emittance is about 50% larger compared to the 400 MHz case (scales as $\varepsilon \propto (V_{\text{rf}} h)^{1/2} \tau^2$). Taking into account that the loss of Landau damping threshold scales as $N_{\text{th}} \propto \varepsilon^{5/2} h^{7/4} V_{\text{rf}}^{-1/4}$, we expect a slightly higher (~5%) stability threshold at 7 TeV in a single rf system.

Figure 4.18 presents the intensity threshold found from macroparticle simulations. For a bunch length of 2 ns, the emittance in single rf (200 MHz) is 3.8 eVs and the intensity threshold is 3.65×10^{11}. The stability margin is significantly increased with a high-harmonic rf system with a voltage ratio of $r = 1/2$. In BLM, it gives an intensity threshold of 2.13×10^{12} and an emittance of 2.5 eVs. In BSM, the threshold is 1.23×10^{12} and the emittance is 4.7 eVs.

However, this configuration is not optimum for operation with short bunches with a length of ~1.08 ns, which is the proposed value for HL-LHC [91]. In a single rf system (200 MHz), the minimum stable emittance for a bunch with an intensity of 2.3×10^{11} is about 3.5 eVs, corresponding to a bunch length of 1.9 ns. Shorter bunches could be achieved with a high harmonic (400 MHz), with the minimum bunch length being 1.3 ns in BLM (0.7 eVs) and 1.4 ns in BSM (2.6 eVs). In general, slightly longer bunches are needed to gain some stability margin, as well as special measures to counteract the shortening due to synchrotron radiation damping and keep the stability margin. Coupled-bunch instabilities were not considered here and might also impose larger emittances, and therefore longer bunches.

4.10 Conclusions

The single-bunch stability has been analyzed for the HL-LHC with macroparticle simulations using an updated impedance model and it was shown that the beam is stable for the HL-LHC parameters. A high-harmonic rf system (800 MHz) has been considered as an interesting option to increase the stability margin in the absence of a wideband longitudinal damper. Table 4.1 shows a summary of the stability thresholds determined from simulations for different configurations of the rf systems. Operation in BLM was found to be extremely sensitive to a phase shift between the two rf systems, and therefore it seems more reasonable to use the second rf system in BSM.

A 200 MHz rf system has also been considered for operation using longer bunches (about 2 ns) for e-cloud mitigation. Although the beam is not stable at 450 GeV in a single rf system, a large stability threshold both at flat bottom and at flat top is provided with the 400 MHz rf system used as second harmonic (see Table 4.1). Nevertheless, this configuration is not feasible for operation with bunches shorter than 1.3 ns at 7 TeV. Given the importance of the e-cloud in HL-LHC, next chapter describes a novel diagnostic tool to evaluate the e-cloud density in the machine.

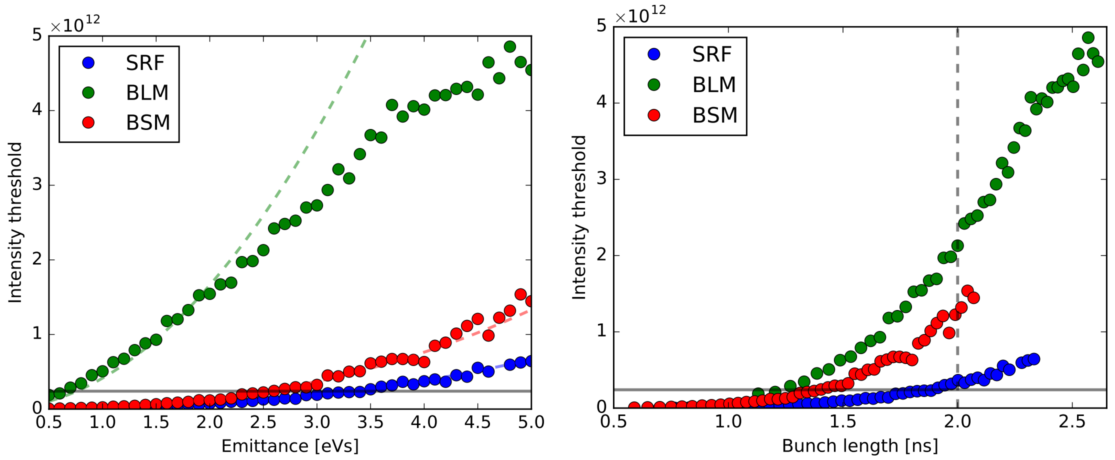

(a) Intensity thresholds vs emittance (b) Intensity thresholds vs bunch length

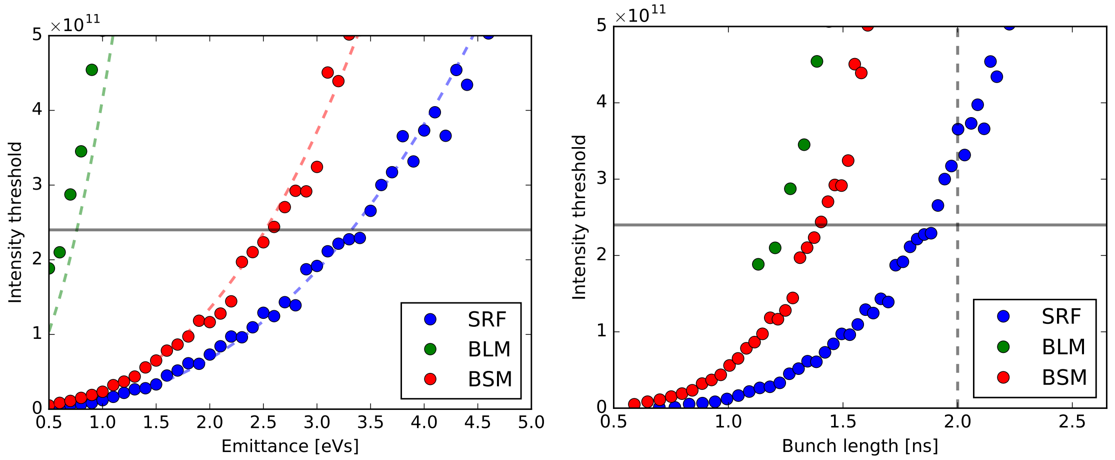

(c) Intensity thresholds vs emittance (zoom) (d) Intensity thresholds vs bunch length (zoom)

Figure 4.18 – Intensity threshold as a function of the longitudinal emittance (left) and bunch length (right) at 7 TeV, for a 200 MHz system operating at 6 MV as a single rf (blue), and with a 400 MHz harmonic system at 3 MV in BLM (green) or in BSM (red). The data is fitted according to the analytical scaling of loss of Landau damping for the different operation modes (dashed colored lines), described in Section 4.6.3. The HL-LHC bunch intensity is shown for reference (horizontal line), as well as the 2 ns bunch length (right plots, vertical dashed line). Bottom plots, zoom of top plots on intensity range around the HL-LHC intensity.

Table 4.1 – Summary of stability thresholds determined from simulations for different configurations of the rf systems. The thresholds shown for BLM are considering a perfect phasing between the two rf systems.

V_{200} [MV]	V_{400} [MV]	V_{800} [MV]	Operation mode	τ [ns]	ε [eVs]	N_{th}
450 GeV						
—	8	—	SRF	1.39	0.7	4.4×10^{11}
4	—	—	SRF	1.87	0.7	1.6×10^{11}
4	2	—	BSM	1.62	0.7	3.0×10^{11}
4	2	—	BLM	2.24	0.7	1.3×10^{12}
7 TeV						
—	16	—	SRF	1.08	2.50	3.0×10^{11}
—	16	8	BSM	1.08	3.08	1.1×10^{12}
—	16	8	BLM	1.08	1.77	2.1×10^{12}
—	16	4	BSM	1.08	2.81	6.0×10^{11}
—	16	4	BLM	1.08	2.18	7.8×10^{11}
—	8	—	SRF	1.08	1.78	1.7×10^{11}
—	8	4	BSM	1.08	2.18	6.4×10^{11}
—	8	4	BLM	1.08	1.25	5.4×10^{11}
6	—	—	SRF	2.0	3.79	3.7×10^{11}
6	3	—	BSM	2.0	4.74	1.2×10^{12}
6	3	—	BLM	2.0	2.50	2.1×10^{12}

5 Electron-cloud measurements in the LHC

In this chapter, a novel method to evaluate the e-cloud density in the accelerator through bunch phase measurements is presented. First, the e-cloud effects in the LHC and the performance limitations that they pose are reviewed. Then experimental results obtained from measurements of the average bunch phase and the bunch-by-bunch phase are shown. The benefits of using this technique compared to other indirect e-cloud measurements and simulations are demonstrated. Finally, the application of this method in the LHC operation is discussed.

5.1 Electron cloud in the LHC

At the beginning of the LHC run 1 (2009-2013), electron-cloud (e-cloud) effects were limiting the LHC operation, leading to an excessive heat load in the cryogenic system, a degradation of the vacuum, transverse instabilities, emittance growth, and particle losses [30, 29]. As the e-cloud buildup depends strongly on the bunch spacing, bunch trains with different bunch spacings were injected into both LHC rings (Beam 1 and Beam 2) during the commissioning (see Chapter 2 for beam parameters). First, beams with a bunch spacing of 150 ns were injected, accelerated to 3.5 TeV, and brought into collisions without any severe e-cloud effect. Then, beams with a bunch spacing of 75 and 50 ns were injected into the LHC, but the e-cloud effects were stronger and were limiting the number of injections, especially for beams with 50 ns bunch spacing. Scrubbing with beams was proven to be an effective method for reducing the secondary electron yield (SEY) below the e-cloud build-up threshold for 50 ns beams, although a long time was required to achieve the desirable effect (2.5 days with 75 ns beams and 15 days with 50 ns beams) [110].

Beams with 25 ns bunch spacing were injected later in 2011, but the strong e-cloud effects were limiting the beam intensity circulating in the ring and quickly degrading the beam quality. Only 60 bunches per beam could be accelerated to 3.5 TeV and collided. At the very end of run 1, after scrubbing with 25 ns beams (5 days in 2011 and 6 days in 2012), it was possible to accelerate 804 bunches per beam to 4 TeV, but the beams were not brought into collision.

The maximum number of bunches collided at 4 TeV was 396, significantly less than the design number of bunches (2808).

The LHC operation was resumed in April 2015 after the Long Shutdown 1, with an increased top energy of 6.5 TeV. The machine commissioning with bunch trains started by injecting bunches spaced by 50 ns. Some e-cloud activity was observed, but e-cloud quickly vanished after a few fills of scrubbing. Then the bunch spacing was reduced to 25 ns and e-cloud effects reappeared. Two scrubbing runs were scheduled, the first one 9 days long and the second one 14 days long. Although those runs helped in reducing the SEY of the beam chambers, it could not be reduced below the e-cloud build-up threshold.

Following the second scrubbing run of 2015, the LHC started the physics program with 25 ns beams. The number of bunches injected into the LHC was gradually increased since that time, but the excessive heat load in the cryogenic system produced by the e-cloud slowed down the intensity ramp-up. By the end of the 2015 run, the LHC could not yet be filled completely with the maximum number of bunches.

The e-cloud is currently considered to be the main limitation for LHC and HL-LHC operation with 25 ns beams and the deterioration of the beam quality can also cause a reduction of the luminosity delivered to the experiments. Although alternative scenarios have been proposed to overcome the e-cloud limitations, such as different filling patterns (50 ns, 8b4e [98]...) or the installation of a 200 MHz rf system to operate with longer bunches, those options pose other challenges and can also potentially lead to a performance reduction. The preferred option for e-cloud mitigation relies on efficient scrubbing of the beam chamber surface to further reduce its SEY. The application of amorphous-carbon coating to the HL-LHC beam screens is also under consideration [4]. Observation tools are required for optimization of the scrubbing strategy and time [42] and the method presented below is one of them.

5.2 Bunch phase shift

As introduced in Section 1.3, the electrons forming the e-cloud are accelerated by the electric field generated by the beam, causing an energy loss of the proton beam that depends on the e-cloud density. Then, the e-cloud buildup can be observed as an increasing bunch-by-bunch energy loss along the bunch trains. The bunch energy loss per turn due to e-cloud ΔE_e is compensated by the rf system, similarly to the energy loss due to the resistive impedance (see Section 1.2.1) or due to synchrotron radiation, and is therefore connected with an rf phase shift $\Delta\varphi_e$ by the following relation:

$$\Delta E_e = N e V \left[\sin(\varphi_s + \Delta\varphi_o + \Delta\varphi_e) - \sin(\varphi_s + \Delta\varphi_o)\right], \tag{5.1}$$

where N is the bunch intensity, V is the amplitude of the rf voltage, and φ_s is the synchronous phase in the absence of intensity effects. The phase shift due to other energy loss mechanisms is $\Delta\varphi_o$ and, in the LHC, it is defined mainly by the energy loss due to synchrotron radiation

ΔE_{SR} and resistive impedance of the ring. The former is the same for all bunches, as it only depends on the proton energy E ($\Delta E_{\mathrm{SR}} \propto E^4$), and its contribution to $\Delta\varphi_o$ is very small even at 7 TeV (~ 0.02 deg with $V = 10$ MV). The energy loss due to resistive impedance depends on bunch length and distribution, but the associated phase shift is in general also small (less than 0.1 deg for nominal beam parameters) [111]. For small $\Delta\varphi_e$, Eq. (5.1) becomes

$$\Delta E_e \approx N e V \Delta\varphi_e \cos(\varphi_s + \Delta\varphi_o). \tag{5.2}$$

The LHC operates above transition, which implies that $\varphi_s = \pi$ in the absence of acceleration and $\pi/2 < \varphi_s < \pi$ during acceleration. As the maximum phase deviation from π during the acceleration in the LHC is around 4 deg and $\Delta\varphi_o$ is smaller than 0.1 deg, then $\cos(\varphi_s + \Delta\varphi_o) \approx -1$ and Eq. (5.1) can be replaced by

$$\Delta E_e \approx -N e V \Delta\varphi_e. \tag{5.3}$$

Therefore, a negative phase shift $\Delta\varphi_e$ indicates an energy loss.

The average bunch power loss P_L can be calculated from the bunch energy loss per turn as

$$P_L = f_{\mathrm{rev}} \Delta E_e, \tag{5.4}$$

where f_{rev} is the revolution frequency.

The bunch phase shift can be measured in the LHC using the phase module (PM) described in Section 2.3.3. The phase measured by the PM ($\Delta\varphi_{\mathrm{PM}}$ in Fig. 2.6) is defined as

$$\Delta\varphi_{\mathrm{PM}} = \varphi_s + \Delta\varphi_o + \Delta\varphi_e + \varphi_{\mathrm{off}}, \tag{5.5}$$

where φ_{off} is an unknown phase offset due to the different delays of the pick-up and voltage signals, and the time of flight from the cavities to the pickup. In order to obtain $\Delta\varphi_e$, it is necessary to define the other terms of Eq. (5.5). Both phases φ_s and φ_{off} are the same for all bunches and the difference in the phase shift $\Delta\varphi_o$ from bunch to bunch is in general small (less than 0.1 deg, see above). Therefore, $\Delta\varphi_e$ can be computed as the phase relative to the first bunch train, which in normal operation is shorter (12 bunches for 25 ns beams and 6 bunches for 50 ns beams) and has the Beam Abort Gap in front of it (3 μs without beam), thus being practically not affected by e-cloud ($\Delta\varphi_e \approx 0$).

5.3 Average bunch phase

The first e-cloud observations based on bunch phase measurements were done using the average phase of all bunches $\langle\Delta\varphi_{\mathrm{PM}}\rangle$ [112], as this signal is calculated by the rf phase loop in normal operation and was available in the CERN logging database. The total beam energy loss per turn due to e-cloud ΔE_{eT} is the sum of the energy loss of each bunch defined by Eq. (5.3):

$$\Delta E_{eT} = \sum_{k=1}^{M} \Delta E_{ek} \approx -e\,V \sum_{k=1}^{M} N_k\, \Delta\varphi_{ek}, \tag{5.6}$$

where M is the total number of bunches.

For bunches with small deviations from the average bunch intensity $\overline{N} = \sum_{k=1}^{M} N_k / M$, i.e., $N_k = \overline{N} + \Delta N_k$, where $\Delta N_k \ll \overline{N}$; the total beam energy loss per turn can be approximated as

$$\Delta E_{eT} \approx -e\,V\,M\,\overline{N}\,\langle\Delta\varphi_e\rangle, \tag{5.7}$$

where the average phase shift due to e-cloud $\langle\Delta\varphi_e\rangle$ can be calculated using Eq. (5.5) as

$$\langle\Delta\varphi_e\rangle = \langle\Delta\varphi_{\mathrm{PM}}\rangle - \langle\Delta\varphi_o\rangle - \varphi_s - \varphi_{\mathrm{off}}. \tag{5.8}$$

Figure 5.1 shows an example of a fill with a strong e-cloud effect that gave an additional shift of the average phase at each injection. This means that the beam energy loss per turn and per particle was increasing with total beam intensity in the ring, suggesting a higher e-cloud density after each injection of a new SPS bunch train (e-cloud buildup).

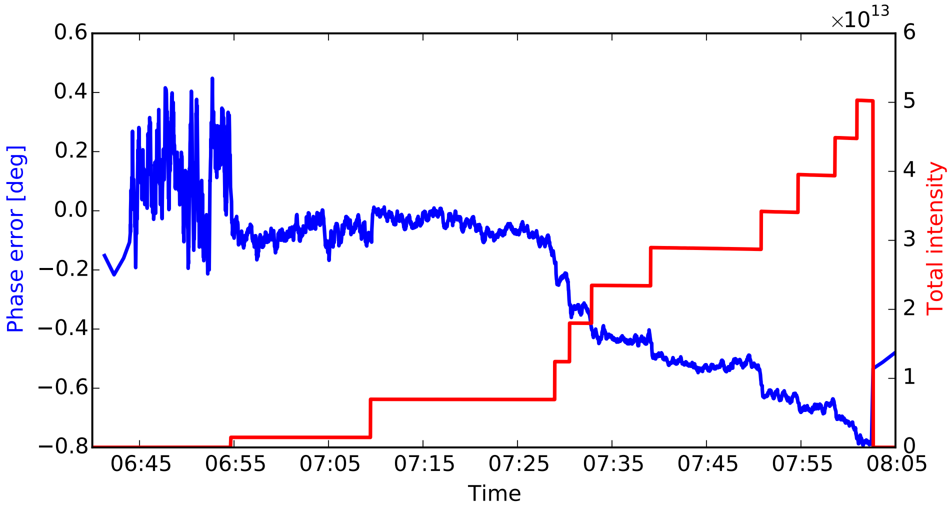

Figure 5.1 – Average phase shift (blue) and total beam intensity (red) of Beam 1 at the LHC flat bottom (450 GeV) during the injection of trains of 48 bunches spaced by 50 ns from the SPS. Note the phase change after each bunch train injection. Average intensity $\overline{N} \sim 1.1 \times 10^{11}$. Fill 1502 (20-11-2010).

An analysis of several fills with 50 ns beams during the LHC scrubbing run in April 2011 is presented in Fig. 5.2. The average phase shift due to e-cloud at each injection is shown as a function of the total beam intensity circulating at that moment. The phase difference between $\langle\Delta\varphi_e\rangle$ and $\langle\Delta\varphi_{\mathrm{PM}}\rangle$ is taken into account by performing a linear fit of the total beam intensity against the average phase. The slopes of these curves, shown in Fig. 5.3, are related to the

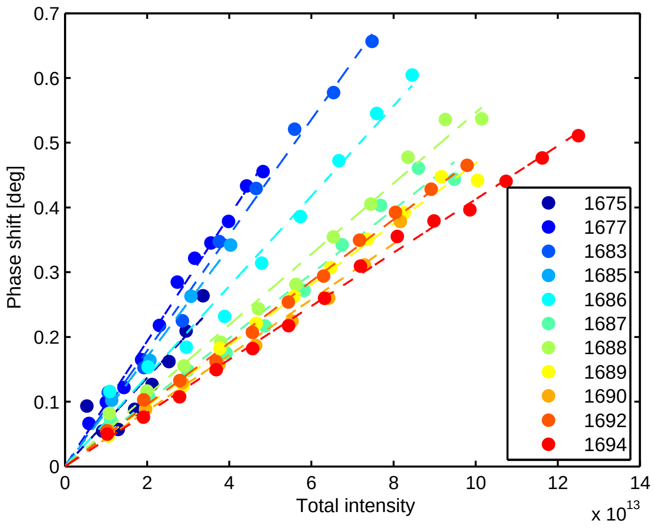

Figure 5.2 – Average phase shift at bunch train injections in the LHC as a function of the total beam intensity in Beam 1 for the 50 ns beams during the scrubbing run in April 2011. The decrease in the slope of the curves between the first and the last fills is a sign of surface scrubbing. Each color corresponds to a different LHC fill. Note the reduction of the slope with time (fill number). Average intensity $\overline{N} \sim 1.2 \times 10^{11}$.

e-cloud density and therefore the decrease in the slope during the scrubbing run is a sign of SEY reduction.

Similar results were obtained for fills with 75 ns beams at the beginning of the LHC run 1 and later with 25 ns beams. In Fig. 5.3, one can also see that after the scrubbing run in April 2011 the slopes were similar for 75 and 50 ns beams, meaning that the SEY was reduced below or very close to their e-cloud build-up threshold. That was not the case for the 25 ns beams even after the 2012 scrubbing run.

The use of the average phase shift for e-cloud observations has a few limitations that must be taken into account. Usually, e-cloud causes particle losses that are higher at the end of the bunch trains, as shown in Fig. 5.4. Under these circumstances the uniform bunch intensity approximation used in Eq. (5.7) is not valid anymore. Another limitation is due to thermal drifts of the phase, which cannot be distinguished from those caused by changes in the e-cloud density (e.g., due to particle losses). In fact, the data for Beam 2 had inexplicably larger drifts, so that only the average phase measurements for Beam 1 were valid. In addition, the average phase can be affected by the errors in the bunch-by-bunch measurements discussed in Section 2.3.3.

5.4 Bunch-by-bunch phase shift

The limitations of the average phase shift measurements described above can be overcome by using the bunch-by-bunch phase data. In this case, the data is acquired using the tool

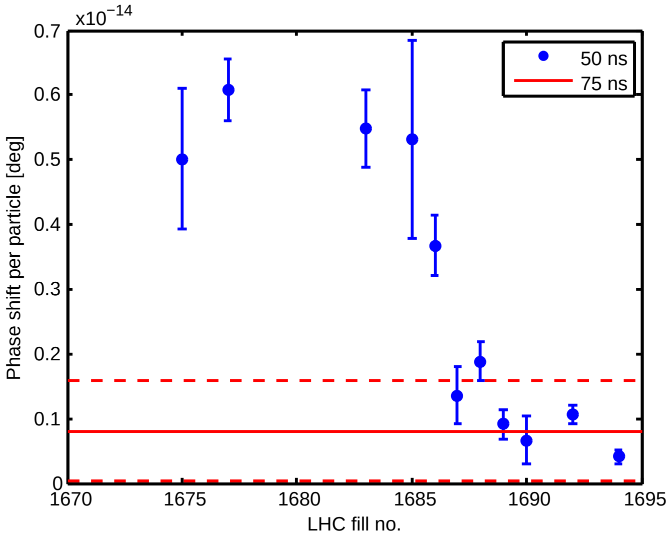

Figure 5.3 – Ratio of the phase shift to total beam intensity for different LHC fills with 50 ns beams (blue circles) and mean value (solid red line) together with standard deviation (dashed red lines) of the same ratio for the 75 ns beams. After scrubbing run in April 2011 the value of the ratio for the 50 ns beams converged to the 75 ns beams value.

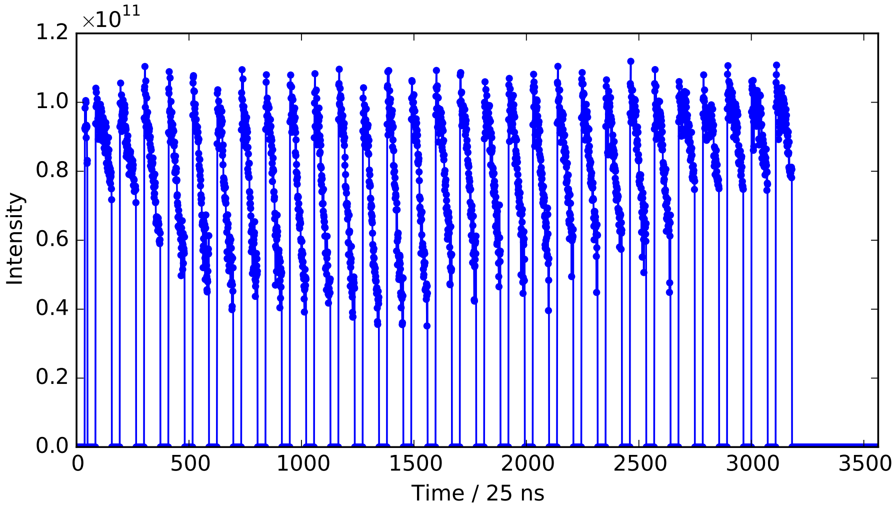

Figure 5.4 – Example of the bunch intensity pattern for the 25 ns beams with high e-cloud density. The triangular bunch trains are caused by the particle loss from the e-cloud effect. The last five bunch trains were injected later and they were still losing particles. Beam 1. Fill 2251 (25-10-2011).

described in Section 2.3.3, which provides a high accuracy (of the order of 0.1 deg) thanks to the implemented corrections and post-processing. In the following, bunch-by-bunch data is used to observe details of the e-cloud buildup structure and to analyze the e-cloud evolution over time (from fill to fill).

5.4.1 Observations of the e-cloud buildup

The e-cloud buildup can be observed as a phase difference between the bunches at the beginning and the end of the bunch trains, shown in Fig. 5.5 for two fills during the 2012 scrubbing run with 25 ns beams. The reduction of the SEY due to scrubbing led to a decrease in the phase variation along the bunch trains from about 1.2 deg at the beginning of the scrubbing run (see Fig. 5.5a) to ~ 0.3 deg at the end of it (see Fig. 5.5b). Nevertheless, the e-cloud effect was still significant for the 25 ns beams after the scrubbing run in 2012.

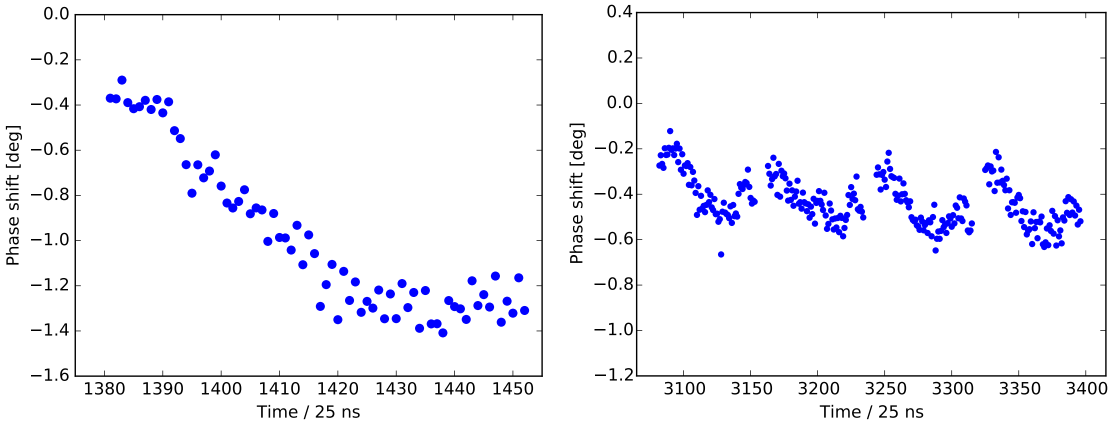

(a) Fill 3389, 6-12-2012. $\overline{N} \sim 1.1 \times 10^{11}$

(b) Fill 3405, 9-12-2012. $\overline{N} \sim 1.2 \times 10^{11}$

Figure 5.5 – Bunch-by-bunch phase shift (corrected and post-processed) along bunch trains immediately after injection. Measurements on Beam 1 during a fill at the beginning (left) and at the end (right) of the 2012 scrubbing run with 25 ns beams. At the end of the scrubbing run, four trains of 72 bunches spaced by 250 ns were injected each time.

A similar effect could be seen before the 2011 scrubbing run for 50 ns beams, but no e-cloud was observed for these beams after reducing the SEY below the build-up threshold by scrubbing with beams [113]. In 2012, the phase variation along the trains with 50 ns spacing was smaller than the measurement resolution (which is around 0.1 deg) [114].

Another observation of the e-cloud buildup is shown in Fig. 5.6 as an increasing bunch-by-bunch power loss along the bunch trains, calculated as

$$P_L = -f_{\text{rev}}\, N\, e\, V\, \Delta\varphi_e \tag{5.9}$$

from the measured phase shift (corrected and post-processed). This example corresponds to measurements before the 2012 LHC scrubbing run.

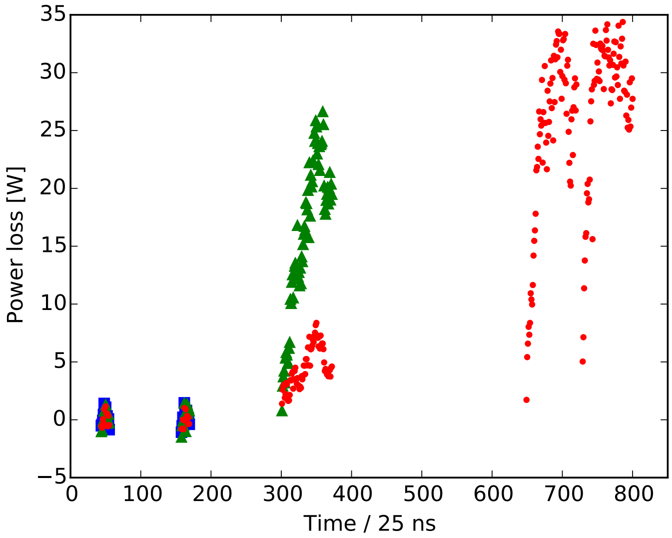

Figure 5.6 – Bunch-by-bunch power loss in Beam 1 for a fill with 25 ns beam before the 2012 scrubbing run (Fill 2826, 10-7-2012) at three different moments: 15 min after the injection of the first trains of 12 bunches (blue squares), a few seconds after the injection of a train of 72 bunches (green triangles), and a few seconds after the injection of two trains of 72 bunches spaced by 225 ns (red circles). The first short bunch train (12 bunches, blue) is used as a reference for the phase shift measurement. $\overline{N} \sim 1.1 \times 10^{11}$.

5.4.2 E-cloud evolution and scrubbing efficiency

Using the bunch-by-bunch phase shift instead of the average phase shift, the total beam power loss P_T can be calculated more accurately as the sum over all bunches:

$$P_T \approx -f_{\text{rev}}\, e\, V \sum_{k=1}^{M} N_k\, \Delta\varphi_{ek}. \tag{5.10}$$

This allows the time evolution during the cycle of the e-cloud density in the ring to be seen. An example of the variation of the total beam power loss during a fill with beams with 25 ns spaced bunches is shown in Fig. 5.7 (black line). Note that the power loss increases after each bunch train injection and then again during the acceleration.

Similarly to the results presented in Fig. 5.3, the maximum of the average power loss per particle P_p calculated as

$$P_p = \max\left(\frac{P_T}{\sum_{k=1}^{M} N_k}\right) \tag{5.11}$$

gives an indication of the e-cloud activity during one fill. A comparison of P_p for different fills during the 2012 scrubbing run is shown in Fig. 5.8 and the decrease in power loss per particle is a clear indicator of SEY reduction (scrubbing). Note that the scrubbing is fast at the beginning and it is slower afterward due to the reduction of the e-cloud density.

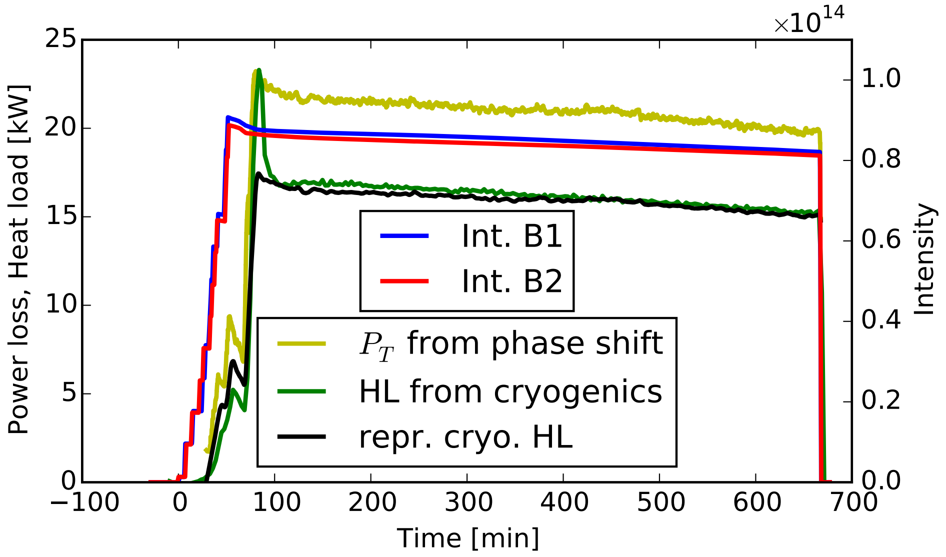

Figure 5.7 – Total beam power loss (P_T) found from the phase shift (yellow line) and the heat load (HL) measured by the cryogenic system (green line) [115, 116], for a fill with 25 ns beams accelerated to 4 TeV (Fill 3429, 13-12-2012). An estimation of the cryogenic heat load (black line) was made from the phase shift measurements as described later in the text (see Section 5.5.1). A scale factor of 0.76 was used to fit the part of the measured cryogenic heat load at 4 TeV. The total beam intensities during the cycle are shown for Beam 1 (blue line) and for Beam 2 (red line).

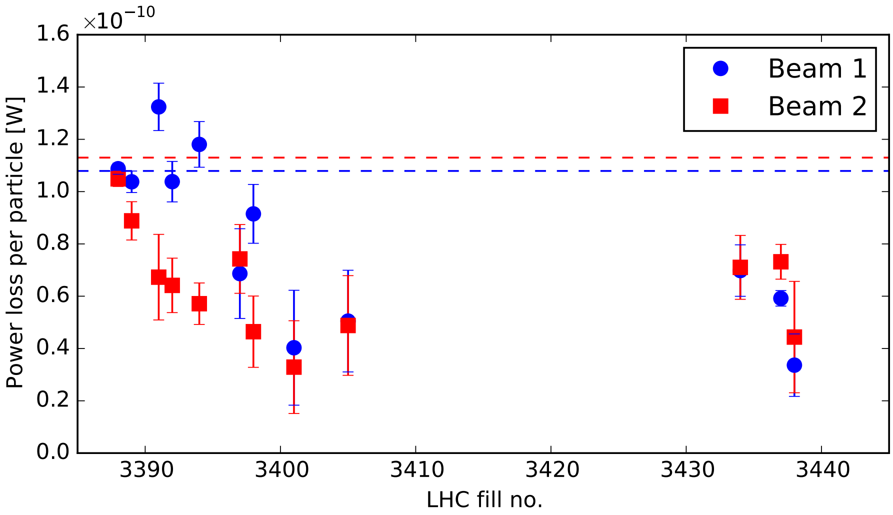

Figure 5.8 – Evolution of the maximum power loss per particle P_p during the 2012 scrubbing run at 450 GeV with 25 ns beams for Beam 1 (blue circles) and for Beam 2 (red squares). The dashed lines represent the level achieved after the scrubbing run in 2011 for both beams. The decrease in power loss P_p is a clear indicator of the SEY reduction. Error bars are defined by the noise of the bunch-by-bunch phase measurements.

Figure 5.9 shows the evolution of the power loss P_p evaluated from the bunch phase during the first scrubbing run in 2015 with 50 (green) and 25 ns beams (orange). A fast conditioning is observed at the beginning of the scrubbing run with 50 ns beams. In the second period with 50 ns beams, the SEY was already below the e-cloud build-up threshold and no e-cloud is observed. For the 25 ns beams, there is no apparent reduction of the e-cloud activity because the beam parameters were continuously optimized to enhance the e-cloud buildup and therefore the scrubbing efficiency. In particular, the number of bunches per injection was gradually increased (12 – 24 – 36 – 48 – 60 – 72 bunches). For each case, the number of injections per fill was increased in steps and the spacing between bunch trains was reduced. With these considerations, a reduction of the e-cloud activity can only be observed when conditions are similar, as for example for fills from 3933 to 3939.

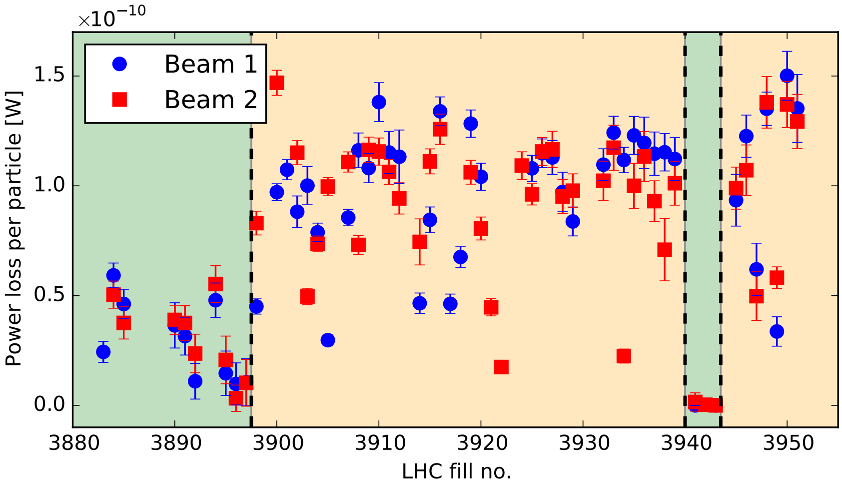

Figure 5.9 – Evolution of the maximum power loss per particle P_p at 450 GeV during the first scrubbing run in 2015 for Beam 1 (blue circles) and for Beam 2 (red squares). The areas shaded in green correspond to periods with 50 ns beams and those shaded in orange with 25 ns beams. The effect of scrubbing is only visible when the beam parameters are similar, as for first fills with 50 ns beams and for fills 3933–3939 with 25 ns beams. Outliers correspond to fills with lower intensity per bunch and/or small number of injections.

After the two scrubbing runs in 2015, the physics program started with bunches spaced by 25 ns. Limited by the cryogenic system capacity, the number of injected bunches and the average bunch intensity was gradually increased as the SEY was being reduced by the effect of scrubbing [96]. The evolution of the power loss P_p, shown in Fig. 5.10, confirms the scrubbing effect during the physics fills. Compared to the scrubbing run with 25 ns beams in 2012, the slope of the power loss reduction is less pronounced in this case. There are two main reasons for that. First, the maximum length of the bunch trains was limited to 144 (it was 288 in 2012) due to a problem with the LHC injection beam stopper (TDI), and longer bunch trains can scrub more efficiently. Second, the spacing between the bunch trains was increased to reduce the e-cloud effects with the aim of maximizing the luminosity delivered to the experiments. Note that during a special run with 100 ns bunch spacing and $\beta^* = 90$ m (fills from 4495 to 4511), as expected, no e-cloud was observed from phase shift measurements.

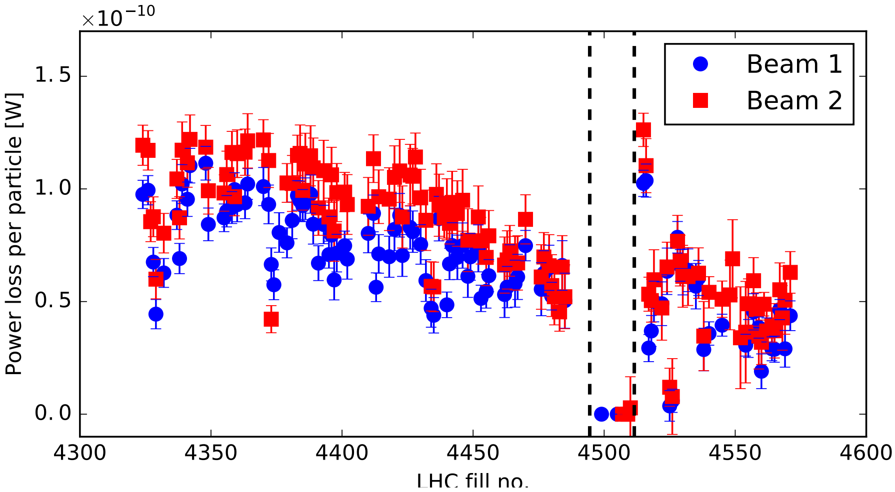

Figure 5.10 – Evolution of the maximum power loss per particle P_p at 450 GeV during the intensity rampup in 2015 for Beam 1 (blue circles) and for Beam 2 (red squares). Note the decrease in the power loss, which indicates a reduction of the SEY. The slope is less pronounced than in 2012 because both the number of bunches and the average bunch intensity was being gradually increased during the intensity rampup. A special run with 100 ns bunch spacing corresponds to fills from 4495 to 4511 (between dashed lines).

5.5 Comparison with other e-cloud measurements and simulations

The method for e-cloud observation described above in this chapter has been compared with an indirect measurement of the e-cloud density based on the heat load deposited in the cryogenic system [115, 116], as well as with macroparticle simulations using the code PyECLOUD [99, 36].

5.5.1 Cryogenic heat load measurements

The energy lost by the beam due to the presence of e-cloud is transferred to the electrons and is finally deposited in the beam screens, where it has to be absorbed by the cryogenic system. Therefore, the beam power loss calculated from the phase shift can be compared with the heat load measured by the cryogenic system [115, 116]. However, it is necessary to take into account that the cryogenic system sees the heat load only in the superconducting magnets, which are almost exclusively found in the arcs. Also, as the cryostats are shared by the two beam chambers in the vast majority of the cases, the contributions of both beams are added. Additionally, the cryogenic system has a slow time response (~ 5 min) due to its large thermal inertia. Note also that the measured heat load includes image current and synchrotron radiation contributions, which should be calculated and subtracted to obtain an estimate of the e-cloud induced heating.

The heat load measured by the cryogenic system can be reproduced by the beam power loss obtained from the measured phase shift by applying a moving average filter with a window of

5 min, similar to the cryogenic system, and then defining a proper scale factor. An example of the estimation of the heat load in the cryogenic system from the phase shift for a fill with 25 ns beams accelerated to 4 TeV is shown in Fig. 5.7. The scale factor giving the best agreement with the cryogenic heat load measurements (found for several fills in 2012) is ~ 0.79 at 4 TeV and ~ 0.7 at 450 GeV. This means that there is an increase in the heat load with beam energy that is larger in the arcs than in the straight sections, since the heat load in the cryogenic system due to the e-cloud is determined mainly by the arcs.

5.5.2 Simulations of the e-cloud buildup

The bunch-by-bunch power loss due to e-cloud has been calculated [36] from simulations performed with the code PyECLOUD (see [99] for details). In simulations, an energy balance is applied to a slice of the beam chamber to calculate the energy loss per turn of each bunch, defined as the difference between the total energy of the electrons before and after the bunch passage plus the energy lost in electron-wall collisions. This calculation is done for each different element of the accelerator and extrapolated to its full length.

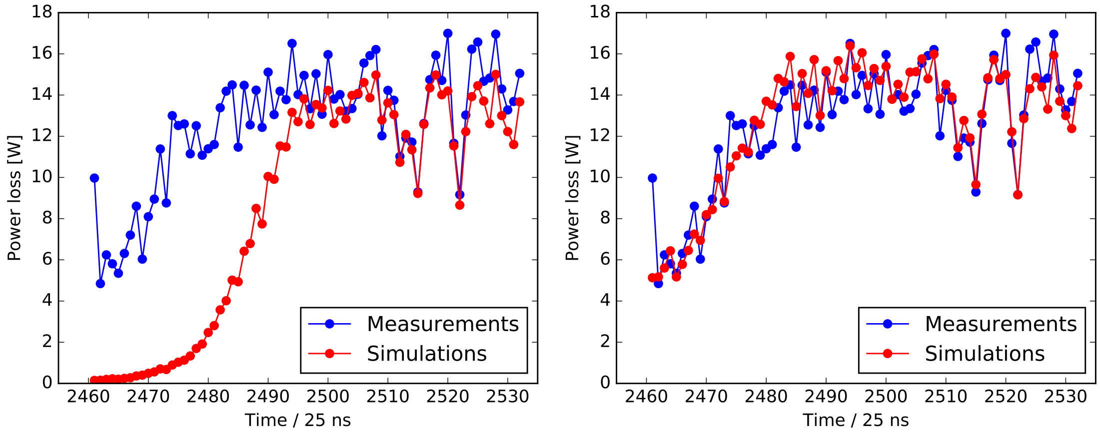

(a) Simulations without uncaptured beam

(b) Simulations with 10% uncaptured beam

Figure 5.11 – Bunch-by-bunch energy loss per turn calculated for a bunch train of 72 bunches spaced by 25 ns from phase measurements (blue circles) and from simulations (red circles) based on the measured beam parameters [36]. Simulations were run both without uncaptured beam (left) and with a 10% of uncaptured beam in the machine (right) [99]. Average bunch intensity $\overline{N} \sim 1.0 \times 10^{11}$. Fill 2251 (25-10-2011).

Measurements taken in 2011 were selected for a comparison with simulations and they both are shown in Fig. 5.11. At that time, the power loss was dominated by the e-cloud in the dipole magnets and the effect from all other elements was neglected in the simulations. The simulations were done using the measured beam parameters (filling pattern, bunch lengths, and intensities). The SEY was estimated from the measured heat load in the cryogenic system and found to be around 1.5. With this SEY value, the agreement between measurements and simulations is good when the e-cloud is saturated (end of the bunch trains), but the buildup is faster in measurements. This discrepancy can be explained, for example, by the presence of uncaptured beam circulating in the machine. The simulation in Fig. 5.11b shows that by adding a 10% uncaptured beam the agreement is very good and the details of the e-cloud buildup seen in the phase shift measurements can be well reproduced. Nevertheless, this might be only a partial explanation, as the amount of uncaptured beam in the LHC is usually lower than 10% even during scrubbing runs. Another possible cause of the small discrepancy between the measurements and the simulated buildup could be due to the assumed SEY dependence on the energy of impinging electrons for low energy electrons [99].

5.6 LHC operation

During the LHC run 2, which started in April 2015, luminosity is produced using beams with 25 ns spaced bunches. Figure 5.12 shows the new diagnostic tool using the measured bunch-by-bunch phase shift described in this chapter, which is implemented in the LHC control room for operational purposes. It has been regularly used to monitor the e-cloud activity, first during the scrubbing runs (June and July, 2015) and then in operation during the intensity ramp-up with the increasing number of bunches. The tool provides essential information for taking the decision on when to dump the beam and refill to achieve optimal scrubbing conditions and shorten the scrubbing run. The decision is based on the e-cloud activity seen in the measured bunch-by-bunch power loss.

Another possibility is to use the phase shift measurements as a feed-forward signal for the cryogenic system. As it was mentioned above, this tool provides instantaneous information on the heat load deposited by the e-cloud whereas the measured heat load in the cryogenic system has a time constant of the order of minutes. With the phase measurement information, necessary changes in the cryogenic system can be anticipated. To improve the accuracy of the predictions, a calibration of the scale factor for the heat load estimation can be done regularly using the measured heat load in the cryogenic system.

5.7 Conclusions

Bunch-by-bunch synchronous phase measurements have been suggested and proven to be a good diagnostic tool for the e-cloud effect. It is possible thanks to the high accuracy of the beam Phase Module and special corrections applied for signal treatment. This novel method can be used to observe the e-cloud build-up along the bunch trains and to calculate the total beam power loss. Measurements of the heat load in the cryogenic system are well reproduced, although a scale factor that depends on the beam energy needs to be applied. Phase shift measurements have a very good agreement with simulations of the e-cloud build-up. The use of this method in operation has been proven to ease the scrubbing run optimization and can be also used as an additional input for the cryogenic system.

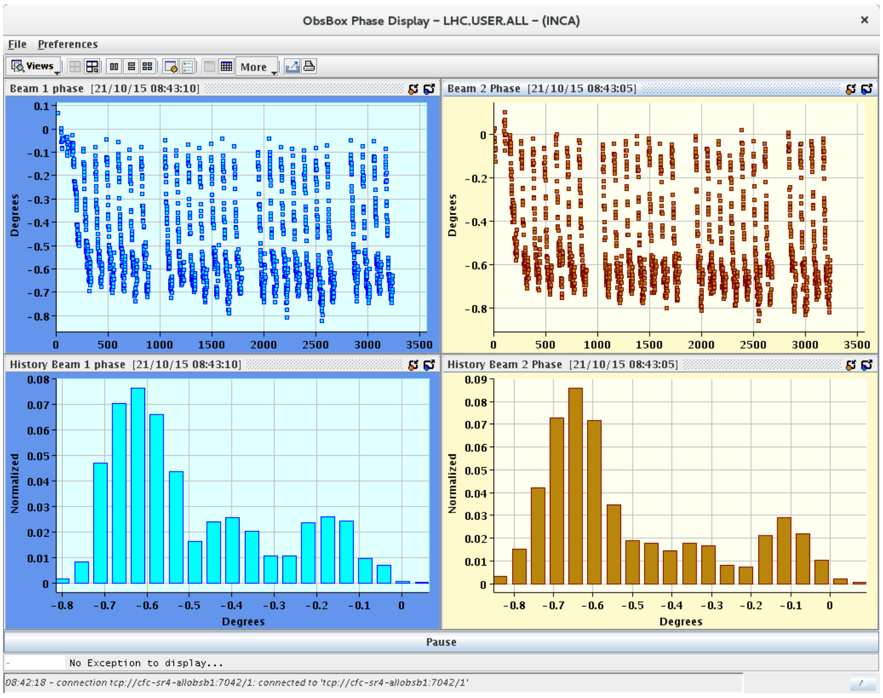

No Exception to display...

08:42:18 - connection tcp://cfc-sr4-allobsb1:7042/1: connected to 'tcp://cfc-sr4-allobsb1:7042/1'

(a) Full machine

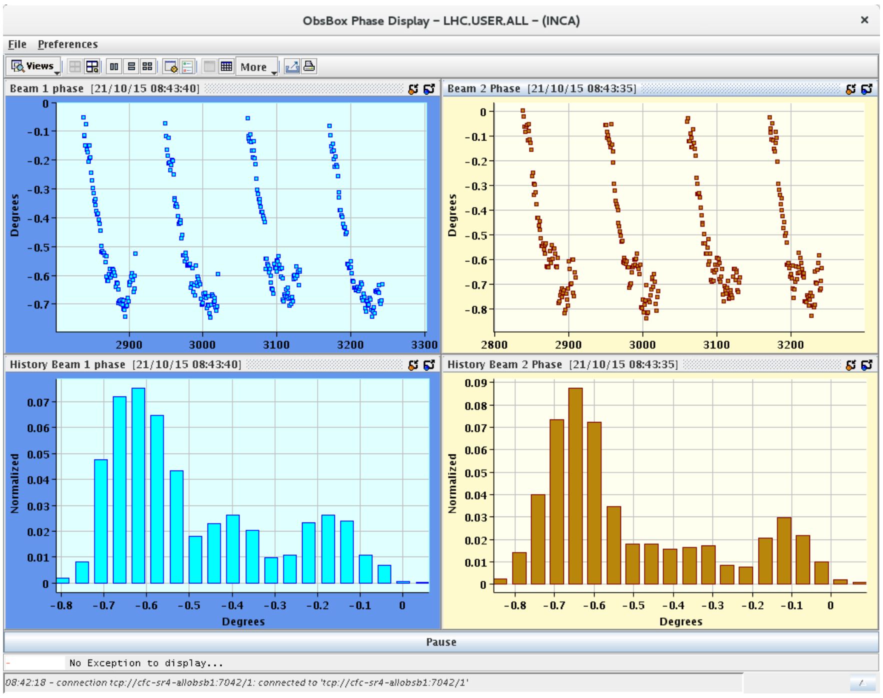

No Exception to display...

08:42:18 - connection tcp://cfc-sr4-allobsb1:7042/1: connected to 'tcp://cfc-sr4-allobsb1:7042/1'

(b) Zoom over the last four bunch trains

Figure 5.12 – Graphical user interface of the bunch-by-bunch phase measurement based on the method described in this chapter. The interface was written in Java by the OP group (thanks to Georges-Henry Hemelsoet) and it is available in the LHC control room. The example shows the e-cloud signal along the bunch trains for the full machine (top) and a detailed view of the last four bunch trains (bottom).

6 Summary and conclusions

Intensity effects can limit the performance of high-intensity particle accelerators, causing beam instabilities, emittance growth, particle losses, and heating of the machine elements. This thesis focuses on the CERN LHC, where these effects can lead to a reduction of the integrated luminosity that would otherwise be produced.

The longitudinal intensity effects in the LHC did not pose a performance limit so far. During commissioning and machine development sessions, loss of Landau damping was observed for bunches with a small longitudinal emittance or high intensity (or both), compared to the nominal parameters. In normal operation, only a slow-growing single-bunch instability has been observed at the end of very long fills (>20 h), but with a small impact on the integrated luminosity even 5 h after the onset of the instability [85]. However, after the future LHC upgrade, the bunch intensity will be pushed by a factor 2 and the bunch length will be reduced to about 1 ns, with a possible negative impact on the longitudinal beam stability. Therefore, a good understanding of the longitudinal intensity effects is crucial for reliable estimation of the current limits of the accelerator and the optimum strategies to overcome these limits in future for the beam parameters foreseen by the HL-LHC project [4].

In the first part of this PhD thesis (Chapters 3 and 4), the beam stability in the longitudinal plane has been analyzed for the LHC and the HL-LHC. The main outcome of this part is an improved knowledge of the LHC longitudinal impedance model [64] supported by beam-measurements, which is then used to study the longitudinal single-bunch stability limits in the LHC. The HL-LHC stability limits were also determined by taking into account the possibility of operating with an additional rf system.

Beam-measurements of the LHC impedance using the traditional methods are challenging due to the very low impedance of the LHC (e.g., $\mathrm{Im}Z/n \simeq 0.09\ \Omega$ for the LHC, to be compared to 5 Ω for the CERN SPS or 20 Ω for the CERN PS). Bunch phase measurements were used for estimation of the resistive impedance, although their systematic errors are larger than the required accuracy. Nevertheless, relative measurements of the resistive impedance of the TDI movable jaws are in good agreement with bench-measurements.

The expected synchrotron frequency shift from potential-well distortion is also smaller than the resolution of the peak-detected Schottky spectrum [56]. Two innovative methods to probe the LHC reactive impedance were successfully used. One of the methods is based on exciting the beam with a sinusoidal rf phase modulation to determine the synchrotron frequency shift. A better resolution is achieved than in the peak-detected Schottky spectrum and the results are consistent with analytical estimations using the LHC impedance model. In the second method, the reactive impedance was estimated from the loss of Landau damping threshold [24] and this approach is so far the most sensitive method. The stability thresholds observed during the ramp follow the analytical scaling of loss of Landau damping and measurements at flat top for different energies are in good agreement with analytical calculations and macroparticle simulations. The longitudinal tracking code BLonD [37] was adapted and used for all simulations.

The single-bunch stability for the HL-LHC was analyzed with macroparticle simulations using an updated impedance model [86] that includes all new machine elements known so far which will be installed or upgraded. Macroparticle simulations show that the beam is stable for the HL-LHC parameters, with a stability margin of ~50% in bunch intensity for the nominal longitudinal emittance (2.5 eVs) at top energy (7 TeV and rf voltage of 16 MV).

In the absence of a wideband longitudinal damper in the LHC, the use of a harmonic rf system was considered in order to increase the longitudinal stability margin in case the beam suffers from coupled-bunch instabilities, unexpected impedances, or if higher bunch intensities are required, as for some backup scenarios for e-cloud mitigation (50 ns bunch spacing and 8b4e scheme [98]). Two options for the rf frequency of the new system were analyzed, in both cases keeping the current rf system (400 MHz). The first possibility is to install an 800 MHz rf system that increases the stability margin for the HL-LHC nominal bunch length (1.08 ns). The second one is a 200 MHz rf system that would be operated using longer bunches (about 2 ns) for e-cloud mitigation.

For the first option with an extra 800 MHz rf system operating at 8 MV, the stability threshold is increased by almost a factor 4 in bunch-shortening mode (BSM) and by a factor ~7 in bunch-lengthening mode (BLM). However, the operation of the main rf system in the full-detuning scheme, which is foreseen for HL-LHC to reduce the required rf power in the klystrons, can complicate the phase synchronization between the two rf systems. For this reason, the effect of a phase shift between the two rf systems is analyzed and found negligible for BSM, but it significantly modifies the bunch shape and degrades beam stability for BLM. This is explained by the modifications in the synchrotron frequency distribution close to the bunch center.

The power requirements for the 800 MHz rf system could be relaxed if its total voltage is reduced to 4 MV and it is operated in BSM. In this configuration, the stability margin is still sufficiently large for the HL-LHC nominal bunch length (1.08 ns).

It has been shown that the half-detuning scheme could be recuperated with a sufficiently large stability margin if the voltage of the 400 MHz rf system is reduced to 8 MV and the 800 MHz rf system is operated with a voltage of 4 MV.

For operation with a 200 MHz rf system, HL-LHC beams are not stable at 450 GeV with a single rf system and the second harmonic system (400 MHz) must be used. At 7 TeV, for bunches with a length of about 2 ns, about the same stability margin is achieved for single rf operation as for a 400 MHz rf system. Operation with bunches shorter than 1.3 ns at 7 TeV is not feasible even with the 400 MHz rf system used as second harmonic.

Analytical scalings of loss of Landau damping are proposed for double rf operation based on the threshold formula for single rf [24]. A good agreement is found between simulations and the analytical scaling for operation in BSM. In BLM, the agreement is good only for small emittances. The discrepancy for larger emittances is most likely due to the synchrotron frequency spread reduction from potential-well distortion.

In the second part of the thesis (Chapter 5), bunch-by-bunch phase shift measurements have been suggested and proven to be a good diagnostic tool for the e-cloud effect. Its importance lies in the fact that e-cloud effect is currently the main limitation for LHC operation with 25 ns spaced bunches. The strategy for mitigation relies on scrubbing with beams [97], and the use of this method in operation eases the scrubbing run optimization. This novel technique can be used to observe the e-cloud buildup along the bunch trains and to calculate the total beam power loss. The required high-accuracy was achieved by a special signal treatment. Measurements of the heat load in the cryogenic system are well reproduced, although a scale factor that depends on the beam energy needs to be applied. Phase shift measurements have a very good agreement with simulations of the e-cloud buildup. This method can also be used to estimate the instantaneous heat load in the cryogenic system.

A In-phase and quadrature components

A carrier of frequency ω modulated in amplitude and in phase by two narrow-band signals, respectively $A(t)$ and $\varphi(t)$, can be decomposed into two amplitude-modulated signals of the same frequency with a phase offset of $\pi/2$ between them:

$$\begin{aligned} A(t)\cos\left[\omega t+\varphi(t)\right] &= A(t)\cos\varphi(t)\cos(\omega t) - A(t)\sin\varphi(t)\sin(\omega t) \\ &= I(t)\cos(\omega t) - Q(t)\sin(\omega t) \end{aligned} \tag{A.1}$$

where $I(t)$ and $Q(t)$ are called the in-phase and quadrature components.

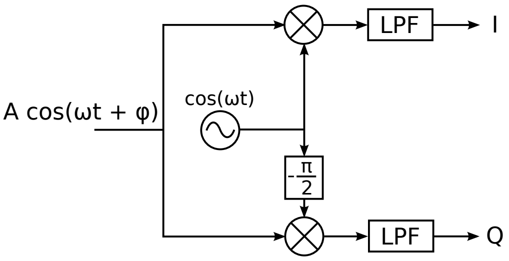

Figure A.1 – Simplified scheme of an I/Q demodulator. The input signal is split and mixed with two sinewaves at the same frequency as the input signal and a phase offset of $\pi/2$. These signals are low-pass filtered to remove the high-frequency mixing products.

A simplified scheme of an I/Q demodulator is shown in Fig. A.1. The input signal is split and mixed with two sinewaves at the same frequency as the input signal and a phase offset of $\pi/2$ between them. A low-pass filtering is required to remove the high-frequency mixing products at 2ω. The I(t) and Q(t) components are, respectively, the result of the mixing with the sinewave at the same phase (in-phase) and with the sinewave shifted in phase by $-\pi/2$ (quadrature). The $I(t)$ and $Q(t)$ signals are subsequently digitized and the amplitude $A(t)$ and the phase $\varphi(t)$ of the input signal can be easily calculated from the I/Q components using the following relations: $A(t)=\sqrt{I(t)^2+Q(t)^2}$ and $\varphi(t)=\tan^{-1}\left[\frac{Q(t)}{I(t)}\right]$.

B Phase shift due to beam loading

As mentioned in Section 2.3.3, the bunch phase measurements using the rf beam phase module should not be affected by beam loading. In order to confirm that statement, phase shift measurements were performed during a fill when the one-turn delay feedback of the low-level rf system was switched on and off. The one-turn feedback is a system that reduces the transient beam loading and the effective impedance of the rf cavities by a factor ~5 [117]. Measurements were done during the commissioning of the one-turn feedback with 25 ns beams.

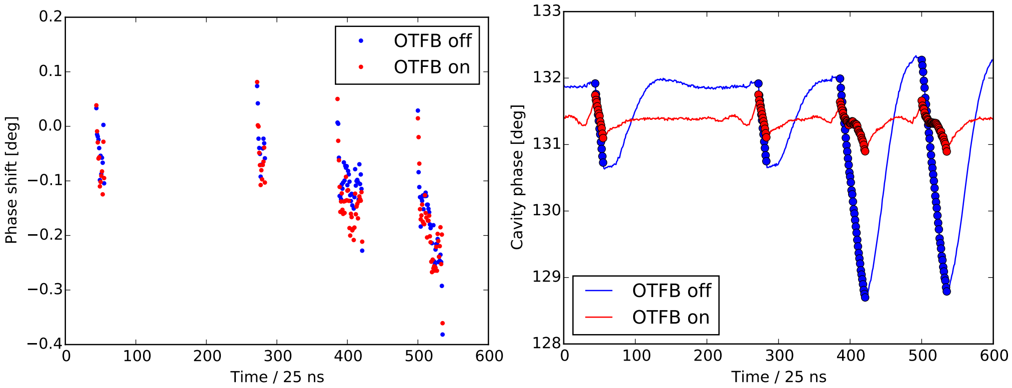

Figure B.1 – Bunch-by-bunch phase shift (left) and cavity phase (right) with the one-turn feedback off (blue) and on (red). The circles on the right plot correspond to filled buckets. Beam 2. Fill 2248 (25 ns, 24-10-2011).

Measurements of the bunch-by-bunch phase shift and cavity phase are shown in Fig. B.1. Although there is a clear reduction in the cavity-phase modulation (due to beam loading) when the one-turn feedback was switched on, the variations observed in the phase shift are below the accuracy of the measurements (~0.1 deg) and are most probably caused by changes in the beam parameters (bunch length and intensity) during the time between the measurements (~30 min). Therefore, the bunch phase measurements are practically not affected by beam loading.

Bibliography

[1] O. S. Brüning, P. Collier, P. Lebrun, S. Myers, R. Ostojic, J. Poole, and P. Proudlock, *LHC Design Report.* Geneva: CERN, 2004.

[2] ATLAS Collaboration, "Observation of a new particle in the search for the Standard Model Higgs boson with the ATLAS detector at the LHC," *Physics Letters B*, vol. 716, no. 1, pp. 1 – 29, 2012.

[3] CMS Collaboration, "Observation of a new boson at a mass of 125 GeV with the CMS experiment at the LHC," *Physics Letters B*, vol. 716, no. 1, pp. 30 – 61, 2012.

[4] G. Apollinari, I. Béjar Alonso, O. Brüning, M. Lamont, and L. Rossi, eds., *High-Luminosity Large Hadron Collider (HL-LHC): Preliminary Design Report.* Geneva: CERN, 2015.

[5] H. Damerau, A. Funken, R. Garoby, S. Gilardoni, B. Goddard, K. Hanke, A. Lombardi, D. Manglunki, M. Meddahi, B. Mikulec, G. Rumolo, E. Shaposhnikova, M. Vretenar, and J. Coupard, eds., *LHC Injectors Upgrade, Technical Design Report, Vol. I: Protons.* No. CERN-ACC-2014-0337, Dec. 2014.

[6] F. Gerigk, "Cavity types," in *CERN Accelerator School (CAS): RF for accelerators*, (Ebeltoft, Denmark), pp. 277–298, June 2010.

[7] G. Dôme, "Theory of RF acceleration," in *CERN Accelerator School (CAS): Accelerator Physics*, pp. 110–158, Sept. 1985.

[8] S. Y. Lee, *Accelerator physics.* Singapore: World Scientific, 1999.

[9] H. Goldstein, C. Poole, and J. Safko, *Classical Mechanics; 3rd ed.* San Francisco (CA), USA: Addison-Wesley, 2002.

[10] L. D. Landau and E. M. Lifshitz, *Mechanics; 3rd ed.* Course of theoretical physics, Oxford: Pergamon, 1976.

[11] H. Poincaré, *Les Méthodes nouvelles de la mechanique céleste*, vol. 3. Paris, France: Gauthier-Villars, 1892.

[12] A. A. Vlasov, "On the kinetic theory of an assembly of particles with collective interaction," *J.Phys.(USSR)*, vol. 9, pp. 25–45, 1945.

[13] T. Bohl, T. P. R. Linnecar, J. Tückmantel, and E. Shaposhnikova, “Experimental Studies of Controlled Longitudinal Emittance Blow-up in the SPS as LHC Injector and LHC Test-Bed,” in *the* 9^{th} *European Particle Accelerator Conference (EPAC’04)*, (Lucerne, Switzerland), p. 617, July 2004.

[14] P. Baudrenghien and T. Mastoridis, “Longitudinal emittance blowup in the Large Hadron Collider,” *Nuclear Instruments and Methods in Physics Research Section A: Accelerators, Spectrometers, Detectors and Associated Equipment*, vol. 726, pp. 181 – 190, 2013.

[15] J. L. Laclare, “Bunched beam coherent instabilities,” in *CERN Accelerator School (CAS): Accelerator Physics*, pp. 264–326, Sept. 1985.

[16] B. W. Zotter and S. A. Kheifets, *Impedances and wakes in high-energy particle accelerators.* Singapore: World Scientific, 1998.

[17] A. W. Chao, *Physics of collective beam instabilities in high energy accelerators.* New York (NY): Wiley, 1993.

[18] H. Risken, *The Fokker-Planck Equation.* N.Y.: Springer-Verlag, 2nd ed., 1989.

[19] F. J. Sacherer, “Methods for computing bunched-beam instabilities,” Tech. Rep. CERN/SI-BR/72-5, Geneva, Sept. 1972.

[20] K. Y. Ng, *Physics of intensity dependent beam instabilities.* Hoboken (NJ): World Scientific, 2006.

[21] L. Landau, “On the vibration of the electronic plasma,” *J. Phys. (USSR)*, vol. 10, pp. 25–34, 1946.

[22] V. K. Neil and A. M. Sessler, “Longitudinal resistive instabilities of intense coasting beams in particle accelerators,” *Review of Scientific Instruments*, vol. 36, no. 4, pp. 429–436, 1965.

[23] F. J. Sacherer, “A longitudinal stability criterion for bunched beams,” in *the* 5^{th} *IEEE Particle Accelerator Conference (PAC’73)*, (San Francisco (CA), USA), pp. 825–829, Mar. 1973.

[24] V. I. Balbekov and S. V. Ivanov, “Thresholds of longitudinal instability of bunched beam in the presence of dominant inductive impedance,” tech. rep., Protvino, 1991.

[25] E. Shaposhnikova, “Longitudinal beam parameters during acceleration in the LHC,” Tech. Rep. LHC-PROJECT-NOTE-242, CERN, Geneva, Dec. 2000.

[26] G. Papotti, T. Bohl, T. Linnecar, E. Shaposhnikova, and J. Tückmantel, “Study of Controlled Longitudinal Emittance Blow-Up for High Intensity LHC Beams in the CERN SPS,” in *the* 11^{th} *European Particle Accelerator Conference (EPAC’08)*, (Genoa, Italy), June 2008.

[27] H. Damerau, M. Morvillo, E. Shaposhnikova, J. Tückmantel, and J. L. Vallet, "Controlled Longitudinal Emittance Blow-Up in the CERN PS," in *the* 22^{nd} *Particle Accelerator Conference (PAC'07)*, (Albuquerque (NM), USA), p. 4186, June 2007.

[28] K. Ohmi, "Beam-photoelectron interactions in positron storage rings," *Phys. Rev. Lett.*, vol. 75, 1526, Aug. 1995.

[29] R. Cimino, G. Rumolo, and F. Zimmermann, eds., *Proceedings of the Joint INFN-CERN-EuCARD-AccNet Workshop on Electron-Cloud Effects (ECLOUD'12)*, (La Biodola, Italy), June 2012.

[30] F. Zimmermann, "Review of single bunch instabilities driven by an electron cloud," *Phys. Rev. ST Accel. Beams 7, 124801*, 2004.

[31] C. Benvenuti, J. Cazeneuve, P. Chiggiato, F. Cicoira, A. E. Santana, V. Johanek, V. Ruzinov, and J. Fraxedas, "A novel route to extreme vacua: the non-evaporable getter thin film coatings," *Vacuum*, vol. 53, no. 1–2, pp. 219 – 225, 1999.

[32] S. Calatroni, P. Chiggiato, P. Costa-Pinto, D. Hynds, M. Taborelli, and C. Yin Vallgren, "Amorphous-Carbon thin films for the mitigation of electron clouds in particle accelerators," in *Final CARE-HHH Workshop on Scenarios for the LHC Upgrade and FAIR*, (Chavannes-de-Bogis, Switzerland), pp. 128–132, Nov. 2008.

[33] E. Shaposhnikova *et al.*, "Experimental Studies of Carbon Coatings as Possible Means of Suppressing Beam Induced Electron Multipacting in the CERN SPS," in *the* 23^{rd} *Particle Accelerator Conference (PAC'09)*, (Vancouver, Canada), May 2009.

[34] C. Yin Vallgren, G. Arduini, J. Bauche, S. Calatroni, P. Chiggiato, K. Cornelis, P. Costa Pinto, E. Metral, G. Rumolo, E. Shaposhnikova, M. Taborelli, and G. Vandoni, "Amorphous Carbon Coatings for Mitigation of Electron Cloud in the CERN SPS," in *the* 1^{st} *International Particle Accelerator Conference (IPAC'10)*, (Kyoto, Japan), May 2010.

[35] O. Boine-Frankenheim, E. Gjonaj, F. Petrov, F. Yaman, T. Weiland, and G. Rumolo, "Energy loss and longitudinal wakefield of relativistic short proton bunches in electron clouds," *Phys. Rev. ST Accel. Beams 15, 054402*, 2012.

[36] G. Iadarola and G. Rumolo, "Electron cloud simulations with PyECLOUD," in *the* 11^{th} *International Computational Accelerator Physics Conference (ICAP2012)*, (Rostock-Warnemünde, Germany), 2012.

[37] T. Argyropoulos, J. F. Esteban Müller, A. Lasheen, D. Quartullo, and H. Timko, "Beam Longitudinal Dynamics code (BLonD)." http://blond.web.cern.ch, 2014.

[38] H. Timko, J. F. Esteban Müller, A. Lasheen, and D. Quartullo, "Benchmarking the Beam Longitudinal Dynamics Code BLonD," in *the* 7^{th} *International Particle Accelerator Conference (IPAC'16)*, (Busan, Korea), May 2016.

[39] J. A. MacLachlan, "ESME: Longitudinal Phase Space Particle Tracking. Program Documentation," 1984.

[40] G. Rumolo and F. Zimmermann, "Practical user guide for HEADTAIL," Tech. Rep. SL-Note-2002-036-AP, CERN, Geneva, Nov. 2002.

[41] A. Shishlo, S. Cousineau, J. Holmes, and T. Gorlov, "The Particle Accelerator Simulation Code PyORBIT," *Procedia Computer Science*, vol. 51, pp. 1272 – 1281, 2015. International Conference On Computational Science (ICCS 2015).

[42] G. Iadarola, G. Arduini, V. Baglin, H. Bartosik, O. Domínguez, J. F. Esteban Müller, G. Rumolo, E. Shaposhnikova, L. Tavian, and F. Zimmermann, "Electron cloud and scrubbing studies for the LHC," in *the* 4^{th} *International Particle Accelerator Conference (IPAC'13)*, (Shanghai, China), 2013.

[43] B. Salvant, O. Aberle, G. Arduini, R. Assmann, V. Baglin, M. J. Barnes, W. Bartmann, P. Baudrenghien, O. E. Berrig, C. Bracco, E. Bravin, G. Bregliozzi, R. Bruce, A. Bertarelli, F. Carra, G. Cattenoz, F. Caspers, S. Claudet, H. Day, M. Deile, J. F. Esteban Müller, P. Fassnacht, M. Garlasche, L. Gentini, B. Goddard, A. Grudiev, B. Henrist, S. Jakobsen, R. Jones, O. Kononenko, G. Lanza, L. Lari, T. Mastoridis, V. Mertens, E. Métral, N. Mounet, A. Nosych, J. Nougaret, S. Persichelli, A. Piguiet, S. Redaelli, F. Roncarolo, G. Rumolo, B. Salvachua, M. Sapinski, R. Schmidt, E. Shaposhnikova, L. Tavian, M. Timmins, J. Uythoven, A. Vidal, J. Wenninger, D. Wollmann, and M. Zerlauth, "Update on Beam Induced RF Heating in the LHC," in *the* 4^{th} *International Particle Accelerator Conference (IPAC'13)*, (Shanghai, China), May 2013.

[44] P. Baudrenghien and T. Mastoridis, "Performances and future plans of the LHC RF," in *the* 52^{nd} *ICFA Advanced Beam Dynamics Workshop on High-Intensity and High-Brightness Hadron Beams (HB2012)*, (Beijing, China), pp. 565–569, Sept. 2012.

[45] H. Timko, P. Baudrenghien, J. F. Esteban Müller, and E. Shaposhnikova, "Operational and Beam Dynamics Aspects of the RF System in 2015," in *LHC Beam Operation workshop*, (Évian-les-Bains, France), Dec. 2015.

[46] P. P. Collier, M. Ainoux, R. Guinand, J. M. Jiménez, A. Rizzo, A. Spinks, and K. Weiss, "Reducing the SPS machine impedance," in *the* 8^{th} *European Particle Accelerator Conference (EPAC'02)*, (Paris, France), pp. 1458–1460, June 2002.

[47] E. Shaposhnikova, T. Bohl, and T. P. Linnecar, "Results from the impedance reduction in the CERN SPS," in *the* 20^{th} *ICFA Advanced Beam Dynamics Workshop on High Intensity and High Brightness Hadron Beams (HB2002)*, vol. 642, (Batavia (IL), USA), pp. 62–64, Apr. 2002.

[48] P. Baudrenghien, G. Hagmann, J. C. Molendijk, R. Olsen, A. Rohlev, V. Rossi, D. Stellfeld, D. Valuch, and U. Wehrle, "The LHC Low Level RF," in *the* 10^{th} *European Particle Accelerator Conference (EPAC'06)*, (Edinburgh, UK), p. 1471, June 2006.

[49] R. Garoby, “Timing aspect of bunch transfer between circular machines: State of the art in the PS complex,” Tech. Rep. CERN-PS-RF-NOTE-84-6, Dec. 1984.

[50] P. Baudrenghien, T. Linnecar, D. Stellfeld, and U. Wehrle, “SPS Beams for LHC: RF Beam Control to Minimize Rephasing in the SPS,” in *the* 6^{th} *European Particle Accelerator Conference (EPAC’98)*, no. CERN-PS-RF-NOTE-84-6, (Stockholm, Sweden), Dec. 1998.

[51] G. Papotti, T. Bohl, F. Follin, and U. Wehrle, “Longitudinal beam measurements at the LHC: The LHC Beam Quality Monitor,” in *the* 2^{nd} *International Particle Accelerator Conference (IPAC’11)*, (San Sebastian, Spain), 2011.

[52] T. P. R. Linnecar, “The high frequency longitudinal and transverse pick-ups in the CERN SPS,” *IEEE Trans. Nucl. Sci.*, vol. 26, pp. 3409–3411, June 1979.

[53] T. Bohl and J. F. Malo, “The APWL Wideband Wall Current Monitor,” Tech. Rep. CERN-BE-2009-006, CERN, Geneva, Feb. 2009.

[54] J. Durand, “Combining wideband signals from a wall current monitor,” Tech. Rep. PS-LP-Note-94-14-Tech, CERN, CERN, Apr. 1994.

[55] T. Linnecar, T. Bohl, E. Shaposhnikova, and J. Tückmantel, “Capture Losses Caused by Intensity Effects in the CERN SPS,” in *the* 33^{rd} *ICFA Advanced Beam Dynamics Workshop: High Intensity High Brightness Hadron Beams (HB2004)*, pp. 345–349, 2004.

[56] E. Shaposhnikova, T. Bohl, and T. Linnecar, “Longitudinal peak detected Schottky spectrum,” in *the* 46^{th} *ICFA Advanced Beam Dynamics Workshop on High-Intensity and High-Brightness Hadron Beams (HB2010)*, (Morschach, Switzerland), Sept. 2010.

[57] U. S. NIM Committee, “Standard NIM instrumentation system,” tech. rep., May 1990.

[58] T. E. Levens, T. Bohl, and U. Wehrle, “A beam-synchronous gated peak-detector for the LHC beam observation system,” in *the* 2^{nd} *International Beam Instrumentation Conference (IBIC2013)*, (Oxford, UK), Sept. 2013.

[59] A. Butterworth, J. Molendijk, R. Sorokoletov, and F. Weierud, “Control of the Low Level RF System of the Large Hadron Collider,” in *the* 10^{th} *International Conference on Accelerator and Large Experimental Physics Control Systems (ICALEPCS 2005)*, (Geneva, Switzerland), 2005.

[60] D. Valuch and P. Baudrenghien, “Beam phase measurement and transverse position measurement module for the LHC,” in *Low Level Radio Frequency Workshop (LLRF 2007)*, (Knoxville (TN), USA), 2007.

[61] M. Ojeda, P. Baudrenghien, A. C. Butterworth, J. Galindo, W. Höfle, T. E. Levens, J. C. Molendijk, F. Vaga, and D. Valuch, “Processing High-Bandwidth Buncn-by-Bunch Observation Data form the RF and Transverse Damper Systems of the LHC,” in *the* 15^{th} *International Conference on Accelerator and Large Experimental Control Systems (ICALEPCS 2015)*, (Melbourne, Australia), 2015.

[62] C. Roderick, L. Burdzanowski, and G. Kruk, “The CERN accelerator logging service - 10 years in operation: a look at the past, present, and future,” in *the* 14^{th} *International Conference on Accelerator and Large Experimental Physics Control Systems (ICALEPCS 2013)*, (San Francisco (CA), USA), 2013.

[63] F. Ruggiero, “Single-beam collective effects in the LHC,” *Part. Accel.*, vol. 50, pp. 83–104. 21 p, Feb. 1995.

[64] N. Mounet, *The LHC transverse coupled-bunch instability.* PhD thesis, EPFL, 2012.

[65] B. Salvant, O. Aberle, G. Arduini, R. Assmann, V. Baglin, M. J. Barnes, P. Baudrenghien, A. Bertarelli, C. Bracco, R. Bruce, X. Buffat, A. Burov, F. Carra, G. Cattenoz, F. Caspers, S. Claudet, H. Day, J. F. Esteban Müller, M. Garlasché, L. Gentini, B. Goddard, A. Grudiev, B. Henrist, W. Herr, S. Jakobsen, R. Jones, G. Lanza, L. Lari, T. Mastoridis, E. Métral, N. Mounet, A. Nosych, J. L. Nougaret, S. Persichelli, T. Pieloni, A. M. Piguiet, S. Redaelli, F. Roncarolo, G. Rumolo, B. Salvachua, M. Sapinski, E. Shaposhnikova, L. Tavian, M. Timmins, J. Uythoven, A. Vidal, R. Wasef, S. White, and D. Wollman, “LHC impedance model: experience with high intensity operation in the LHC,” in *the* 52^{nd} *ICFA Advanced Beam Dynamics Workshop on High-Intensity and High-Brightness Hadron Beams (HB2012)*, (Beijing, China), Sept. 2012.

[66] J. F. Esteban Müller, B. Salvant, and E. Shaposhnikova, “Longitudinal parameters and beam induced heating,” in *LHC Beam Operation workshop*, (Évian-les-Bains, France), 2014.

[67] B. Salvant, O. Aberle, M. Albert, R. Alemany Fernández, G. Arduini, J. Baechler, M. J. Barnes, P. Baudrenghien, O. E. Berrig, N. Biancacci, M. Bozzo, G. Bregliozzi, F. Carra, F. Caspers, P. Chiggiato, A. Danisi, H. Day, M. Deile, D. Druzhkin, J. F. Esteban Müller, S. Jakobsen, J. Kuczerowski, A. Lechner, R. Losito, A. Masi, E. Métral, N. Minafra, A. Nosych, A. Perillo Marcone, D. Perini, S. Redaelli, F. Roncarolo, G. Rumolo, E. Shaposhnikova, J. Uythoven, A. J. Välimaa, J. E. Varela Campelo, C. Vollinger, N. Wang, M. Wendt, J. Wenninger, and C. Zannini, “Beam Induced RF Heating in LHC in 2015,” in *the* 7^{th} *International Particle Accelerator Conference (IPAC’16)*, (Busan, Korea), May 2016.

[68] J. F. Esteban Müller, T. Argyropoulos, T. Bohl, T. Mastoridis, N. Mounet, G. Papotti, B. Salvant, E. Shaposhnikova, and D. Valuch, “Measurements of the LHC longitudinal resistive impedance with beam,” in *the* 52^{nd} *ICFA Advanced Beam Dynamics Workshop on High-Intensity and High-Brightness Hadron Beams (HB2012)*, (Beijing, China), Sept. 2012.

[69] E. Shaposhnikova, T. Argyropoulos, T. Bohl, A. Burov, R. Calaga, L. Ficcadenti, E. Metral, N. Mounet, T. Mastoridis, J. F. Esteban Müller, V. Kain, G. Papotti, and F. Roncarolo, “Studies of the LHC impedance at injection energy,” Tech. Rep. CERN-ATS-Note-2012-060 MD, July 2012.

[70] J. F. Esteban Müller, T. Argyropoulos, T. Bohl, C. Bhat, R. Calaga, V. Kain, M. Kuhn, N. Mounet, G. Papotti, E. Shaposhnikova, and H. Timko, "Probing the LHC impedance with single bunches," Tech. Rep. CERN-ATS-Note-2013-001 MD, Jan. 2013.

[71] V. Kain, B. Goddard, R. Schmidt, and J. Wenninger, "Protection Level during Extraction, Transfer and Injection into the LHC," Tech. Rep. LHC-Project-Report-851, Aug. 2005.

[72] B. Salvant, A. Grudiev, V. Baglin, B. Goddard, E. Métral, and M. Timmins, "Electromagnetic simulations of the impedance of the LHC injection protection collimator," in *the* 3^{rd} *International Particle Accelerator Conference (IPAC'12)*, (New Orleans (LA), USA), 2012.

[73] B. Salvant, O. Aberle, M. Albert, R. Alemany, F. Antoniou, M. Barnes, P. Baudrenghien, O. Berrig, N. Biancacci, J. Boyd, F. Carra, F. Caspers, P. Chiggiato, A. Danisi, H. Day, M. Deile, J. F. Esteban Müller, M. Ferro-Luzzi, S. Gilardoni, S. Jakobsen, J. Kuczerowski, M. Lamont, A. Lechner, I. Llamas Garcia, R. Losito, A. Masi, E. Métral, N. Minafra, A. Nosych, A. Perillo Marcone, S. Redaelli, F. Roncarolo, G. Rumolo, E. Shaposhnikova, A. Tauro, J. Uythoven, A. Valimaa, J. Varela, C. Vollinger, N. Wang, M. Wendt, J. Wenninger, and C. Zannini, "Beam induced RF heating including TDI," in *LHC Performance Workshop*, (Chamonix, France), Jan. 2016.

[74] J. Uythoven, N. Biancacci, C. Bracco, O. Frasciello, L. Gentini, B. Goddard, A. Lechner, F. L. Maciariello, A. Perillo Marcone, N. Shetty, G. Steele, B. Salvant, F. Velotti, and M. Zobov, "Injection protection upgrade for the HL-LHC," in *the* 6^{th} *International Particle Accelerator Conference (IPAC'15)*, (Richmond (VA), USA), 2015.

[75] J. F. Esteban Müller, T. Argyropoulos, C. Bhat, S. Jakobsen, T. Mastoridis, E. Metral, N. Mounet, G. Papotti, T. Pieloni, B. Salvant, E. Shaposhnikova, and H. Timko, "Beam induced heating reduction by bunch flattening," Tech. Rep. CERN-ACC-NOTE-2014-0011, Mar. 2014.

[76] E. Shaposhnikova, T. Argyropoulos, P. Baudrenghien, C. Bhat, A. Burov, J. F. Esteban Müller, T. Mastoridis, G. Papotti, B. Salvant, and H. Timko, "Flat bunches in the LHC," in *the* 5^{th} *International Particle Accelerator Conference (IPAC'14)*, (Dresden, Germany), June 2014.

[77] R. Garoby, S. Hancock, and J. L. Vallet, "Production of flat-topped bunches," Tech. Rep. PS/RF/Note 92-8, 1992.

[78] R. Cappi, R. Garoby, S. Hancock, M. Martini, and J. P. Riunaud, "Measurement and reduction of transverse emittance blow-up induced by space charge effects," in *the* 15^{th} *IEEE Particle Accelerator Conference (PAC'93)*, (Washington D.C., USA), 1993.

[79] C. Y. Tan and A. Burov, "Phase modulation of the bucket stops bunch oscillations at the Fermilab Tevatron," *Phys. Rev. ST Accel. Beams*, vol. 15, 044401, Apr. 2012.

[80] E. Shaposhnikova, T. Argyropoulos, T. Bohl, C. Bhat, P. Baudrenghien, A. Butterworth, T. Mastoridis, J. F. Esteban Müller, G. Papotti, J. Tückmantel, W. Venturini Delsolaro, and U. Wehrle, "Loss of Landau damping in the LHC," in *the* 2^{nd} *International Particle Accelerator Conference (IPAC'11)*, (San Sebastián, Spain), Sept. 2011.

[81] E. Shaposhnikova, T. Argyropoulos, C. Bhat, T. Bohl, P. Baudrenghien, J. F. Esteban Müller, W. Höfle, G. Papotti, J. Tückmantel, D. Valuch, W. Venturini Delsolaro, and U. Wehrle, "Studies of longitudinal single bunch stability," Tech. Rep. CERN-ATS-Note-2011-041 MD, May 2011.

[82] E. Shaposhnikova, T. Argyropoulos, C. Bhat, T. Bohl, P. Baudrenghien, T. Mastoridis, J. F. Esteban Müller, G. Papotti, J. Tückmantel, and W. Venturini Delsolaro, "Longitudinal single bunch stability in LHC with phase loop on," Tech. Rep. CERN-ATS-Note-2011-056 MD, July 2011.

[83] J. F. Esteban Müller, P. Baudrenghien, A. Lasheen, T. Roggen, E. Shaposhnikova, and H. Timko, "LHC Longitudinal Single-Bunch Stability Threshold," Tech. Rep. CERN-ACC-NOTE-2016-0001, Jan. 2016.

[84] J. F. Esteban Müller, T. Argyropoulos, T. Bohl, N. Mounet, E. Shaposhnikova, and H. Timko, "Beam measurements of the LHC impedance and validation of the impedance model," in *the* 5^{th} *International Particle Accelerator Conference (IPAC'14)*, (Dresden, Germany), June 2014.

[85] P. Baudrenghien, J. F. Esteban Müller, E. Shaposhnikova, and H. Timko, "RF and Transverse Damper Systems," in *LHC Performance Workshop*, (Chamonix, France), Jan. 2016.

[86] N. Biancacci, "Update on the HL-LHC impedance budget," in *the* 4^{th} *Joint HiLumi LHC-LARP Annual Meeting*, (KEK, Tsukuba, Japan), Nov. 2014.

[87] R. Calaga, E. Jensen, G. Burt, and A. Ratti, "Crab Cavity Development," *Adv. Ser. Dir. High Energy Phys.*, vol. 24, pp. 137–156, 2015.

[88] F. Zimmermann and H. Schmickler, "Long-range beam–beam compensation using wires," *Adv. Ser. Dir. High Energy Phys.*, vol. 24, pp. 243–267, 2015.

[89] F. Carra, A. Bertarelli, A. Dallocchio, L. Gentini, P. Gradassi, G. Maitrejean, A. Manousos, N. Mariani, N. Mounet, E. Quaranta, S. Redaelli, and V. Vlachoudis, "Mechanical engineering and design of novel collimators for HL-LHC," in *the* 5^{th} *International Particle Accelerator Conference (IPAC'14)*, (Dresden, Germany), June 2014.

[90] A. Bertarelli, A. Dallocchio, M. Garlasche, L. Gentini, P. Gradassi, M. Guinchard, S. Redaelli, A. Rossi, O. Sacristan De Frutos, F. Carra, and E. Quaranta, "Novel Materials for Collimators at LHC and its Upgrades," in *the* 54^{th} *ICFA Advanced Beam Dynamics Workshop on High-Intensity and High-Brightness Hadron Beams (HB2014)*, (East-Lansing (MI), USA), Nov. 2014.

[91] E. Métral, G. Arduini, D. Banfi, J. Barranco Garcia, N. Biancacci, O. Brüning, R. De Maria, M. Giovannozzi, W. Höfle, K. Li, J. F. Esteban Müller, Y. Papaphilippou, T. Pieloni, B. Salvant, E. Shaposhnikova, C. Tambasco, A. Valishev, D. Valuch, and A. Wolski, "HL-LHC Operational Scenarios. High Luminosity LHC," Tech. Rep. CERN-ACC-NOTE-2015-0009, May 2015.

[92] D. Boussard, D. Brandt, and L. Vos, "Is a longitudinal feedback system required for LHC?," Tech. Rep. LHC-Project-note-205, CERN, Geneva, Oct. 1999.

[93] E. Shaposhnikova, "Impedance effects during injection, energy ramp and store," in *the* 4^{th} *LHC Crab Cavity Workshop (LHC-CC10)*, (CERN, Geneva, Switzerland), Dec. 2010.

[94] T. Linnecar and E. Shaposhnikova, "An RF System for Landau Damping in the LHC," Tech. Rep. CERN-LHC-Project-note-394, Feb. 2007.

[95] J. F. Esteban Müller, R. Calaga, and E. Shaposhnikova, "Lower of higher harmonic RF system in the LHC," in *Joint LIU / HL-LHC Meeting*, (CERN, Geneva, Switzerland), Oct. 2015.

[96] G. Iadarola, "25 ns operation and MDs in the LHC - findings and consequences for the LIU and HL-LHC," in *Joint LIU / HL-LHC meeting*, (Geneva, Switzerland), Oct. 2015.

[97] G. Iadarola, H. Bartosik, K. Li, L. Mether, A. Romano, G. Rumolo, and M. Schenk, "Electron Cloud Effects," in *LHC Performance Workshop*, (Chamonix, France), Jan. 2016.

[98] H. Damerau, "Different bunch/batch schemes," in *Joint LIU / HL-LHC meeting*, (Geneva, Switzerland), Oct. 2015.

[99] G. Iadarola, *Electron cloud studies for CERN particle accelerators and simulations code development.* PhD thesis, Università degli Studi di Napoli Federico II, 2014.

[100] T. Argyropoulos, *Longitudinal beam instabilities in a double RF system.* PhD thesis, National Technical University of Athens, Jan. 2015.

[101] E. Shaposhnikova, T. Bohl, and T. P. R. Linnecar, "Beam transfer functions and beam stabilisation in a double RF system," in *Particle Accelerator Conference (PAC'05)*, (Knoxville (TN), USA), May 2005.

[102] V. I. Balbekov and S. V. Ivanov, "Methods for suppressing the longitudinal instability of a bunched beam with the help of Landau damping," *Soviet Atomic Energy*, vol. 62, no. 2, pp. 117–125, 1987.

[103] D. Boussard, "RF power requirements for a high intensity proton collider," in *the* 14^{th} *IEEE Particle Accelerator Conference (PAC'91)*, (San Francisco (CA), USA), pp. 2447–2449, May 1991.

[104] J. Tückmantel, "Adaptive RF Transient Reduction for High Intensity Beams with Gaps," in *the* 10^{th} *European Particle Accelerator Conference (EPAC'06)*, (Edinburgh, UK), pp. 541–543, June 2006.

[105] T. Mastoridis, P. Baudrenghien, A. Butterworth, J. Molendijk, and J. Tückmantel, "Cavity Voltage Phase Modulation MD," tech. rep., CERN, Geneva, Switzerland, Sept. 2012.

[106] T. Roggen, P. Baudrenghien, and R. Calaga, "A Higher Harmonic Cavity at 800 MHz for HL-LHC," in *the* 17^{th} *International Conference on RF Superconductivity*, (Whistler (BC), Canada), Sept. 2015.

[107] P. Baudrenghien and T. Mastoridis, "Power requirements for the LHC harmonic cavities with the full-detuning scheme," in *the* 2^{nd} *LHC Harmonic Cavity meeting*, (Geneva, Switzerland), pp. 541–543, May 2013.

[108] R. Calaga, "HL-LHC RF Roadmap," in *LHC Performance Workshop*, (Chamonix, France), Sept. 2014.

[109] R. Tomás, G. Arduini, D. Banfi, J. Barranco, H. Bartosik, O. Brüning, R. Calaga, O. Domínguez, H. Damerau, S. Fartoukh, S. Hancock, G. Iadarola, R. de Maria, E. Métral, T. Pieloni, G. Rumolo, B. Salvant, E. Shaposhnikova, and S. White, "HL-LHC alternatives scenarios," in *LHC Performance Workshop*, (Chamonix, France), Sept. 2014.

[110] G. Rumolo, G. Arduini, V. Baglin, H. Bartosik, N. Biancacci, P. Baudrenghien, G. Bregliozzi, P. Chiggiato, S. Claudet, R. De Maria, J. F. Esteban Müller, M. Favier, C. Hansen, W. Höfle, J. M. Jimenez, V. Kain, G. Lanza, K. Li, H. Maury Cuna, E. Métral, G. Papotti, T. Pieloni, F. Roncarolo, B. Salvant, E. Shaposhnikova, R. Steinhagen, L. Tavian, D. Valuch, W. Venturini Delsolaro, F. Zimmermann, U. Iriso, O. Domínguez, E. Koukovini-Platia, N. Mounet, C. Zannini, and C. Bhat, "Electron cloud observation in LHC," in *the* 2^{nd} *International Particle Accelerator Conference (IPAC'11)*, (San Sebastián, Spain), Sept. 2011.

[111] J. F. Esteban Müller and E. Shaposhnikova, "Synchronous phase measurements in the LHC for electron cloud observations," Tech. Rep. CERN-ACC-NOTE-2013-0007 PERF, CERN, 2012.

[112] E. Shaposhnikova, "Stable phase shift for beam with 50 ns and 75 ns bunch spacing," in *LHC Beam Commissioning Working Group*, (Geneva, Switzerland), Nov. 2010.

[113] J. F. Esteban Müller, P. Baudrenghien, G. Iadarola, T. Mastoridis, G. Papotti, G. Rumolo, E. Shaposhnikova, and D. Valuch, "Synchronous phase shift at LHC," in *Joint INFN-CERN-EuCARD-AccNet Workshop on Electron-Cloud Effects (ECLOUD'12)*, (La Biodola, Italy), June 2012.

[114] J. F. Esteban Müller and E. Shaposhnikova, "Synchronous phase measurements in the LHC for electron cloud observations," Tech. Rep. CERN-ACC-NOTE-2013-0007 PERF, CERN, Geneva, Switzerland, 2013.

[115] K. Brodzinski and L. Tavian, “First measurements of beam-induced heating on the LHC cryogenic system,” in *the* 24^{th} *International Cryogenic Engineering Conference and International Cryogenic Materials Conference (ICEC 24 - ICMC 2012),* (Fukoaka, Japan), 2012.

[116] L. Tavian, “Performance limitations of the LHC cryogenics: 2012 review and 2015 outlook,” in *LHC Beam Operation workshop,* (Évian-les-Bains, France), 2012.

[117] T. Mastoridis, P. Baudrenghien, and J. Molendijk, “LHC One-Turn Delay Feedback Commissioning,” in *the* 3^{rd} *International Particle Accelerator Conference (IPAC'12),* (New Orleans (LA), USA), 2012.